UNIVERSITÁ DEGLI STUDI DI CATANIA

DIPARTIMENTO DI FISICA E ASTRONOMIA

DOTTORATO DI RICERCA IN FISICA

Study of the ^{19}F(p,α)^{16}O reaction through the Trojan Horse Method and its astrophysical enviroment

PH.D. THESIS

Author:

Dr. I. Indelicato

Supervisor:

Chiar.mo Prof. C. Spitaleri

CICLO XXVII 2011/2014

"If a cluttered desk is a sign of a cluttered mind, of what, then, is an empty desk a sign?"

Albert Einstein

UNIVERSITÁ DEGLI STUDI DI CATANIA

Abstract

Faculty Name
Dipartimento di fisica e astronomia

Ph.D Thesis

by Dr. I. Indelicato

Fluorine nucleosynthesis takes place in the hydrogen-helium intershell region of Asymptotic Giant Branch (AGB) stars and in the same region also the *s* elements are produced. Because fluorine is produced in the He-intershell and then dredged up to the surface together with *s* process elements, its abundance is used as probe for AGB models and nucleosynthesis and is one of the most important input parameters for an analysis of *s* process in AGB star conditions. The problem is that current models fail to explain the highest F enhancements found in the low-mass AGB stars. A possible way to explain this abundance found in AGB star envelopes might be provided by a revision of the uncertainties in the nuclear reaction rates involved in the synthesis of this nuclide in these stars. In particular, The ^{19}F(p,α)^{16}O reaction is the main destruction channel of fluorine at the bottom of the convective envelope in AGB stars, where it can experience temperatures large enough to determine its destruction, owing to extra-mixing processes. Because of the Coulomb barrier, measurements available in the literature do not have access to the energy region of astrophysical interest, corresponding to the Gamow peak ($E_{c.m.}$ = 38 keV). Direct measurements of the cross section stop at about 500 keV for the α_0 channel (with ^{16}O being left in its ground state following ^{20}Ne decay), thus the astrophysical factor was then extrapolated to low energies assuming a non resonant energy trend. In the case of extra-mixing phenomena, which are characterized by a maximum temperature of about 10^7 K, the energy region below 500 keV is of key importance, thus requiring further and accurate investigations to evaluate the contribution of possible resonances, which could significantly enhance the reaction rate at such low temperatures. So, a new experimental study through the Trojan Horse Method (THM) is important because the method is

particulary suited for the study of low-enegy resonances in the case of charged particle induced reactions. It is an experimental indirect technique which selects the quasi-free contribution of an appropriate three-body reaction performed at energies well above the Coulomb barrier, to extract a charged-particle two-body cross section at astrophysical energies free from coulomb suppression. Two experimental runs were performed using the THM, extracting the quasi-free contribution to the ^{2}H(^{19}F,α^{16}O)n three-body reaction. In this work I focused on the second run especially because of the improved angular and energy resolution allowed to draw accurate quantitative conclusions from the data for the α_0 channel. The measurement was performed at the Laboratori Nazionali di Legnaro in July 2012 where the Tandem accelerator provided a 55 MeV ^{19}F beam which impinged onto CD_2 targets. The experimental setup consisted of a telescope devoted to oxygen detection, made up of an ionization chamber and a silicon position sensitive detector (PSD) on one side with respect to the beam direction and one additional PSD on the opposite side for coincident detection of the α particles. In the beginning of the experimental work, I described the reason leading to the choice of the three-body reaction, of the beam energy, of the setup and of the detection angles. After the off-line analysis in which I widely described the detector calibration, the three-body reaction channel selection, the study of reaction mechanism and the selection of the quasi-free contribution are discussed. Finally the cross-section reaction are extracted and compared with the available direct measurement. The analysis of the α_0 channel shows the presence of resonant structure never observed before that could lead to a significant increase in the reaction rate at astrophysical temperatures, with important consequences for stellar nucleosynthesis.

Contents

List of Figures

List of Tables

Abbreviations

BBN	**B**ig **B**ang **N**ucleosynthesis
SBBN	**S**tandard**B**ig **B**ang **N**ucleosynthesis
AGB	**A**symptotic **G**iant **B**ranch
HR	**H**ertzsprung **R**ussell
ZAMS	**Z**ero **A**ge Main**S**equence
RGB	**R**ed **G**iant **B**ranch
TP	**T**hermal **P**ulse
PDCZ	**P**ulse **D**riven **C**onvective**Z**one
TDU	**T**hird**D**redge **U**p
WR	**W**alf **R**aye
HBP	**H**ot**B**ottom **P**rocess
CBP	**C**ool**B**ottom **P**rocess
CEMP	**C**arbon **E**nhanced **M**etal**P**oor
PPN	**P**roto **P**lanetary **N**ebulae
SiC	**Si**licon **C**arbide
CD	**C**oulomb **D**issociation
ANC	**A**symptotic **N**ormalization **C**oefficient

THM	**T**rojan **H**orse **M**ethod
DWBA	**D**istorted**W**ave **B**orn**A**pproximation
DWIA	**D**istorted**W**ave **I**mpulse**A**pproximation
PWIA	**P**lane**W**ave **I**mpulse**A**pproximation
QF	**Q**uasi **F**ree
HOES	**H**alf**O**ff **E**nergy**S**hell
OES	**O**n **E**nergy**S**hell
SD	**S**equential **D**ecay
SM	**S**equential **M**echanism
DBU	**D**irect **B**reak**U**p
PSD	**P**osition **S**ensitive**D**etector
IC	**I**onization **C**hamber
ADC	**A**nalogical **D**igital**C**onverter
TFA	**T**ime **F**ilter**A**mpifier
TAC	**T**ime **A**mplitude**C**onverter
SCA	**S**ingle **C**hannel**A**nalyzer
GG	**G**ate **G**enerator
FWHM	**F**ull**W**idth **H**alf**M**aximum

To my family...

Introduction

Almost all the elements we know today are produced in stars of different types and initial masses, the only exceptions being hydrogen, helium and traces of lithium formed in the Big-Bang Nucleosynthesis. The absence of stable nuclei with A=5 or A=8, together with the Coulomb barrier increase for reactions between heavier nuclei substantially stops the cosmological production in correspondence of ^{7}Li in Standard Big Bang Nucleosynthesis. All of the heavier nuclides with A$\geq$12 are produced in stars, and among them the nuclides beyond the iron peak are formed from neutron capture processes. In particular, the *s*-elements (heavy-element from Fe to Pb) are "cooked" inside stars with masses below about three times the Solar mass, during a late evolutionary phase called Asymptotic Giant Branch (AGB) [6]. These stars experience an ingestion of protons into the helium-rich layer during the core He-flash, resulting in the production of ^{13}C. In this way, the ^{13}C(α,n)^{16}O reaction would then be the source of neutrons for the *s* process [7]. In addition to the production of *s* process elements, AGB stars may also be a rich site for the nucleosynthesis of lighter elements, such as fluorine.

Its nucleosynthesis takes place in the same region wher the *s* elements are produced and its abundance is very sensitive to the physical condition in AGB. For this reason it is used as probe for AGB models and nucleosynthesis and is one of the most important input parameters for an analysis of *s* process in AGB star conditions. Thus, fluorine abundance observed in these objects can constrain AGB star models since it is strictly connected to the mixing processes taking place inside them. Anyway, the highest values of the observed ^{19}F enhancements in the stellar atmosphere are not matched by the current models.

Primary sources of uncertainty in predicting fluorine abundances in AGB stars are both the adopted reaction rates and the treatment of the mixing phenomena as well as the associated nucleosynthesis at the bottom of the convective envelope

[9, 10].

In particular, in the present work we focus on the ^{19}F(p,α_0)^{16}O reaction (^{16}O being left in its ground state following ^{20}Ne decay) that represents the main fluorine destruction channel in this low-temperature, proton-rich environment [9]. Its reaction rate is determined by the contribution of several resonances, about 10, which show up below 1 MeV, and by the non-resonant contribution. Direct measurements of this cross section [15] stop at about 500 keV in the C.M. frame, thus only theoretical estimates or spectroscopic studies are available elsewhere.

In the case of extra-mixing phenomena, which are characterized by a maximum temperature of about 10^7 K, the energy region below 500 keV is of key importance. Thus only model calculations of the reaction rate are actually available in the temperature region most relevant for ^{19}F nucleosynthesis in AGB stars. For this reason a measurement of the low energy cross section is extremely important but experimentally it is very difficult.

In fact, this measurement has to be performed inside the energy window relevant for astrophysics (the so-called Gamow windows) that as said before extends well below 1 MeV. Anyway these energies are much lower than the Coulomb barrier of the ^{19}F+p channel that is about 2.5 MeV. Sice cross sections exponentially drop in the sub-Coulomb region, measuring of the nuclear processes under investigation is very difficult. In addition, the electron screening effect, due to the electrons surrounding the interacting ions, prevents one to measure the bare-nucleus cross section, which is the information required for the astrophysical calculations. The only way to get the low-energy cross section is then by extrapolating the behavior of the higher energy data. This is done by means of the definition of the astrophysical S(E)-factor, which represents essentially the cross section free of Coulomb suppression and allows for an easier extrapolation:

$$S(E) = \sigma(E)E^{2\pi\eta} \tag{1}$$

where $\exp(2\pi\eta)$ is the inverse of the Gamow factor, which removes the dominant energy dependence of σ(E) due to the barrier penetrability.

But, extrapolation can introduce large errors due to, for istance the presence of unexpected resonances or high energy tails of subthreshold resonances or the wrong estimate of the electron screening potential.

For this reason, a number of indirect methods, such as Coulomb Dissociation (CD) [28], Asymptotic Normalization Coefficient (ANC) [29], and Trojan Horse Method (THM) [30], have been introduced as complementary and/or alternative approaches for determining the bare-nucleus S(E)-factor.
The last one is particularly suited for extracting low-energy cross section for nuclear reactions having charged particles or neutrons in the exit channel. THM is an experimental indirect technique which selects the quasi-free contribution of an appropriate three-body reaction performed at energies well above the Coulomb barrier, to extract a charged-particle two-body cross section at astrophysical energies free from Coulomb suppression. A reaction

$$A + a \rightarrow C + c + s \tag{2}$$

with nucleus $a{=}x \oplus s$ having a strong cluster structure and with three particles in the final states, can proceed by various reaction mechanisms. In the application of THM we are interested in the process where the Trojan horse nucleus a breaks up into a cluster x that is the transferred particle and where the nucleus s can be regarded as a spectator to the two-body subreaction:

$$A + x \rightarrow C + c \tag{3}$$

The idea is that the particle x (participant) is conducted inside the nuclear field of A, where the reaction takes place, from a, which for this reason is named Trojan horse nucleus. In this way it overcomes the problem of the Coulomb suppression and electron screening. So, under proper kinematical condition, the particle A interacts only with the cluster x which comes from the direct break-up of the target nucleus a, whereas the cluster s proceeding indisturbed behaves as a spectator to the two-body process. In order to completely determine the kinematical properties of the spectator s, the two ejectiles c and C have to be detected, identified and their energies and emission angles measured.

In the case of direct break-up, the two-body cross section can be derived from the measurement of three-body cross section and from the knowledge of the momentum distribution of x inside the Trojan-horse nucleus.

$$\frac{d3\sigma}{dE_C d\Omega_C d\Omega_c} \propto KF|\Phi(\vec{p}_s)|^2 \left(\frac{d\sigma^{HOES}}{d\Omega}\right) \quad (4)$$

where $|\Phi(\vec{p}_s)|^2$ is the momentum distribution of cluster s inside a and $\frac{d\sigma^{HOES}}{d\Omega}$ the off-shell cross section of the reaction in equation 3.

In the present work the experimental study of the ^{19}F(p,α)^{16}O reaction via the THM is described.

The experiment was performed in Legnaro at the Laboratori Nazionali di Legnaro (Padova) where the Tandem accelerator provided a 55 MeV ^{19}F beam impinged onto CD_2 targets. The experimental setup consisted of a telescope devoted to oxygen detection, made up of an ionization chamber and a silicon position sensitive detector on one side with respect to the beam direction and one additional silicon PSD on the opposite side of the beam axis optimized for coincident detection of the alfa particles. A symmetric setup allowed to double the statistic.

After detector calibration, the first step of the data analysis is to single out the events corresponding to the three-body reaction.

Since different reactions can take place in the target a careful selection of the reaction channel is necessary. The channel selection procedure begins with the separation of the oxygen locus in the ΔE-E two-dimensional plot by means of a graphical cut. As reaction n.3 has three nuclei in the exit channel, the reaction products are distributed around a characteristic kinematic locus, because their kinetic energies are correlated by energy and momentum conservation equations. From a comparison with a Monte Carlo simulation it is possible to single out the reaction channel of interest from all the other. Besides the experimental Q-value has been extracted for the selected events by imposing energy balance for the three-body reaction and compared with the theoretical one.

After the selection of the ^{16}O-α-n exit channel, the following step in data analysis is to establish whether in the selected experimental kinematic regions the contribution of the QF process to the overall ^{16}O-α coincidence yield is evident and well separated from others.

Through this study it is shown that the QF mechanism can be selected without significant contribution from contaminant sequential decay processes and the analysis in Plane Wave Impulse Approximation is sufficient to describe the process. So the extraction of the cross section from the selected data was carried out and

it show for the first time the presence of resonances in the ^{19}F(p,α)^{16}O reaction at astrophysical energies, possibly determining a sensitive change in the reaction rate.

The structure of this work is reported hereafter:

- Chapter 1: stellar evolution and the problematic connected to the ^{19}F(p,α)^{16}O reaction are presented. In particular the *s* process, the AGB phase, the mixing process and the fluorine nucleosynthesis are reviewed;
- Chapter 2: some quantities which are relevant for nuclear astrophysics, such as the reaction rate and the astrophysical factor are defined;
- Chapter 3: the indirect techniques are discussed. Greatest attention is addressed to the TH method;
- Chapter 4: the indirect study of the ^{19}F(p,α)^{16}O reaction through the THM, the choise of the three-body reaction, of the beam energy and the detection angles are described;
- Chapter 5: the data analysis procedure, the channel selection, the study of reaction mechanism and finally the extraction of the cross-section are reported.

Chapter 1

Astrophysics Motivation

1.1 The solar abundances

Nuclear astrophysics is the study of the nuclear processes which drive the birth, evolution and death of stars and of how all naturally occurring elements formed and evolved into our present universe. In fact, it is one of the primary goals of physicists today to explain the origin and abundance of all the elements and their isotopes in the universe.

The basics of the nucleosynthesis occurring in stars were set in 1957 by the work of Burbidge, Burbidge, Fowler and Hoyle [31]. Their paper provided a classification of nucleosynthesis processes into eight types where each process is associated with its product nuclei and the typical temperature and site where it occurs showing how stars can produce elements and their isotopes from helium to uranium.

Our current cosmological belief is that the nuclei make up the majority of matter were first made from nucleons created a short time after the beginning of the Universe, in the Big-Bang. Nuclei were later forged in the interiors of stars of different types and initial masses and stellar explosions.

The solar system abundances of nuclides are shown in Fig.1.1, which displays the abundances of elements plotted against atomic number. This distribution displays several important features helped in the identification and early description of the nuclear process that could be responsible for their production. The graph has a decreasing trend from left to right, that is from light to heavy elements. Almost

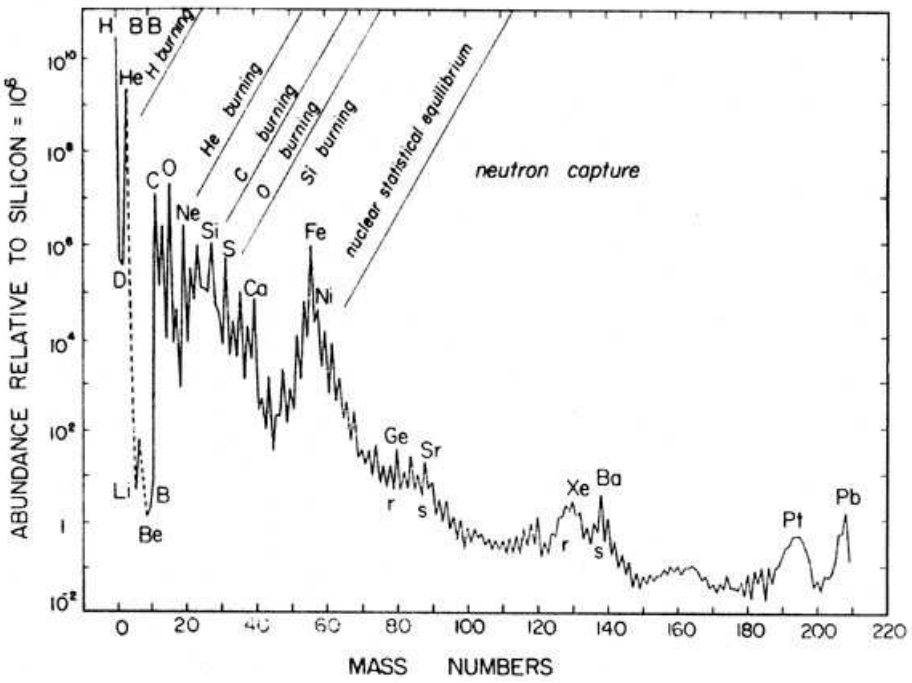

FIGURE 1.1: The relative abundances of all elements measured in the solar system, as a function of mass number A normalized to 10^6Si atoms and the y-axis is a logarithmic scale.

all the mass is contained in H(71%) and He(27%).
All of this hydrogen and the majority of helium were formed in the early universe by big bang nucleosynthesis (BBN) and are the basic building blocks for the synthesis of heavier and more complex nuclei [32]. Because of the decreasing temperature and density of the Big Bang and the lack of nuclei at atomic masses 5 and 8, only a scant few heavier elements (hydrogen, helium and traces of lithium) could be created during BBN.

Some elements have anomalous abundances, showing a deep abundance minimum or maximum respect to the general trend. For instance, there is an abundance minimum in the A=5-11 region, corresponding to the elements Li, Be and B.
These nuclides are easily destroyed in fusion reactions with protons. Therefore, their observed solar system abundances must be explained by processes that occur in sites other than stellar interiors. They are thought to be produced via spallation reactions induced by Galactic cosmic rays [33].
All of the heavier nuclides with A≥12 are produced in stars. The nuclides in the region between ^{12}C and ^{40}Ca are synthesized via charged-particle nuclear reactions in various stellar burning processes. Reactions between charged particles are subject to the Coulomb repulsion. The larger the charge of the reacting nuclei,

the smaller the nuclear reaction probability will become. This circumstance is reflected in the overall decline of the abundance curve from ^{12}C to ^{40}Ca.

The theories of nucleosynthesis are interwined with the theories of nuclear structure as it was soon recognised that the features observed in the solar system distribution of abundances are related to the nuclear properties of each element. For example appearing abundances peak at mass numbers for closed proton and neutron shells. The magic numbers [1] for nuclear stability are 2, 8, 20, 28, 50, 82 and 126; and nuclides with Z or N equal to these magic numbers are the ones that show large abundances in the diagram (because are more stable than those with slightly higher neutron numbers and have low neutron-capture cross-sections). This is particularly notable for the light doubly-magic nuclei with equal magic Z and N, for example ^{4}He (Z=N=2), ^{16}O (Z=N=8) and ^{40}Ca (Z=N=20).

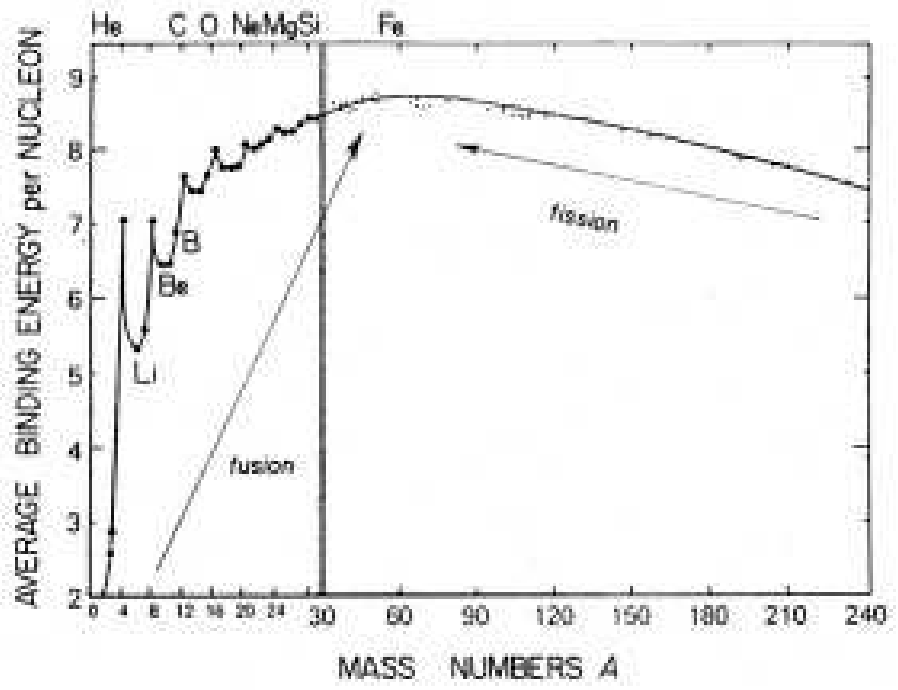

FIGURE 1.2: Binding energy per nucleon as a function of mass number A [1]. Comparison with the peaks in Fig. 1.1 shows the strong correlation between elemental abundance and nuclear binding energy.

Another significant feature is the abundance maximum of the iron peak that is related to the fact that these nuclides represent energetically the most stable species (see Fig. 1.2). Because of the large Coulomb repulsion, the synthesis of nuclides

[1] Same elements with a configuration of a particular number of neutrons or protons are particulary stable.

beyond the iron peak via charged-particle reactions becomes very unlikely. These nuclei are instead produced by neutron capture processes.

Burbidge et al.[31] and Cameron [34] showed that only two sets of physical conditions were necessary to explain the abundances of the heavy elements in the solar system: The s process is present when there is a low neutron densities, of the order of 10^7-10^8 cm^{-3}; while the r process is due to a strong flux of neutrons, when the neutron densities are higher than $\simeq 10^{20}$ cm^{-3}, and it is believed to occur during explosives phases of stellar evolution (Novae, SuperNovae and X-rays binaries).

In the s (slow) process the neutron-capture rate is much lower than the β^--decay rates, while in the r (rapid) process the neutron-capture rate is much faster than the β^--decay so that neutron capture dominates.

About half of all elements heavier than iron are produced in a stellar environment through the$s$ processes. Many improvements were soon presented, thanks to increased precision in the measurements of isotope abundances from meteorites and of neutron capture cross sections. Various reviews dealing with the$s$ process, and with connected stellar and nuclear issues have been published over the years, especially for a late evolutionary phase called Asymptotic Giant Branch (AGB) stars where neutron-rich elements are produc inside stars with masses below about three times the Solar mass, and then carried to the surface by a series of mixing phenomena [6].

1.2 Evolution prior and through the AGB phase

AGB stars represent a late phase of evolution of stars with an initial mass between about 0.8 and 8 $M_\odot$ [2] [36]. In particular, low-mass stars shall be defined as those stars less massive than $\approx 2.25 M_\odot$ while those of between 2.25 and 8 $M_\odot$ will be refered to as intermediate-mass stars [3].

1.2.1 Evolution prior the AGB phase

Depending on its initial mass, every star goes through specific evolutionary stages dictated by its internal structure and how it produces energy. Each of these stages corresponds to a change in the surface temperature and luminosity of the star, which can be seen to move to different regions on the Hertzsprung-Russell diagram[3] as it evolves.

When a star is born, it is situated on the so called Zero Age Main Sequence (or ZAMS). Therefore, the ZAMS curve represents the position of the stars in the HR diagram at the onset of hydrogen burning in their core [2] (see Fig. 1.3).

There are two process by wich this may happen: the proton-proton chain and the CNO-cycle. The first one shown in figure 1.4 and starts with the fusion of two protons to deuterium (^{2}H) which can, once sufficient deuterium accumulates, capture another proton to build up ^{3}He. Finally, two ^{3}He can react to ^{4}He, releasing two protons in the process. This set of reactions constitutes the first branch of the pp chain (ppI). There are another two set of reactions constitutes the second branch (ppII) and the third branch (ppIII) summarized in figure 1.4. These two branches contribute just a small percentage of the energy production in a star. For example, in about 70% of the energy is produced from the ppI chain, 30% from the ppII and only a fraction of a percent comes from the ppIII chain.

[2]The upper limit comes from the fact that more massive stars ignite carbon in non degenerate condition. These stars through a series of nuclear burnings proceed either to the construction of an iron core and subsequent photodissociation instability with core collapse and end their life in a Supernova explosion. The lower limit reflect the fact that stars below this mass not have time to evolve [35].

[3]The H-R Diagram is a graph that astronomrs use to classify stars according to their luminosity and temperature.

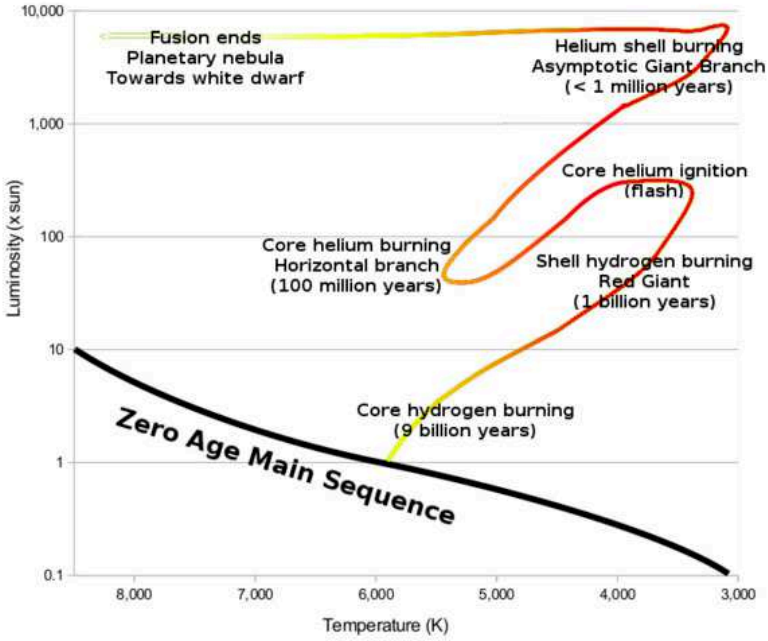

FIGURE 1.3: An H-R diagram showing the evolutionary track of a Sun-like star.

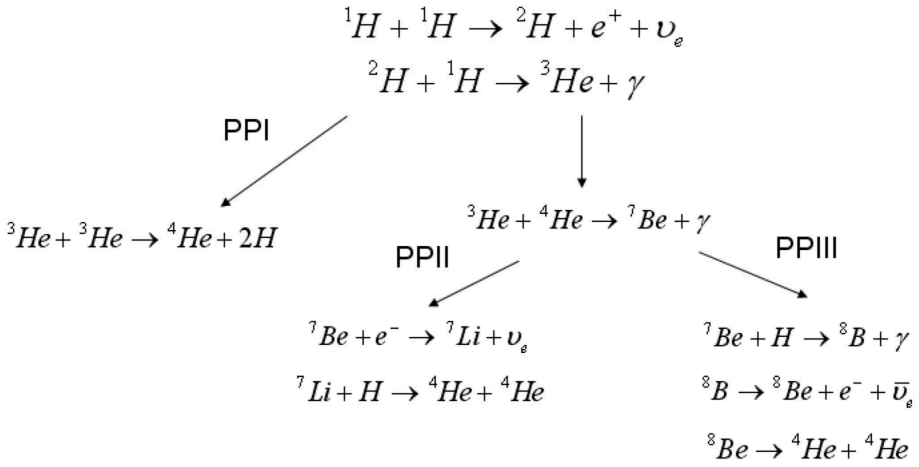

FIGURE 1.4: Figure shows the pp chains [2]. Each of the pp chains fuses four protons to onehelium nucleus.

For all of the pp chains, the first step is the creation of the deuterium and this the slowest reaction because it proceeds via the weak interaction the cross-section is smaller than for all of the reactions in the chains. This reaction therefore governs the length of time for which a star will undergo hydrogen fusion, its main sequence lifetime [37].

Owing to the different energies carried away by the neutrinos, for each ^{4}He nucleus produced by the ppI chain 26.5 MeV of energy is liberated, while the ppII and ppIII chains produces respectively 25.97 MeV and 19.59 MeV [38].

If a star consists exclusively of hydrogen and helium, then significant energy can only be generated during the hydrogen burning stage via the operation of the pp chains. Most stars, however, consist of gas that contains heavier nuclides, particularly those in the C, N, and O mass region. Hence, these nuclei can act as catalysts as the fusion of hydrogen [39]. The resulting different set of reactions through which hydrogen can be converted to helium are referred to as the CNO cycles [40].

Figure 1.5 compares the total energy generate for the pp chain and CNO cycles as a function of temperature and shows that the pp chain dominates for lower temperatures, while the CNO cycle dominate energy production for higher temperatures.
The pp chain is the principal energy source in the stars with $M \leq M_{\odot}$ [1]. Above temperatures of $2x10^7$K, and in the presence of heavier elements, a different set of reactions dominates energy production from hydrogen.

The temperature dependency of energy production (ϵ(T)) for the pp chain is $\epsilon \approx T^4$, while for the CNO cycle is $\epsilon \approx T^{18}$. The consequence is that for a given metallicity[4] the first one is the dominant source of energy at lower core temperatures while at higher temperature the CNO cycles dominates the energy production.

The temperature in the stellar interior depends on the stellar mass. Therefore, in all hydrogen burning stars with insignificant CNO seed abundances the pp chain dominate the energy production [39]. In stars with significant CNO seed abundances, the pp chain is the main source of energy in the low-mass stars ,

[4]The fraction of mass composed by elements heavier than He in a star is commonly indicated by Z,and named metallicity.

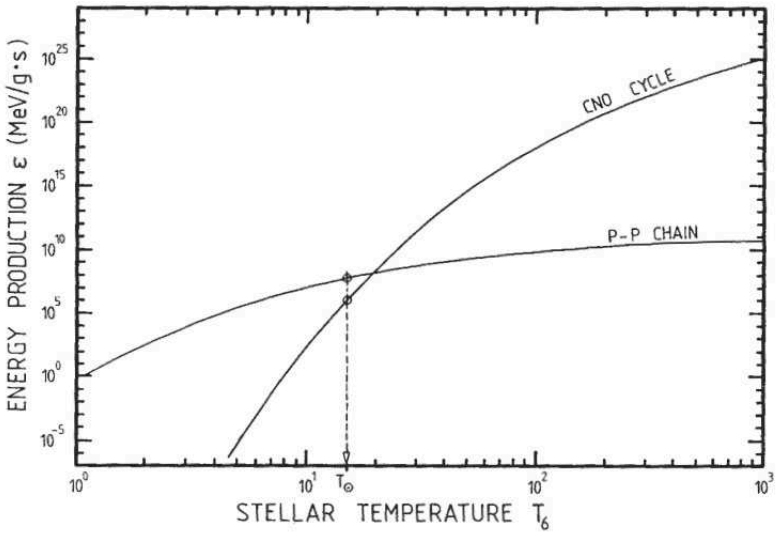

FIGURE 1.5: Energy production as a function of central temperature for the p-p chain and the CNO cycle. The dot denotes conditions in the solar core: the Sun is powered dominantly by the pp chain. The contribution by the CNO cycle is at roughly 10% of the total energy production.

while in stars more massive than Sun, the energy production from the CNO cycle overtakes the pp chains and becomes the dominant mode of energy production [1].

The CNO cycle is shown diagrammatically in fig. 1.6. Like the pp chain, this cycle converts four protons into a helium nucleus and only the hydrogen nuclei are consumed in the cycle. For example, if the cycle starts at ^{12}C leads through a series of proton capture and β-decay processes via ^{13}N, ^{13}C, ^{14}N, ^{15}O and ^{15}N back to ^{12}C.

The ^{15}N+p reaction shows a branching via ^{16}O into an additional cycle, which is roughly 10^3 times less probable [38]. The situation is best illustrated in fig. 1.6 in which are shown all of the cycles.
The various CNO cycles exist because at each of the branch point nuclei ^{15}N, ^{17}O, ^{18}O, the (p,α) reaction will compete with the (p,γ) reaction. In fact, while the proton-induced reactions on the nuclei ^{12}C, ^{13}C, ^{14}N and ^{16}O can proceed via the (p,γ) reaction, for the proton-induced reactions on these nuclei both the (p,γ) and (p,α) channels are energetically allowed [39].

The main sequence eventually terminates when all the hydrogen in the core has been processed into helium.

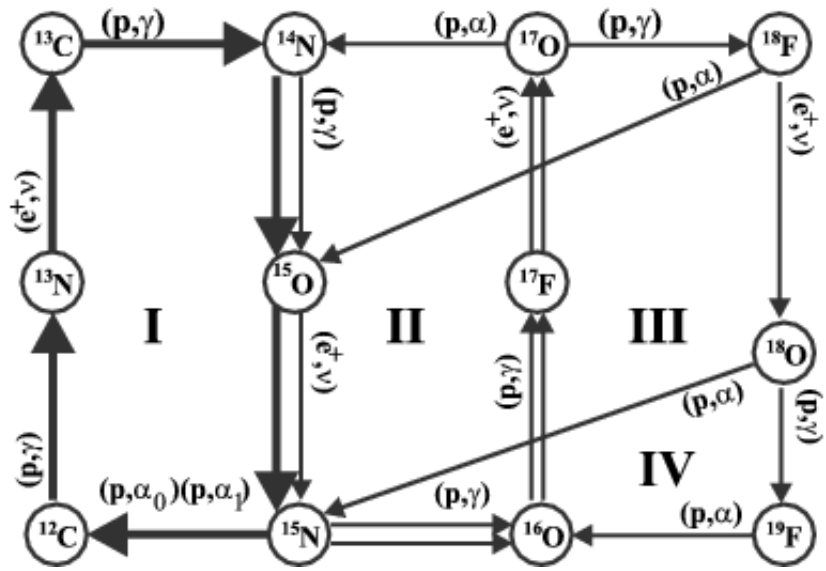

FIGURE 1.6: The four CNO cycles. Each reaction cycle fuses four protons to one ^{4}He nucleus.

The star leaves the main sequence and nuclear burning reactions advances in a shell surrounding the contracting ^{4}He core [3].

When the mass of the He core is about 10% of the total stellar mass, the central core becomes electron degenerate and the outer layers of the star respond to the increasing temperature in the core [5] by expanding and cooling down; they become convective [6] and the star makes the transition to what is know as the Red Giant Branch (RGB), far to the right of the H-R diagram (see fig. 1.3) [41].

As the star ascends the RGB the convective envelope deepens, reaching into layers that have been partially processed by hydrogen burning. Some of these nuclei, as ^{4}He, ^{13}C, ^{14}N, are then moved up to the stellar surface altering the surface composition. The surface becomes enhanced in ^{4}He and ^{14}N while the abundance of carbon drops [42]. The process is called the first dredge-up (1DUP).

When the core temperature reaches about T $\approx$ 0.1 GK, helium starts burning in the core. This provides the star with a new source of energy and re-establishes a new hydrostatic equilibrium [39].

[5] the gas pressure in a degenerate gas is independent of temperature. Therefore, when the core contracts, the temperature increases

[6] Convection is the transport of energy by rising cells (or blobs) of matter within a star [2].

However, depending on the star's total mass, the ignition of helium can take place either violenty during a helium-core-flash [7] in low mass stars due to their degenerated cores after the main sequence, or quietly in intermediate mass stars, who reach the necessary temperatures before the core degenerates [43].

Helium in the core can burn via the following chain of reactions:

$$^4He + ^4He \leftrightarrow ^8Be + \gamma \tag{1.1}$$

$$^8Be + ^4He \rightarrow ^{12} C^* + \gamma \tag{1.2}$$

$$^{12}C^* \rightarrow ^{12} C + \gamma \tag{1.3}$$

In the first step, two α particles interact to form ^{8}Be in its ground state. This nucleus is unstable by an energy of only 92 keV and disintegrates back into two α particles with a half-life of $T_{1/2}$=6.7x10^{-17} s [39]. However this half-life is large enough to allow for a second capture of a α particle. It is facilitated by the fact that the combined energy of a Be and a He match almost exactly an excited state of the carbon nucleus corresponding to an excitation energy of 7.68 MeV [31, 44].

There are a number of other reactions which contribute during helium burning. In fact, as the carbon abundance increases, helium may also burn via the reaction:

$$^{12}C + ^4He \rightarrow ^{16} O + \gamma \tag{1.4}$$

or

$$^{16}O + ^4 He \rightarrow ^{20} Ne + \gamma \tag{1.5}$$

Therefore, the result of core helium burning is a CO-core with traces of neon.

The next phase of the evolution is very similar to the evolution we have already discussed following exhaustion of the hydrogen burning core. The contraction of the core leads to a strong expansion of the star's outer layers, causing its surface

[7] Unlike an ideal classical gas, whose pressure is proportional to its temperature,the gas pressure in a degenerate gas is indipendent of temperature. Matter becomes degenerate at relatively high densities as a result of the Pauli exclusion principle which states that no more than two spin-1/2 particles (such as electrons) can occupy a given quantum state simultaneously. A degenerate gas strongly resists further compression because electrons cannot move into lower energy levels that are already occupied [39]. Ignition in a degenerate core results in a explosive start of fusion knows as the "Helium Flash".

temperature to drop and moving the star to the right and upwards in the H-R diagram (see fig. 1.3) along the Asymptotic Giant Branch. The AGB is so named because the evolutionary track approaches the line of the RGB asimptotically from the left, and indeed it can be thought of as the shell He-burning analogue of the shell H-burning RGB.

1.2.2 Evolution through the AGB phase

After helium is depleted in the core, in stars with masses $M < 8M_{\odot}$ there is insufficient gravitational energy to generate the high temperatures required to fuse C and O into heavier nuclei. Thus, carbon does not ignite, and the C/O core contracts and becomes increasingly electron-degenerate [36]. However, the core contraction generates sufficient heat for the surrounding layer of He to start fusing in a shell and the stars enter their AGB-phase. A this point, as illustrated in Figure 1.7, the star consist of:

- a degenerate C/O core;
- a He-burning shell, located just above the core;
- an inert He intershell around it;
- a H-burning shell;
- an outer H-rich convective envelope.

During the first part of the AGB phase, called the early AGB, in stars more massive than 3-5$M_{\odot}$, the large energy flux produced by the He-burning shell causes the base of the H-rich envelope to expand and cool, so that H-burning in the shell is immediately switched off [43]. When this occurs, the outer convection zone penetrates inwards, into the intershell region. This process is known as the second dredge up. For lower mass stars, H-burning in the shell remains efficient, and prevents such a mixing. The mixing that results during this second dredge-up phase increases the He and N content of the envelope; in fact hydrogen has been completely converted into helium and both ^{12}C and ^{16}O have been converted almost completely into ^{14}N [35].

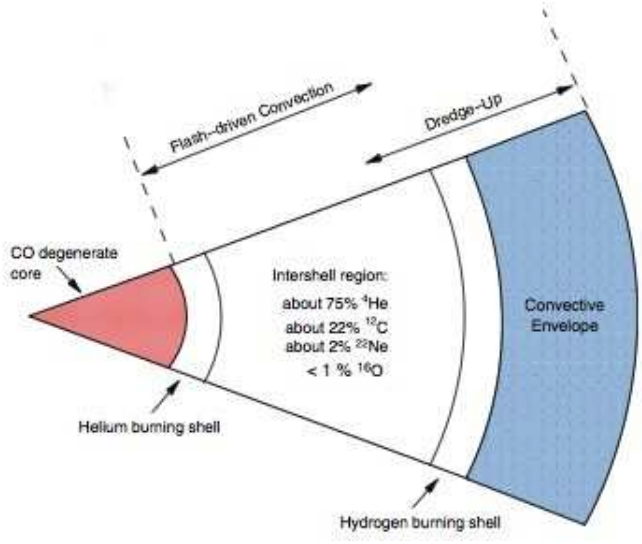

FIGURE 1.7: Illustration of the structure of an AGB star [3].

Finally, when the He burning shell gets closer to the H/He discontinuity, it dies down and, after a rapid contraction, the H burning shell fully supplies the surface energy loss. The temporary stop of the He-burning shell marks the beginning of the Thermally Pulsing AGB phase (TP-AGB) [45].

1.2.3 The Thermally Pulsing phase

The four distinct phases present in the thermal pulse are shown schematically in fig.1.8. are:

- the on phase;
- the power down phase;
- the dredge-up phase;
- the off phase;

The first thermal pulse occurs when the H burning shell accumulates enough He below it ($10^{-3}M_{\odot}$ at a core mass of $0.8M_{\odot}$), so that the He-rich zone is compressed and heated, and He reignites and a thermonuclear runaway (also known as thermal pulse, TP) occurs [43]. Due to the fast energy release, the local temperature increases and the He burning luminosity blows up, in extreme cases to 10^{9} $L_{\odot}$. This enormous energy production results in the formation of a convective zone

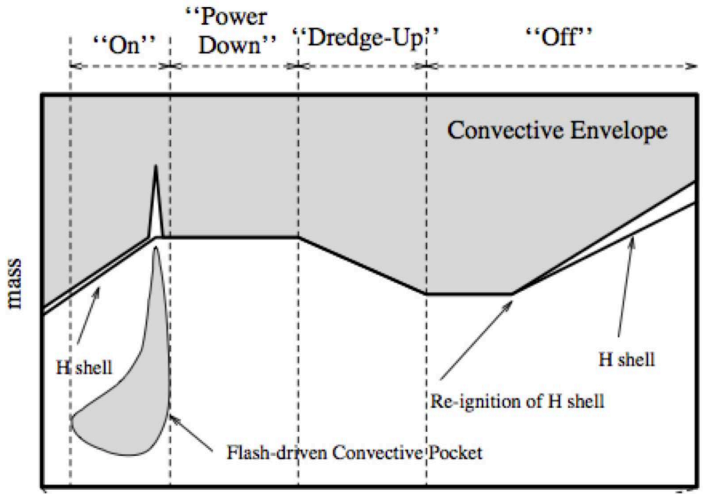

FIGURE 1.8: One thermal pulse [4, 5].

(pulse driven convective zone, PDCZ) that extends from the ^{4}He-shell almost to the H-shell (see fig.1.9).

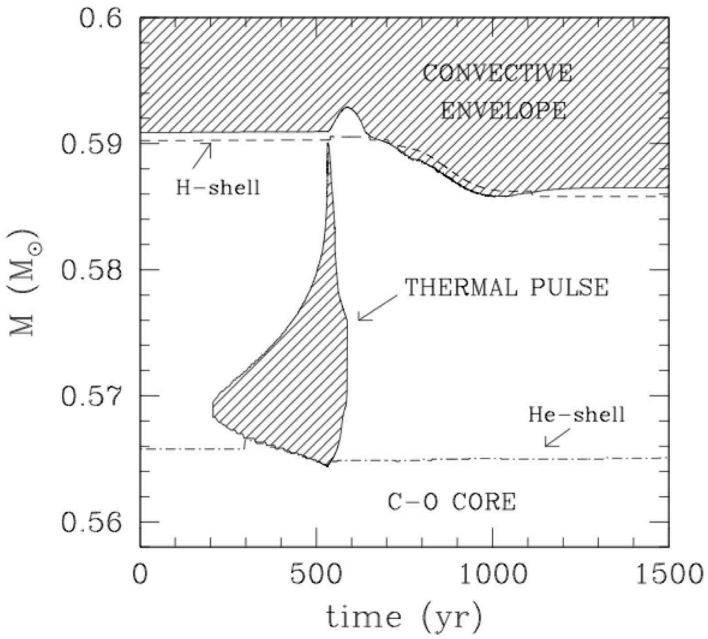

FIGURE 1.9: Convective episode in the model of M=2 $M_\odot$ [6].

This convective zone is comprises mostly of ^{4}He (about 75%) and ^{12}C (about 22%), and lasts for about 200 years [7]. The time of maximum energy output is known as the "peak" of the pulse and the decline in output thereafter is the power-down phase. In this phase, the helium luminosity decrease and intershell convection lessens. The previously released energy drives a substantial expansion, pushing the hydrogen burning shell to cooling so much that it is extinguished. In these

conditions, a third dredge up (TDU) episode is strongly favoured. After a small number of pulses, the convective envelope penetrates the into regions where the intershell convection zone had been active. This mean that the nuclei (mainly carbon) that produced during helium burning and mixed outward by the flah-driven convection, pulled into the envelope is an extremely important process as it allows material processed by nuclear reactions in the depths of a star to reach the surface where they can be observed and also returned to the interstellar medium via mass loss and planetary nebulae[37]. Especially increases the C/O ratio. This is because the third dredge-up process dredges up carbon from the interior of the star to its surface. At the end of TDU, He burning may increase again in the He shell and the star continues through a quiescent He-burning phase, which lasts until the reservoir of He produced prior the flash is used up again. At this point, He-burning dies down again and the star embarks on another long phase of quiescent H-burning. When the mass of the He-rich layers reaches the critical value previously specified, another thermal pulse is initiated and this cycle is repeated many times [43].

Spectroscopical observations show that the surface of these stars is strongly enriched in *s* process elements [46], which are produced through slow neutron captures.

1.3 The Neutron Capture Process

As discussed earlier, while the elements lighter than mass number A $\sim$ 60 are made by charged particle fusion reactions, another physical process is therefore needed to explain the existence of the nuclides beyond the iron peak. Neutron captures are the most likely way to produce these elements because capture of charged particles, such as protons or α particles, are inhibited by the large Coulomb barrier and moreover the production of any heavier nucleus by direct fusion is an endothermic process.

The capture of a neutron by an isotope of atomic number Z and mass number A defined by the following equation:

$$(A, Z) + n \rightarrow (A + 1, Z) + \gamma \tag{1.6}$$

The isotope (A+1, Z) could be stable or unstable. In the first case the neutron capture process continues accordingly with the capture cross section of the isotope involved and the isotope (A+2 ,Z) will be synthesized. In the other case, the neutron capture time scale τ_n of the isotope (A+1, Z) has to be compared with its β-decay time scale τ_β, where the β-decay is define by the following equations [47]:

➢ β^--decay

$$(A + 1, Z) \rightarrow (A + 1, Z + 1) + e^- + \overline{\nu_e} \tag{1.7}$$

➢ $-\beta^+$-decay

$$(A + 1, Z) \rightarrow (A + 1, Z - 1) + e^+ + \nu_e \tag{1.8}$$

There are three possible situations:

- $\tau_n \gg \tau_\beta$ The neutron capture to the isotope (A+2, Z) is favoured with respect the β^--decay to the isotope (A+2, Z+1)

  This case is defined as r process and it is characterised by high neutron density (10^{20} cm^{-3}), which requires very high temperatures and extreme conditions. During r-process, isotopes extremely enriched of neutrons are formed until the β^--decay is favoured with respect the neutron capture. In

this way the τ_β involved can reach values close to 10^{-6} sec. When the neutron density decreases unstable nuclei reach a stable configuration through consecutive decays.

- $\tau_n \ll \tau_\beta$ The β^--decay is favoured with respect the neutron capture. If the isotope (A+2, Z+1) is stable or its τ_n is longer or comparable with its τ_β the nucleosynthesis by neutron capture can go ahead to heavier nuclei.

  This case is defined as *s* process, where the typical neutron density is 10^6-10^9 cm^{-3} [31]. The *s*-process path goes along the valley of β stability and its termination point is ^{209}Bi (Z=83).

- $\tau_n \sim \tau_\beta$ The neutron capture is comparable with the β^--decay. In this case the isotope (A+1, Z) is an open branching between the two processes during the neutron exposure.

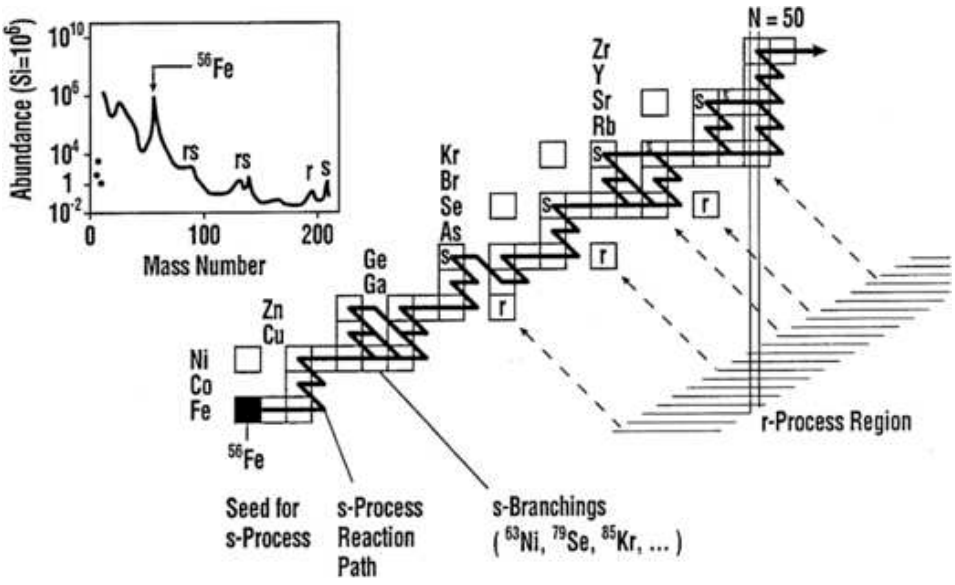

FIGURE 1.10: Neutron capture paths of the *s* process and r process shown on the chart of the nuclides between iron and the actinides.

Fig. 1.10 shows that the neutron capture path of the *s* process follows the valley of stability. The r process path is shifted to the far neutron-rich region, from where the reaction products decay back to stability.

1.3.1 The *s* process in stellar evolution

The key ingredient in activating the *s* process reactions is the neutron source.
At the time of B^2FH, many of the reaction rates necessary to predict which reactions were key for neutron production were poorly known. For this reason several candidate reactions were proposed. Chief among these were the $^{13}C(\alpha, n)^{16}O$ and $^{21}Ne(\alpha, n)^{24}Mg$ reactions which can be produced by the $^{12}C(p, \gamma)^{13}N(\beta+\nu)^{13}C$ and $^{20}Ne(p, \gamma)^{21}Na(\beta+\nu)^{21}Ne$ reaction chains, respectively, during Helium burning [48]. Soon after B^2FH, it was suggested by Cameron [34] that because most of the CNO nuclei are converted into ^{14}N (slowest reaction rate), the reaction chain $^{14}N(\alpha,\gamma)^{18}F(\beta^+\nu)^{18}O(\alpha,\gamma)^{22}Ne(\alpha, n)^{25}Mg$ was a viable candidate as an *s* process neutron source.
Furthermore, in a stellar interior, the problem of predicting the main source of neutrons for *s* process nucleosynthesis is more complex than simply which neutron emitting reaction has the highest rate. In fact, the several reactions purposed by B^2FH are dependent on proton captures. If *s* process nucleosynthesis is to occur in Helium burning, this requires that some mixing occur between the hydrogen shell and the helium core [48]. But, the question how the process of the extra mixing of proton really works is not well understood.

The exception is the reaction chain $^{14}N(\alpha,\gamma)^{18}F(\beta^+\nu)^{18}O(\alpha,\gamma)^{22}Ne(\alpha, n)^{25}Mg$ where only α-capture reactions are involved. From this point of view, the $^{22}Ne(\alpha, n)^{25}Mg$ is a more natural candidate since the ^{14}N and ^{4}He are already present in the burning environment.
Our current understanding of *s* process nucleosynthesis suggests at least two nuclei represent the best candidates for the source of neutrons: ^{13}C and ^{22}Ne, which produce neutrons, respectively, via the $^{13}C(\alpha,n)^{16}O$ and via the $^{22}Ne(\alpha,n)^{25}Mg$ reactions [49, 50].

Depending on the dominant neutron source, a different *s* element pattern is expected. This is due to the fact that the $^{13}C(\alpha,n)^{16}O$ reaction is activated at temperatures around 0.9 x 10^8 K, while the ^{22}Ne neutron source can only be efficient in intermediate mass AGB stars where the temperatures are higher [43].

Clayton et al. [51, 52] showed that to reproduce the solar system abundance of *s* only nuclei we a mix of three components:

1. Weak Component: is required in order to explain most of the *s* isotopes with A<90, from Fe to Sr;

2. Strong Component: may be necessary to explain the abundances of the A=204 - 209 nuclei;

3. Main Component: produces most of the nuclei in the mass range 90 <A<204, from Sr to Pb.

The weak component likely comes from central He burning in massive stars ($M>15M_{\odot}$), where the neutron source is the $^{22}Ne(\alpha,n)^{25}Mg$ reaction. This source produces a high neutron density of about 10^{10} -10^{12} n/cm^3 and needs a temperature larger than 3$-$ 3.2 x 10^8 K to be activated.

The strong component is associated with metal-poor AGB stars [53], and the main component is originate from thermally pulsing, low mass AGB stars (section 1.8, [54]). This second component is activated at relatively low temperatures (T = 0.8 -1.0 x 10^8 K) and can therefore easily explain why the abundances of *s* elements are highly enhanced in low mass AGB stars, where the temperature is low. Low mass AGB stars experience an ingestion of protons into the helium-rich layer during the core He-flash, resulting in the production of ^{13}C. In this way, the $^{13}C(\alpha,n)^{16}O$ reaction would then be the source of neutrons for the *s* process, as discussed in section 1.4.

1.4 Nucleosynthesis and mixing processes in AGB stars

The TP-AGB phase of evolution is crucial because during the thermal pulses, the temperature is high enough, on the order of 10^8 K, for a very rich nucleosynthesis to begin [46]. In this phase, main neutron sources are the ^{13}C(α,n)^{16}O reaction, active during the interpulse period, and the ^{22}Ne(α,n)^{25}Mg reaction, marginally activated within the convective shell originated by the TP [55]. In fact, this source needs a temperature larger than 3 - 3.2 x 10^8 K to be activated, while the maximum temperature achieved in low mass stars at the bottom of TPs does not exceed T = 3 x 10^8 K, hence the ^{22}Ne source is only marginally at play [54].
In the He-intershell, He is partially converted into carbon, thus, in order to obtain a sufficient amount of ^{13}C, a diffusion of protons from the H-rich envelope into the C-rich radiative zone is needed.
Neutron production and concordant *s* processing occur in two steps [56] and is shown schematically in fig. 1.11.

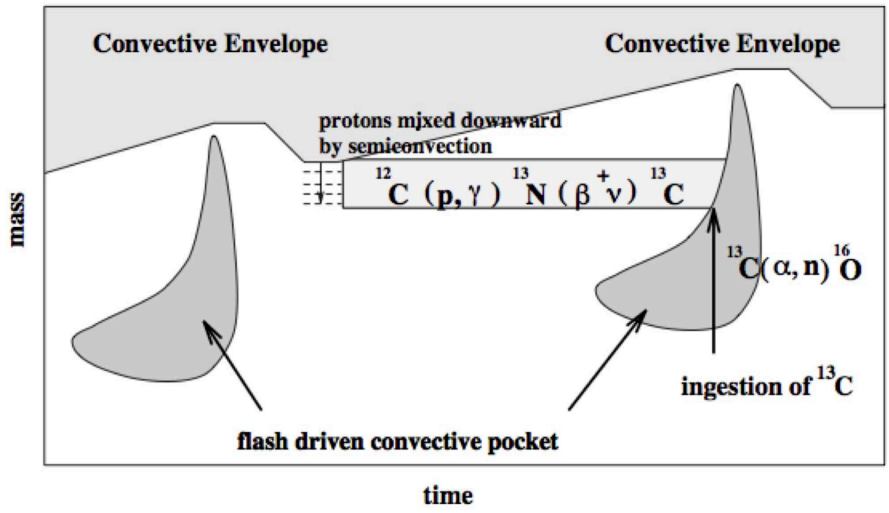

FIGURE 1.11: Schematic showing two consecutive pulses. The *s* processed material is later dredged to the surface of the star [7].

Proton which are deposited by the semiconvection during the TDU episode are in region about 75% ^{4}He and 22% ^{12}C, so these proton are captured from the abundant ^{12}C via the ^{12}C(p,γ)^{13}N(β^-)^{13}C nuclear chain, leading to the formation of a layer enriched in ^{13}C, called the ^{13}C-pocket [57]. When the star contracts again, the H shell reignites and the temperature in the ^{13}C pocket reaches about

10^8 K where the timescale for α-capture decreases below the time between pulses and the $^{13}C(\alpha, n)^{16}O$ reaction results efficiently activated. The ^{13}C produced according to this scenario is fully burned via the $^{13}C(\alpha, n)^{16}O$ reaction during the time between two consecutive thermal pulses, thus producing a low neutron density of the order of 10^7 cm^3 which are captured by the seed nuclei (belonging to the iron peak) to produce the *s* process isotopes.
Together with the H-burning ashes the *s* elements produced by this mechanism are then engulfed by the He-flash convection zone and can reach the surface by the next dredge-up event [58].
In addition to the production of *s* process elements, TP-AGB stars may also a rich site for the nucleosynthesis of light elements.
Goriely et al. [59] proposed that AGB stars could be a site for the synthesis of ^{19}F, an element whose origins have long puzzled astronomers.

During the interpulse period, only in the intermediate-mass AGB stars when the temperature at the base of the convective envelope reaches 20 x 10^6 K, the convective envelope penetrate the H-burning shell, thereby activating the so-called hot bottom burning (HBB process).
As a result, these stars depending on their initial metallicity, undergo a nucleosynthesis which involves a series of proton capture reactions at the base of the H-burning shell. Under these conditions the CN cycle is activated, carbon is converted into nitrogen by proton captures and the C/O ratio remains below unity (that is why HBB is responsible for preventing the production of carbon stars). The nucleosynthesis signatures of HBB includes enhancement in helium and nitrogen abundances; depletion of ^{18}O; a low $^{12}C/^{13}C$ ratio; a low C/O ratio; efficient destruction of ^{19}F via the $^{19}F(p,\alpha)$ and $^{19}F(p,\gamma)$ reactions; and enhancement of the abundances of ^{23}Na, ^{25}Mg, ^{26}Mg and ^{26}Al nuclei.

1.5 Fluorine nucleosynthesis

Three different astrophysical sites for fluorine nucleosynthesis have been proposed. The first was proposed by Woosley and Haxton in 1988 [60]. In the scenario they suggest, core-collapse supernovae might produce fluorine through the neutrino dissociation of ^{20}Ne and eject it prior to its destruction into the interstellar medium (see section 1.5.1). In fact, although the cross sections of neutrino-nucleus reactions are small, a large flux of nutrinos is released when the core of a massive star collapses to form a neutron star. For this reason, the ν-process can have a significant effect on the nucleosynthesis of core-collapse supernovae.

A different scenario was proposed by Meynet and Arnould in 2000 [61]. They concluded that ^{19}F could be produced in particular massive stars, so called Wolf-Rayet stars via helium-burning and then eject into the interstellar medium extreme solar winds (see section 1.5.2).

The first observational evidence in 1992 by Jorissen and Arnould [8] indicate that fluorine can be produced in the He-rich intershell region of AGB stars (see section 1.5.3). In their paper measurement of HF-features [8] in the spectra of AGB stars was published.
They found that stars with hight C/O ratios showed also higher fluorine abundances, suggesting a strong correlation between this element and these stars and that this must in some way be connected with the carbon enrichment on the stellar surface.

It is still unknown which of the three above sources is the main contributor for fluorine. The above scenario is based on several observational studies that, during the last decade, have been addressed the problem of the fluorine origin and evolution [63].

1.5.1 The ν-process scenario

Woosley and Haxton postulated that fluorine may be produced in this scenario by a two-step process. First neutrinos interact with the abundant ^{20}Ne found in

[8] The HF molecule is efficiently formed in cool stellar atmospheres and a number of strong lines appear in the near-IR K band [62]. Lines of this molecule have been used by Jorissen et al. (1992) to measure F abundances outside the solar system for the first time.

the collapsing star via neutral current inelastic scattering. These inelastic collision exicite ^{20}Ne nuclei and then the exicited ^{20}Ne* emits a proton:

$$^{20}Ne(\nu,\nu)^{20}Ne^{*} \rightarrow^{19} F + p \tag{1.9}$$

A tipical neutrino energy in this scenaio is 10 MeV and the cross section expected for inelastic neutrino collision is less than 10^{-18} barn [64]. However, a core-collapse supernova produces a large flux of neutrinos (can be estimated from the total energy of neutrinos produced in the collapse of about 10^{53} ergs, the radius of the Neon-rich shell of about 2x10^{9}cm and the neutrino temperature), approximately 10^{58} neutrinos. This large flux of neutrinos making this scenario a potentially important method of fluorine production.
The estimate of the amount of fluorine produced via neutrino nucleosynthesis is 0.42% of the original ^{20}Ne abundance (about one order of magnitude larger than the solar abundance). More recent simulations predicted significantly less fluorine production than previous studies [65].

Improving stellar model (including in the model the mass loss in the evolution of the progenitor, the nuclear reaction rates all of the heavy elements and using a more sophisticated statical model nuclear evaporation process-emission of a proton, neutron, or α-that takes into account known nuclear levels and their spins and parities) was found a value much lower than earlier calculations had predicted. This translates into a fluorine production reduction of about 40% [65].
This lower theoretical predictions of fluorine abundance and the absence of observation in supernova remnant [66] indicate that different sites of fluorine production should be considered.

1.5.2 The Walf-Rayet scenario

Wolf-Rayet stars represent an advanced phase of massive star evolution. These are a type of hot giant star, temperature above 30.000 K and masses of 10-25 $M_{\odot}$, extending up to 80 $M_{\odot}$ and are characterize by powerful stellar winds [67]. Their speeds are very fast (up to 6000 km/s) and remove large quantities of material causing the lose of their hydrogen envelopes. In this condition fusion reactions, which normally take place close to the stellar core and have direct impact on the

observed nuclear abundances, take place close to the stellar surface.
In WR-stars fluorine can be produced during early helium core burning via the chains [61]:

$$^{14}N(\alpha,\gamma)^{18}F(\beta^{+})^{18}O(p,\alpha)^{15}N(\alpha,\gamma)^{19}F \tag{1.10}$$

where neutrons and protons comes from the reactions ^{13}C(α,n)^{16}O and ^{14}N(n,p)^{14}C respectively.
Fluorine that is produced by the star via helium-burning can be carried out by high stellar winds and in this way saved from destruction.
This scenario might be an important fluorine-source but there is no direct measurement of fluorine in the stellar winds. However, there are observations of planetary nebulae which indicate fluorine production in WR-stars [68].

1.5.3 The AGB scenario

Fluorine nucleosyntesis in AGB stars takes place in the intershell region.
Jorissen [8] and Forestini [69] investigated many possible formation scenarios and the one they judge as most promising is illustrated in fig. 1.12. Here, ^{13}C produces neutrons via the ^{13}C(α,n)^{16}O reaction discussed above, and some of these neutrons are captured by ^{14}N to produce ^{14}C and protons via the ^{14}N(n,p)^{14}C reaction.

The ^{14}N nucleus needed is formed in the hydrogen burning shell, where hydrogen is burned via the CNO cycle which converts some of the dredged-up carbon into ^{14}N. This acts as a seed for the production of several species. The detail of this process depend primarily on the temperature of the intershell region, both during a pulse and during the interpulse phase, and also on the metallicity of the star [7, 70].

Starting with ^{14}N as a seed, the pathway for the production of ^{19}F is the same process as suggested for Wolf-Rayet stars:

$$^{14}N(\alpha,\gamma)^{18}F(\beta^{+})^{18}O(p,\alpha)^{15}N(\alpha,\gamma)^{19}F \tag{1.11}$$

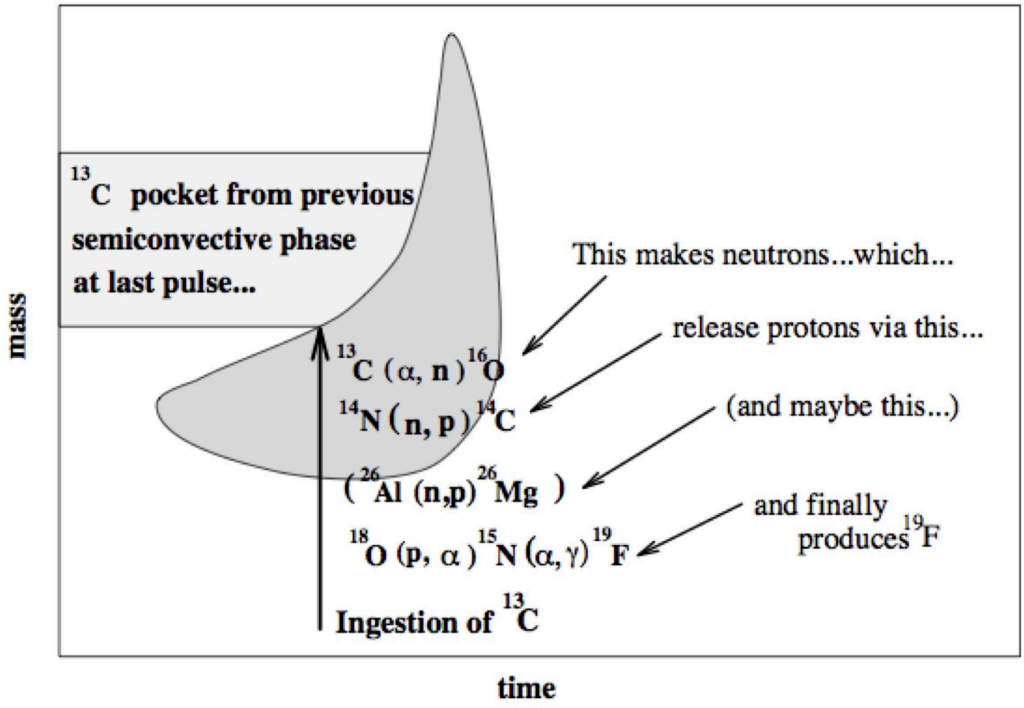

FIGURE 1.12: Schematic of the ^{19}F production mechanism.

A significant portion of ^{15}N results from the ashes of H-burning (CNO), but, this alone is not sufficient to explain the observed values. For the production of additional ^{15}N via the process ^{18}O(p,α)^{15}N, both the heavy oxygen isotope ^{18}O and a proton source are required. ^{18}O can be produced in the intershell region via the chain ^{14}N$(\alpha,\gamma)^{18}$F$(\beta^+)^{18}$O and is not the limiting factor, since both ^{14}N and ^{4}He in the H-burning ashes.

This oxygen isotope comes from the ashes of the previous thermal pulse that have been partially incorporated into the current pulse. ^{18}O easily survives α-captures at the temperatures considered and remains abundant in the pulse [7, 69].

The proton source is a problem, however, since the intershell region is H-depleted and the two possible proton source reactions, ^{14}N(n,p)^{14}C and ^{26}Al(n,p)^{26}Mg, both require neutrons to be present.

Free neutrons are unstable and must be produced in the intershell region via the reaction ^{13}C(α,n)^{16}O, which is also the main neutron source for the *s* process element seen in these stars, but they are also available for ^{14}N and ^{26}Al to capture. ^{13}C, however, is not too abundant in the intershell and a mixing-down of protons during the thermal pulse, when the outer convective zone can penetrate into the intershell region, is necessary to form a ^{13}C-rich pocket. This convective zone is also required to move the synthesized fluorine out of the area, before it can be

destroyed [7].

It is important to note that ^{19}F production depends on the ashes of the previous pulses and interpulses (^{13}C, ^{14}N, ^{15}N, ^{18}O).

Fluorine, after being produced by this rather complex production chain (see 1.11) is transported to the stellar surface during the TDU, together with other elements typical for late AGB-evolution, primarily ^{12}C and *s* process elements. Since the C/O is expected to increase as a consequence of TDU episodes during the AGB phase, this was interpreted as a clear evidence of F production in these stars [71]. Therefore, there is a strong correlation between the star's C/O ratio and its observed fluorine abundance during its late evolution.

1.6 Observation of fluorine

Fluorine can be observed in a number of different wavelength ranges. The first abundance measurements was vibrational HF-lines in the K-band (see table 1.1) by Jorissen et al. [8] and is also the first direct observational evidence of fluorine abundances higher than the solar abundance in AGB stars.
Their studies covered red giant stars of several different spectral types [9] (see table 1.1 for a brief definition of each spectral type), as shown in fig.1.13. In this work, it was found that fluorine abundances in K and M stars is consistent with the Sun. Slight overabundances were observed in some MS and S stars, and excess of fluorine found in SC stars, most C stars, some J stars and a few MS or S stars. The excess fluorine abundances as high as 100 times the solar fluorine abundance and frequently fell within the range of 3 to 30 times the solar fluorine abundance. This high values of ^{19}F enhancements observed in AGB stars are not matched by the models.
The observed enhancements of fluorine in AGB stars indicate a positive correlation with the carbon enhancements and can be explained if ^{19}F is also produced in the He intershell and then dredged up to the surface together with ^{12}C and *s* process elements [9].

[9] Stars are classified by their spectra (the elements that they absorb) and their surface temperature.

Type	Description
K	Yellow-orange stars which slightly cooler than the Sun (T_{eff} 4000 K).
M	Cool, orange-red stars (T_{eff} 3000 K).
MS	Intermediate AGB star with more carbon than M stars and less than S stars.
S	AGB star rich in *s* elements, with more carbon than M stars and less than C stars.
SC	AGB star with more carbon than S stars. Abundance of carbon and oxygen is nearly equal.
C	Carbon-rich AGB stars.
J	Carbon AGB stars with high ^{13}C abundances.

TABLE 1.1: Brief descriptions of the stellar classifications [27].

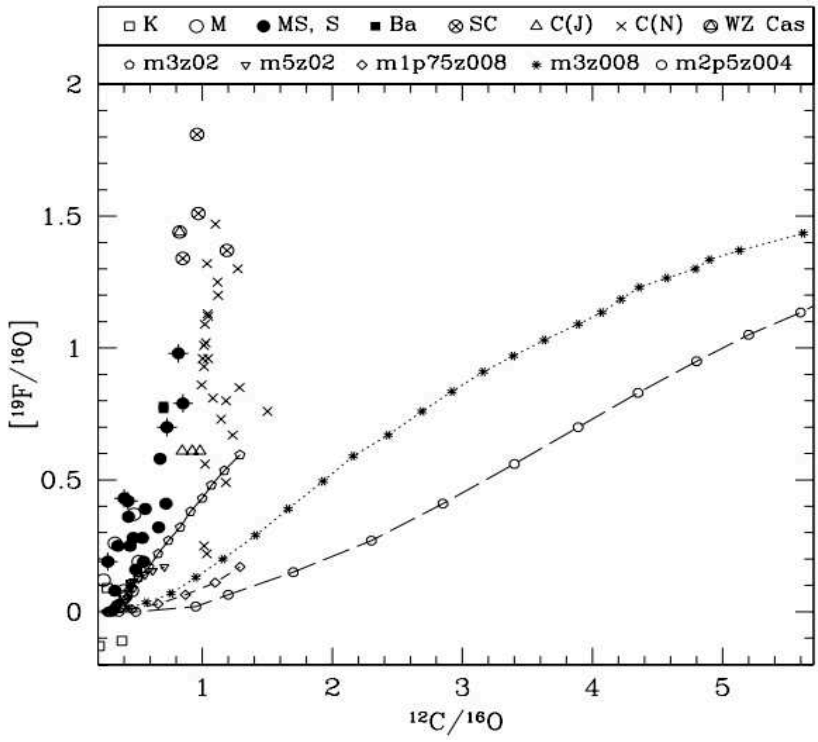

FIGURE 1.13: Comparison of the ^{19}F abundance observed by [8] and the prediction (long dashed, short dashed, dotted and full line) from AGB star models by [9]. Calculations show that even the highest experimentally observed surface fluorine abundances are reproduced for some masses and metallicities, but this occurs for C/O values much larger than what experimental data suggest [9].

The problem of matching the highest observed ^{19}F abundance has been revised by Lugaro et al. [9] by the inclusion of extra mixing processes at the base of the convective envelope, named cool bottom processing (CBP).

This process is described as the circulation of material from the base of the convective envelope into the thin radiative region located on top of the H-burning shell [72], as shown in fig.1.14. Here the material is processed by proton captures and then carried back to the envelope, thus producing the signature of CNO processing at the stellar surface [10].

If the temperature at which the material is carried by CBP is lower than about

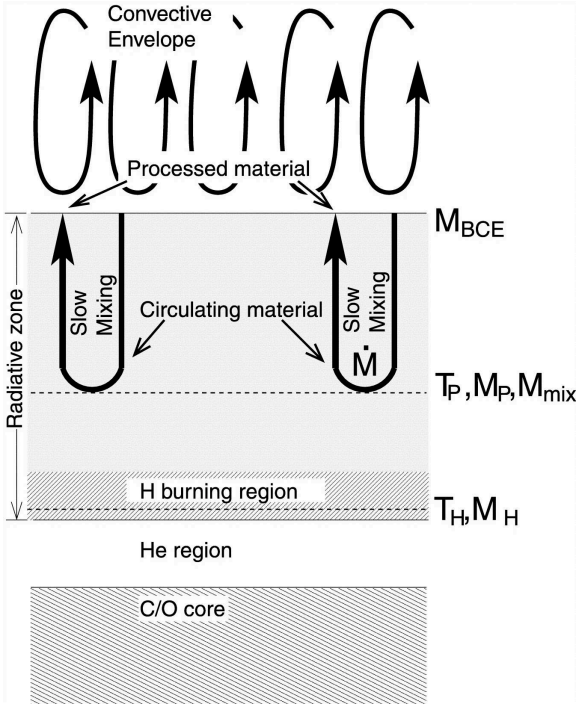

FIGURE 1.14: Schematic diagram of the CBP model. Material taken from the envelope circulates slowly down into the radiative zone, where it undergoes nuclear processing at temperatures near TP, and then back to the envelope where it is rapidly mixed with the other envelope material. The mass coordinate M_P is where $T = T_P$, and M_{BCE} is the bottom of the convective envelope[10]

30 million degrees, at which value the ^{19}F(p, α)^{16}O reaction is activated, then the ^{19}F abundance would be unchanged [9].

Thus, if the extra mixing process is included in model it acts by decreasing the C/O ratio at the surface of the star and leaving the ^{19}F abundance unchanged [9]. The ^{19}F production depends on the amount of ^{13}C in the H-burning ashes, which is a by-product of CNO cycling, and would not be different if the CNO cycling occurs only in the H-burning shell or also at the base of the convective envelope

via cool bottom processing [9]. Then the theoretical curves of fig.1.15 would be simply shifted to the left, making it easier to explain the observed ^{19}F abundances.

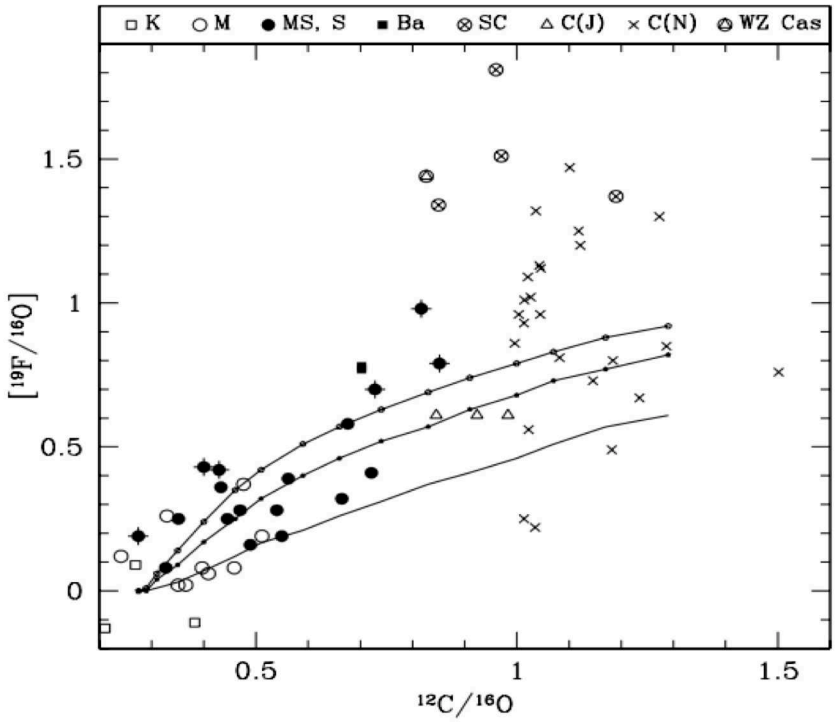

FIGURE 1.15: Comparison of fluorine abundances observed by Jorissen et al. (points) and model predictions (dashed lines) that take into account the partial mixing zone [9].

Abia et. al [71, 73] released two re-evaluations of the fluorine abundances in several stars from the Jorissen study. Abia et al. [71] focused three C stars (see table 1.1) from the Jorissen et al. [8] study and found much lower fluorine abundances that are consistent with solar fluorine abundance. Abia investigated in detail the differences beetween their measurement and Jorissen, and found that because of a possible lack of proper accounting for C-bearing molecules (i.e. CH, CN, CO and C_2) contribution, the F abundances reported in Jorissen et al. for solar metallicity giants had been overestimated.

Fluorine abundance measurements were based on two specific spectral vibration-rotation absorption lines of the HF molecule that Jorissen mostly free of contamination, but the study by Abia used a more complete molecular line list for the synthetic spectra that showed significant contamination of these same lines in carbon-rich stars from ^{12}C^{14}N and ^{12}C^{12}C molecules. Abia abundance measurements relied instead on a different vibration-rotation line of HF that their model

indicated had no contamination [71].

Abia [73] covered a larger variety of AGB stars, including several J-type, SC-type and C-type stars. This study also showed systematic reductions in the fluorine overabundances as compared to Jorissen's paper. The revised fluorine abundances found by Abia for J and C stars [73] are mostly consistent with the solar fluorine abundance.

However, Abia still found a significant fluorine overabundance in SC stars. the SC stars are unique in that both found a nearly equal amount of carbon and oxygen. In turn, slight variations in carbon and oxygen abundances in SC star models result in large variations in the final molecular structure predicted by the models, meaning that there is a far greater uncertainty associated with these SC star measurements than with other AGB stars.

While the results of Abia et al. [71, 73] seem to have reconciled observations and model predictions at solar and slightly subsolar metallicity, large uncertainties in the ^{19}F production in AGB stars, especially in the low-metallicity regime, still exist.

Carbon-enhanced metal-poor (CEMP) stars provide an opportunity to directly measure the F production in low-mass, metal-poor AGB stars. These stars are chemically peculiar objects, characterized by an overabundance of C and low metallicity. Less than a third of CEMP stars exhibit no enhancement in heavy elements (CEMP-no), while most of these objects (over 70%; [74]) are characterized, by an overabundance of n capture, *s* process elements (CEMP-s).

Lucatello et al. [11] F abundance and ^{12}C/^{13}C isotopic ratio measurements or upper limits for a sample of 10 C-rich, metal-poor giant stars. Fig. 1.16 show most of the derived upper limits for F abundance in CEMP-s are not satisfactorily accounted for by nucleosynthetic computations. In fact, the comparison with four of the most recent models for low-mass (2.0 $M_{\odot}$), low-metallicity AGB nucleosynthetic models shows that there are large differences in the predictions between different families of models, which cannot reproduce several of the upper limits, not providing any [F/C+N] ratio predictions low enough to account for the values measured in several of the sample stars [11].

A possible solution that could explain the lowest F upper limit range is the action of CBP, which may reduce the F in the AGB envelope if such extramixing processes expose material at temperatures high enough to activate ^{19}F(p,α) [11].

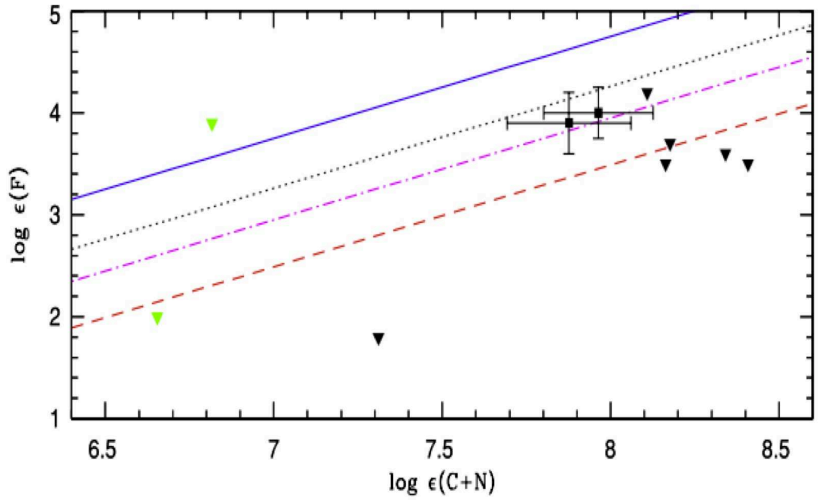

FIGURE 1.16: F abundance as a function of C+N in 10 CEMP stars. The inverted triangles indicate upper limits, green symbols are CEMP-no stars. Theoretical modeling results are indicated by lines. All models are for M = 2 M_{odot} and [Fe/H] = -2.3. [11]

Thus, improvements in the nuclear reaction rate involved fluorine nucleosynthesis , affected by a large number of uncertainties, are needed. Fluorine has also been measured in post-AGB stars and in planetary nebulae [10], the progeny of AGB stars. The large enhancements found in these site (when compared with the solar fluorine abundance) supported the idea of AGB stars as producer of fluorine [75].

[10]Planetary nebulae are composed of the material ejected into the interstellar medium by AGB stars.

1.7 Termination of the AGB evolutionary phase

Depending on the initial mass and the mass loss rate, AGB stars will have very different fates.

The low mass AGB stars will finally become carbon stars due to several third-dredge-up episodes which cause a significant amount of carbon to appear on the stellar surface.

For the intermediate-mass AGB stars, this phase of evolution is finally terminated by severe mass loss over the last 2 - 3 helium-shell-flash cycles through strong stellar winds.

All along the thermal pulsating AGB phase, the star undergoes moderate to strong mass loss that allows the injection of the different elements synthesised inside the star into the interstellar medium. At the end of the TP-AGB phase, the star ejects its envelope becoming planetary nebulae contribute pre-biotic materials to the interstellar medium and the next generation of stars [66].

The mass loss is dominated by the helium flashes or the thermal pulses. If the thermal pulse phase is sufficiently long, the flash forces the mass outflow from the stellar surface to be accelerated and the star will expand rapidly until the gas becomes cool enough that heavy elements can condense into dust grains. The composition of this dust component is also partly dependent on core nuclear burning and thus initial stellar mass, as the resultant elemental abundance from core burning in relatively low mass AGB stars is carbon, while the products from core burning in intermediate to high mass stars will contribute oxygen, nitrogen and silicates to the circumstellar shell. These carbon and silicate grains are the major dust component of proto-planetary nebulae (PPN) [76]. In many planetary nebulae the central stars are burning hydrogen, in other helium, indicating that there may be a number of final thermal pulses that eject the hydrogen envelope. Once this hydrogen or helium is exhausted, all that is left is a degenerate C-O core [76]. This is due to the fact that such stars are not able to burn carbon in their cores, and as a result the white dwarf mainly consists of carbon and oxygen.

1.8 Pre-solar Grains

In the last 20 years it has become possible to study Presolar grains recovered from pristine meteorites. These grains have survived the formation of the solar system as individual microcrystals and they carry the signature of their condensation environment [77].
A wide variety of such grains have been discovered. The first to be recovered from meteorites were carbon-rich grains including silicon carbide (SiC), graphite and diamond [78].
AGB stars of low mass and around solar metallicity have been identifyed as the most likely parent stars of mainstream SiC [11], the major group of presolar SiC grains found in meteorites, [79]. In fact, these objects contain trace amounts of heavy elements showing the signature of the *s* process, such as Kr, Ba, Nd and Sm and enhancement of ^{128}Xe and ^{130}Xe, which are isotopes associated with the *s*process [80, 81].
These features suggest that these grains are formed in the envelopes of low-mass TP-AGB stars which should be rich in carbon and *s*process elements due to the action of TDU. Conversely, it is unlikely that the bulk of the grains had formed in intermediate-mass AGB stars since the formation of carbon-rich stars in this mass range is inhibited by the occurrence of HBB.

The relatively high precision of the measurements of the isotopic composition of trace heavy elements in single SiC of the size of micrometers provide constraints on theoretical models of the *s* process, on neutron-capture cross sections and on the conditions in the interior of AGB stars. By comparing models of the *s*process in AGB stars with observed *s*process element ratios is possible to constrain which neutron are activated and hence the temperatures reached in thermal pulse.

Measurements of pre-solar grains have also suggested the requirement for additional physics not included in standard stellar evolution codes and provide important new information about mixing processes in low-mass AGB stars.
The idea that extra-mixing processes are operating in AGB stars is supported by the C, O, and N isotopic ratios found in meteoritic silicon carbide and oxide grains from AGB stars [3].

[11] SiC grains originated in low-mass ($<2M_{\odot}$) AGB stars from roughly solar-metallicity stars [12].

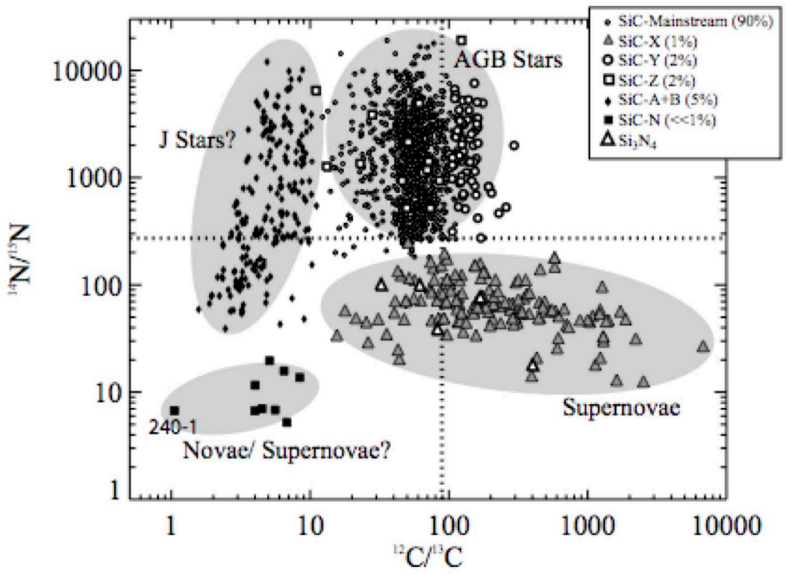

FIGURE 1.17: C and N isotopic ratios measured in individual presolar SiC grains[12]. Five different groups can be distinguished on the basis of their abundances in the meteorites, given in the legend. The dotted lines represent the solar initial values.

The C and N ratios in presolar SiC grains and the isotopic ratios for $^{18}O/^{16}O$ and $^{17}O/^{16}O$ in oxide grains, cannot be explained by the action of first and second dredge-up [82].

As shown in fig.1.17, the measured $^{12}C/^{13}C$ ratios spread to lower values than the solar ratio, while the $^{14}N/^{15}N$ ratios spread both above and below the solar one. These data requir that material be transported from the cool convective stellar envelope to hotter layers of the star where could be depleted. The physical mechanism of the extra mixing (CBP, [83], see 1.6) is unknown,but may be related to shear instabilities, thermohaline instabilities and/or magnetic effects and it is necessary in order to explain Sic grain data with lower $^{12}C/^{13}C$ ratios and higher $^{14}N/^{15}N$ ratios than those covered by the line predicted by the models in fig.1.17 and is also believed to be necessary in order to generate a ^{13}C pocket to provide a neutron source necessary for the *s*process [12].

As said in section 1.6, this extra-mixing processes are required in order to reproduce the large observed fluorine abundances because may reduce the F in the AGB envelope through the $^{19}F(p,\alpha)$

Chapter 2

Thermonuclear Reaction Rates

Nuclear reactions play a key role in the production of energy and nucleosynthesis in stars. The kinetic energy available to particles in stellar interiors is that of their thermal motions, and hence the reactions which are induced by this motion are called thermonuclear reactions [38].
As was mentioned in the previous chapter, heavy elements are synthesized in the stellar interior by various thermonuclear reactions that occur in different stages of stellar evolution. For these reasons it is worthwhile to discuss the subject of thermonuclear reaction rates in more detail.
This chapter presents the stellar nuclear reaction rate theory and describes the determination of stellar reaction rates.

2.1 Stellar Thermonuclear Reaction

Thermonuclear reactions are denoted as X(a, b)Y , where the nucleus X reacts with the particle a and transforms to the element Y with the release of the particle.

$$X + a \rightarrow Y + b \tag{2.1}$$

The energy consumed or produced by the reaction (the Q-value of reaction) is defined by the relativistic relation:

$$Q = (m_X + m_a - m_Y - m_b)c^2 \tag{2.2}$$

where m is the mass of interacting particle. For example, the main reactions in the stellar burning which involve particles lighter than iron are esoenergetic (Q > 0) and the Q-value represent the energy liberated for each reaction.
To obtain the energy produced by nuclear reactions per second, the first step is to calculate the probability that a given nuclear reaction will take place. This is proportional to the cross section σ.
Consider a gas of particles x with density N_x and particles a with a density N_a per cubic centimeter, and velocities v_x and v_a with relative velocities v.
Since the cross section only depends on the relative velocity v, one can assume either particles of type x or a as the projectiles with velocity v. If we assume x to be projectiles, then the particles a must be considered at rest. Consequently, the projectiles see N target nuclei per cubic centimeter, and each target nucleus has an area σ(v). Thus, we define the reaction rate per unit volume r as [1]:

$$r = N_x N_a v\sigma(v) \tag{2.3}$$

where:

- σ(v)N_a is the effective cross section. In fact, the projectiles see N target nuclei per cubic centimeter, and each target nucleus has an area σ(v). Thus, the effective area per cubic centimeter that the projectiles see equals the cross section for a single target nucleus multiplied by the number of target nuclei per cubic centimeter.

- vN_x is the flux of particles x, v defined as the relative velocity between these two particles and σ(v) the probability that this reaction will occur.

In this equation, r is in units of reactions per cubic centimeter per second.
In the stellar gas both types of nuclei are moving and the product between cross section and particle velocity has to be averaged over the probability ϕ(v) [1]:

$$< \sigma v >= \int_0^\infty \phi(v) v\sigma(v) dv \tag{2.4}$$

The quantity $< \sigma v >$ is referred to as the reaction rate per particle pair.
It follows that the reaction rate becomes:

$$r = N_x N_a < \sigma(v) > \tag{2.5}$$

If the reacting particles are identical, a factor $\frac{1}{2}$ must be taken into account in the previous equation, for otherwise we would count each pair twice. So, we can introduce a Kronecker symbol δ_{xa} and equation 2.5 should be rewritten in the following way [84]:

$$r = NxNa < \sigma(v) > (1 + \delta_{xa})^{-1} \tag{2.6}$$

The velocities in stellar AGB environment are described by a non degenerate gas (the stellar gas is almost always non-degenerate exceptions are white dwarfs and neutron stars for which $\rho >10^{14}$ g cm^{-3}).
Moreover, the gas can be considered as in thermodynamic equilibrium and non relativistic, thus the velocity distribution follow the Maxwell-Boltzmann law:

$$\phi(v) = 4\pi v^2 \left(\frac{m}{2\pi kT}\right)^{\frac{3}{2}} e^{\left(-\frac{mv^2}{2kT}\right)} \tag{2.7}$$

such that k is Boltzmann's constant and T the gas temperature.
From equations 2.5 and 2.7 and using the center of mass kinetic energy E=$\frac{1}{2}\mu$v^2, where $\mu = \frac{m_x m_a}{(m_x + m_a)}$ is the reduced mass, the reaction rate per particle pair can be written:

$$< \sigma v >= \left(\frac{8}{\pi\mu}\right)^{\frac{1}{2}} \frac{1}{(kT)^{\frac{3}{2}}} \int_0^\infty \sigma(E) E e^{(-\frac{E}{kT})} dE \tag{2.8}$$

With these assumptions, the stellar thermonuclear reaction rate is given by:

$$r = N_x N_a \left[\left(\frac{8}{\pi\mu}\right)^{\frac{1}{2}} \frac{1}{(kT)^{\frac{3}{2}}} \int_0^\infty \sigma(E) E e^{(-\frac{E}{kT})} dE\right] (1 + \delta_{xa})^{-1} \tag{2.9}$$

This integral has to be evaluated from zero energy to infinity only if the reaction is esoenergetic, since in this case no reaction thresholds must be taken into account; otherwise, if Q<0, the integration has to be performed between the reaction threshold and infinity.

2.2 Coulomb Barrier, Penetration Factor and The Astrophysical Factor

The reaction rate is related to the reaction cross-section σ, which can be measured experimentally. The cross-section is essentially a measurement of a reaction probability.

Let us concentrate in the case of a reaction between two charged particles. One of the reasons the determination of the cross section at stellar temperatures is an interesting problem is the fact that are needed for a comprehensive analysis of stellar energy production and to explain the variety of elements and isotope abundances. But, coulomb repulsion is extremely strong to allow nuclear reactions to happen frequently, thus giving values of the cross section sometimes too tiny to be measured.

Nuclear interactions only occur over distances on the order of fm (10^{-15} m). However, the Coulomb force repelling the two particles acts over a much longer distance. The distance of closest approach, r_C, corresponds to the point where the potential energy reaches that of the initial energy of the approaching particle, E. Let us consider the reaction between a charged projectile and a charged target. For the reaction to take place the projectile must penetrate the Coulomb barrier of the target nucleus. The Coulomb potential has the form of equ. 2.10 and is illustrated in fig.2.1.

$$V = \frac{Z_1 Z_2 e^2}{r} \tag{2.10}$$

Classically, fusion would only be possible if projectile nuclei had enough energy to overcome this Coulomb barrier. If the projectile has energy less than E_C, the Coulomb barrier height, it is turned away at the classical turning point.

The Coulomb barrier height is related to the charges of projectile and target nuclides, so burning involving higher Z nuclides requires higher energies and so

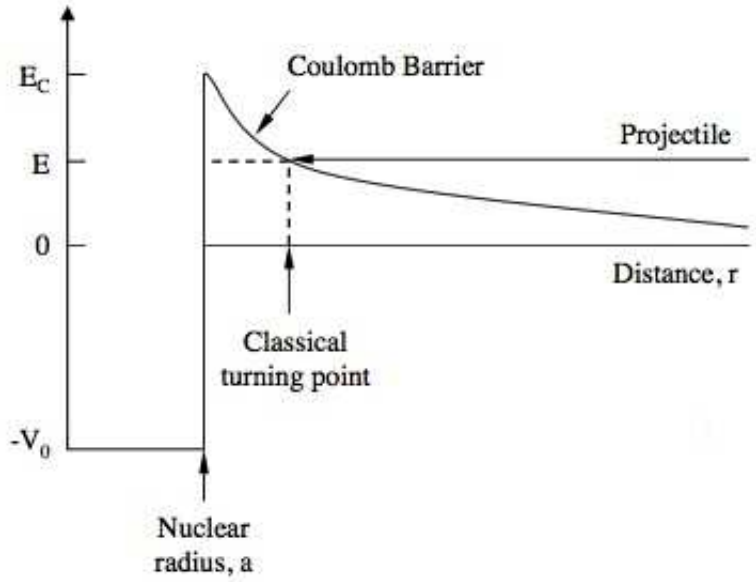

FIGURE 2.1: Sketch of the Coulomb barrier. The plot reports the total potential V(r) versus the relative distance r between the two interacting particle.

higher temperatures.

For r_C on the order of fm, the Coulomb Barrier is on the order of MeV. For example, in the ^{19}F-p reaction, the energy necessary to overcome the Coulomb barrier is 2.5 MeV. For most stellar environments, the average kinetic energy of the nuclei, kT is on the order of keV. In fact, even if temperatures are quite high in stellar core, usually thermal energies ranging from few keV in quiescent phenomena up to few hundreds of keV in some explosive events, because of the smallness of the Boltzmann constant

$$kT = 8.62x10^8 T(keV) \tag{2.11}$$

A particle will very rarely have an energy greater than the Coulomb barrier, so most reactions would be classically forbidden.

The only possibility for occurrence of the thermonuclear reactions in stars comes from a quantum mechanical effect found by G. Gamow [85]: there is a small but finite probability of penetrating (tunneling) through the Coulomb barrier, even if the particle energy is less than that of the barrier.

This tunneling occurs with a characteristic energy-dependent probability called penetrability, P_l and is given by [84]:

$$P_l = \frac{|\chi_l(\infty)|^2}{|\chi_l(R)|^2} \tag{2.12}$$

where $|\chi_l(\infty)|^2$ represents the probability of finding the particles at the interaction radius and $|\chi_l(R)|^2$ represents the probability of finding the particles at the classical turning point of the Coulomb barrier.
It can be calculated by solving the radial part of the Schrödinger equation:

$$\frac{d^2\chi_l}{dr^2} + \frac{2\mu}{\hbar^2}[E - V_l(r)]\chi_l = 0 \tag{2.13}$$

where V_l(r)is the potential for the l^{th} partial wave resulting when the centrifugal potential term is also present [84]. The general solution is:

$$\chi_l(r) = AF_l(r) + BG_l(r) \tag{2.14}$$

At low energies or, equivalently, where the classical turning point is much larger than the nuclear radius, equation 2.13 has two independent solutions: the regular F_l(r) and irregular G_l(r) Coulomb wave function for a given relative orbital angular momentum l differ for their behaviour at the origin since the former vanishes for r=0 while the latter diverges.
Thus, the equation 2.12 takes the form:

$$P_l = \frac{kr}{F_l^2 + G_l^2} \tag{2.15}$$

For low energies, the s-wave component (orbital angular momentum equals zero, l=0) can be approximated by

$$P_0 \approx e^{(-2\pi\eta)} \tag{2.16}$$

The quantity η is the so-called Sommerfeld parameter and is equal to:

$$\eta = \frac{Z_1 Z_2 e^2}{\hbar\nu} \tag{2.17}$$

where Z_1 and Z_2 are the atomic numbers of the particles, $\hbar$ the reduced Planck constant, e the proton charge and ν the relative velocity of the particles, given by :

$$\nu = \frac{\hbar k}{\mu} \tag{2.18}$$

where k is the wave number:

$$\nu = \left(\frac{2\mu|E|}{\hbar^2}\right)^{\frac{1}{2}} \tag{2.19}$$

The Sommerfeld parameter is a measure of the Coulomb interaction intensity since η is the higher the larger is the product of the charges of the interacting ions, yet it decreases when the kinetic energy increases, as the interaction time is shorter. The penetration through the angular momentum barrier is not included in this approximation, which would affect reactions with l$\neq$ 0.
At low energy, below the Coulomb barrier, tunneling probability has an approximate expression that drops exponentially with the equ. 2.16:

$$P_0 \approx e^{(-2\pi\eta)} \approx e^{-\left(\frac{E_G}{E}\right)^{\frac{1}{2}}} \tag{2.20}$$

Here E_G is called the Gamow energy and is given by

$$E_G = 2\mu(\pi\eta\nu)^2 = 0.978(Z_1Z_2)^2\mu(MeV). \tag{2.21}$$

The cross section should be proportional to the effective geometrical area $\pi\lambda^2$ seen by the particle pair during the collision, as well a geometric factor $\frac{1}{E}$ to account for the size of the nucleus [1]:

$$\sigma \sim \pi\lambda^2 \sim \left(\frac{1}{p}\right)^2 \sim \frac{1}{E} \tag{2.22}$$

where p is the linear momentum and λ the de Broglie wavelenghth.
Therefore the cross section can be written as:

$$\sigma(E) \propto \frac{1}{E}e^{-2\pi\eta} \tag{2.23}$$

In the previous equation is included the non-nuclear contribution to the reaction cross section: all the intrinsically nuclear effect are contained in the proportionality constant, called astrophysical S(E)-factor:

$$S(E) = \sigma(E)Ee^{2\pi\eta} \tag{2.24}$$

In this way we may write:

$$\sigma(E) = \frac{1}{E} S(E) e^{-2\pi\eta} \tag{2.25}$$

Writing the cross section as in equation 2.25 is purely for convenience as the S-factor has no physical meaning; nevertheless it is very useful in removing the strong energy dependence of the cross section, usually spanning several orders of magnitude in a small energy region, thus enhancing the visualization of the resonant nature of the reaction.

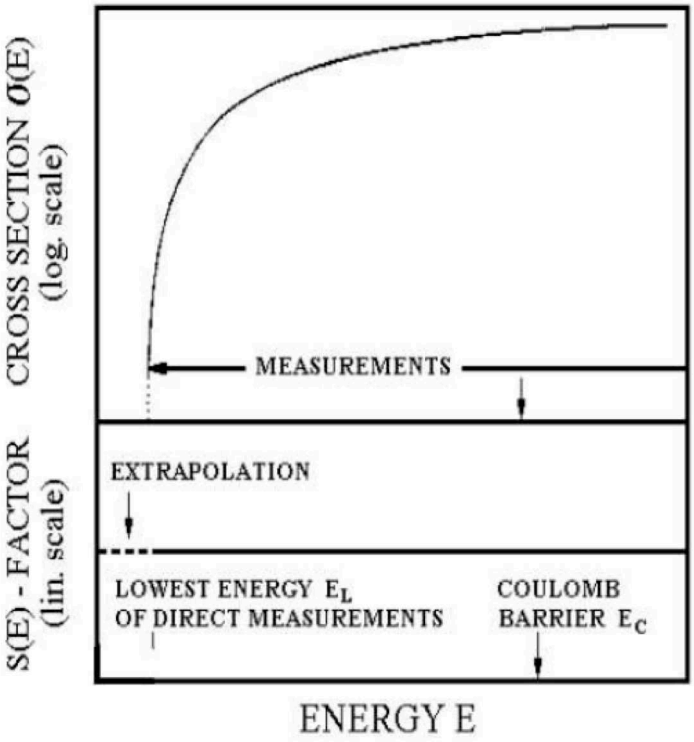

FIGURE 2.2: Comparition of the low-energy behaviour of the cross section (upper panel) and of the S(E)-factor (lower panel) for a non-resonant reaction.

Since the use of extrapolation to deduce the low-energy behaviour of reaction cross sections of astrophysical relevance is often necessary, because it is typically very difficult to measure the cross sections at astrophysical energies (E $\approx$ keV), the astrophysical factor is convenient due to the slow, continuous variation of S(E) with energy when resonances are not present, compared to the other cross-section factors, which vary rapidly with energy.

Figure 2.2 shows that S(E) varies much less rapidly with beam energy than the cross section and it allows an easier procedure for extrapolating the energy behaviour at astrophysical energies.
As such, it is often the practice to measure cross sections at higher energies, extract the S-factor, and then extrapolate this factor to lower energies.

2.3 Non-Resonant Reaction Rates

The introduction of the S(E)-factor is also very useful to derive an analytical expression of the reaction rate in the case of non-resonant reactions.
If equation 2.2 is inserted into equation 2.8, the reaction rate can be written as:

$$\begin{aligned} < \sigma v > &= \left(\frac{8}{\pi\mu}\right)^{\frac{1}{2}} \frac{1}{(kT)^{\frac{3}{2}}} \int_0^\infty \sigma(E) E e^{(-\frac{E}{kT} - 2\pi\eta)} dE = \\ &= \left(\frac{8}{\pi\mu}\right)^{\frac{1}{2}} \frac{1}{(kT)^{\frac{3}{2}}} \int_0^\infty \sigma(E) E e^{\left[-\frac{E}{kT} - \left(\frac{E_G}{E}\right)^{\frac{1}{2}}\right]} dE \end{aligned} \tag{2.26}$$

The integrand of the equation 2.26, because of the limited dependence of S(E) from E, is governed by the combination of two exponential terms [1]:

- the first exponential term in the integral ($e^{-\frac{E}{kT}}$) is a measure of the number of available particles in the high-energy tail of the Maxwell-Boltzmann distribution, and this term decreases with energy, therefore is only important at low energies;
- the second exponential ($e^{-\frac{E_G}{E}}$) is related to the penetration through the Coulomb barrier which drops exponentially at lower energies, hence it is non negligible only at higher energies.

The product of the two terms as shown in fig.2.3, gives rise to a peak of the integrand in equation 2.26 at an energy E_0. This peak is referred to as the Gamow peak, and it is the most effective energy region for thermonuclear reactions to occur.
If no resonance appears, the astrophysical S-factor is often assumed to be constant

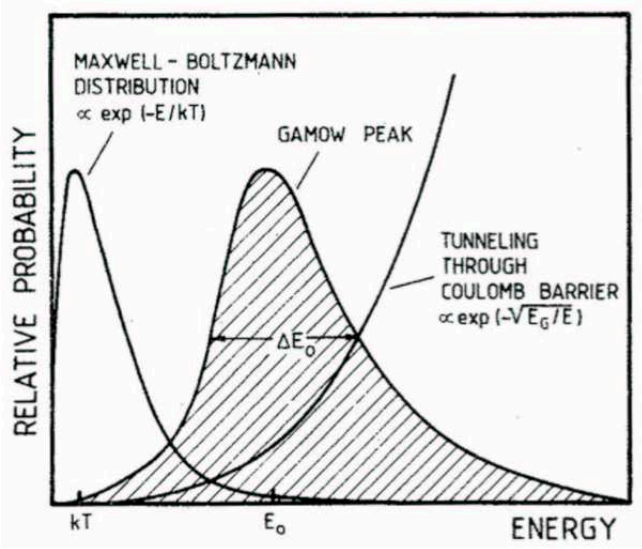

FIGURE 2.3: The Gamow Peak (shaded), resulting from convolution of the Maxwell-Boltzmann distribution and the penetrability.

over the energy range close to the Gamow peak.

$$S(E) = S(E_0) = S_0 = constant \tag{2.27}$$

At the temperatures of interest in stellar reactions the product of these exponentials produces a function which looks not dissimilar to a Gaussian. This function is called the Gamow window. It is peaked at the effective burning energy, E_0, which is determined by finding the energy at which the integrand in equation 2.26 is a maximum. By setting the first derivative of equation 2.26 to zero, one finds E_0 to be:

$$E_0 = \left(\frac{kT}{2}\right)^{\frac{2}{3}} E_G^{\frac{1}{2}} = 1.22[(Z_1 Z_2)^2 \mu T_6^2]^{\frac{1}{3}} (keV) \tag{2.28}$$

This means that with increasing stellar temperature and numbers the Gamow peak is shifted toward higher energies.

Referring to fig.2.3, the arrow is the $\frac{1}{e}$ width of the peak, which is the effective width Δ (the Gamow window). For a given stellar temperature T, nuclear reactions take place in this relative narrow window around the effective burning energy E_0. This width is calculated from finding the extremum of the second derivative of the integrand in equation 2.26 and is equal to [1]:

$$\Delta = \frac{4}{\sqrt{3}} (E_0 kT)^{\frac{1}{2}} = 0.749 (Z_1^2 Z_2^2 \mu T_6^5)^{\frac{1}{6}} (keV) \tag{2.29}$$

Thus, $E_0 \pm \frac{\Delta}{2}$ is the energy range where the nuclear reactions will most likely occur at a given temperature T and it is related to the Coulomb barrier of the interacting nuclei: it will be higher when the Coulomb barrier will be increased. For example, at temperature of T=15 x 10^6 K, typical of the sun core, the E_0 value for some reactions is:

	$\mathbf{E_0}$ **(keV)**	$\mathbf{\Delta/2}$ **(keV)**
p+p	5.92	3.2
^{14}N+p	26.5	6.8
α +^{12}C	56	9.8
^{16}O+^{16}O	237	20.2

TABLE 2.1: Gamow energy and width of the Gamow peak evaluated at the temperature of the solar core [1].

As can be seen in fig. 2.3, the peak of the Maxwell-Boltzmann distribution, kT, is much smaller than the Gamow peak, E_0, which is in turn much smaller than the Coulomb barrier. Thus, the cross section at the Gamow energy is on the order of 10^{-12} to 10^{-9} barn (barn = 10^{-28} m^2), corresponding to experimental counting rates ranging from a few events per day to a few events per month under typical laboratory conditions; hence, it is difficult to measure the cross section directly at the Gamow energy. The usual procedure to measure the cross section is measuring it over as wide a range as possible, and then extrapolate down.

The concept of the Gamow window can be extended to reaction regimes different from the non-resonant mechanisms. In fact, the majority of non-resonant reactions occur within energies of $E_0 \pm \frac{\Delta}{2}$; but the total reaction rate can however be dominated by resonant reactions within the Gamow window.

An example of a non-resonant reaction is direct capture [1]. In direct capture the products of the reaction emerge without a transitional state, as opposed to resonant capture where a compound nucleus is first formed as will be seen in the following section.

In addition to non-resonant processes, the energy of the projectile nucleus can be such that will cause the two particles to resonate in a quasi-stationary state of the compound nucleus [1]. In this case, the reaction is called a resonant reaction and

[1]Compound nucleus formation is a reaction mechanism in which two nuclei combine into a single excited nucleus, called the compound nucleus. The compound nucleus lives for a relatively

the calculation of its rate is significantly different from what was presented in this section. The next section is allocated to a discussion of resonant reaction rates.

2.4 Resonant Reaction Rates

The previously derived reaction rate expression relies on the smooth variation of the S-factor with energy for non-resonant (direct) reactions. However, very often, resonant reactions can take place where the two nuclei can fuse together into an excited state with energy E_r of the of a compound nucleus in the entrance channel, and then decay to lower-lying state [86].
Schematically the process has the form:

$$x + a \rightarrow [C^*] \rightarrow y + b \tag{2.30}$$

Reactions occurring under such conditions are called resonant reactions. In contrast to the direct capture mechanism which can occur for all energies of the projectile, the resonant reactions can only happen if the energy of the entrance channel Q + E_x matches the energy E_r of the excited state in the compound nucleus [1]. Thus $E_x = E_r - Q$ where Q is the threshold energy required for the reaction to happen and E_x is the incoming projectile energy. So, when the energy of the reduced mass system is such that it is equal or close to the energy of a resonance state in the compound system, the cross section of the reaction is significantly enhanced. This sudden increase in the cross section is due to the fact that at energies equal or close to the resonance energy, the amplitude of the wave function for the entrance channel matches that of the quasi- stationary state.
As a first approximation, the energy dependence of the cross section for an isolated (for wich the total width Γ is much smaller than the average energy spacing between two consecutive resonances, $|E_2 - E_1| > \Gamma$ as it is shown in fig. 2.5) and narrow (for which the resonance energy is large compared with their total widths, $\Gamma << E_r$, can be seen in fig. 2.4) resonance can be written as a Breit-Wigner function [1]:

long time and forgets how it was formed. It then transforms into lighter nuclei by a decay, or by fission.

$$\sigma(E)_{BW} = \pi\lambda^2 \frac{2J+1}{(2J_x+1)(2J_a+1)}(1+\delta_{xa})\frac{\Gamma_1\Gamma_2}{(E-E_r)^2+(\Gamma/2)^2} \tag{2.31}$$

where:

$\lambda = \frac{\hbar}{\sqrt{2\mu E}}$ is the center of mass de Broglie wavelength (μ is the reduced mass);
J is the angular momentum of the resonance and J_x and J_a are the spins of particles x and a in the entrance channel (target and projectile);
$(1+\delta_{xa})$ is a factor that ensures that identical reacting particles are not counted twice;
E is the energy of the projectile and E_r is the resonance energy;
Γ_1 and Γ_2 are the partial widths of the entrance and the exit channels of the reaction describing the formation and the decay of the compound nucleus and Γ is the total width defined as the sum of the partial widths for all open reaction channels $\Gamma = \Gamma_1 + \Gamma_2 + ...$

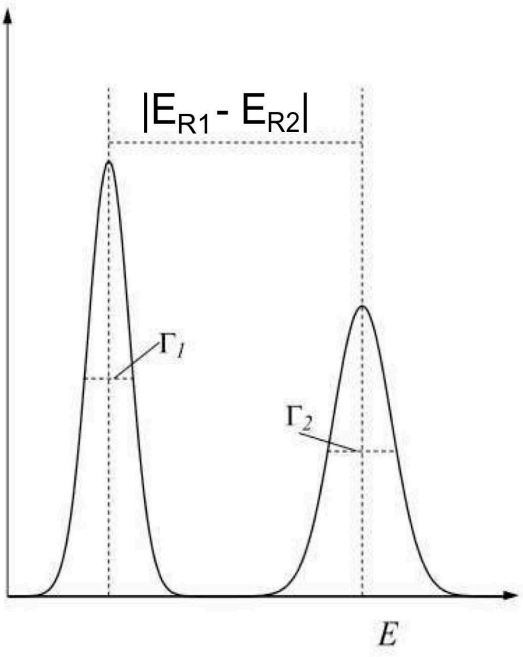

FIGURE 2.4: Two isolated resonances. The resonance energy is large compared with their total widths.

The partial widths express the probability for a compound nucleus to be formed or decay through a particular channel.
The total width is related through the uncertainty principle to the mean lifetime

of the quasistationary state of the compound nucleus

$$\Gamma = \sum_i \Gamma_i = \frac{\hbar}{\tau} \tag{2.32}$$

where τ is the mean lifetime of the resonance and Γ_i are the partial widths of the resonance. The partial widths of a resonance can be thought of as the inverse of the partial lifetimes of a resonance

$$\frac{1}{\tau} = \sum_i \frac{1}{\tau_i} \tag{2.33}$$

This concept then leads to the branching ratio of a resonance:

$$BR_i = \frac{\Gamma_i}{\Gamma} \tag{2.34}$$

which is the probability that a resonance will decay (or be populated) through the ith decay channel.

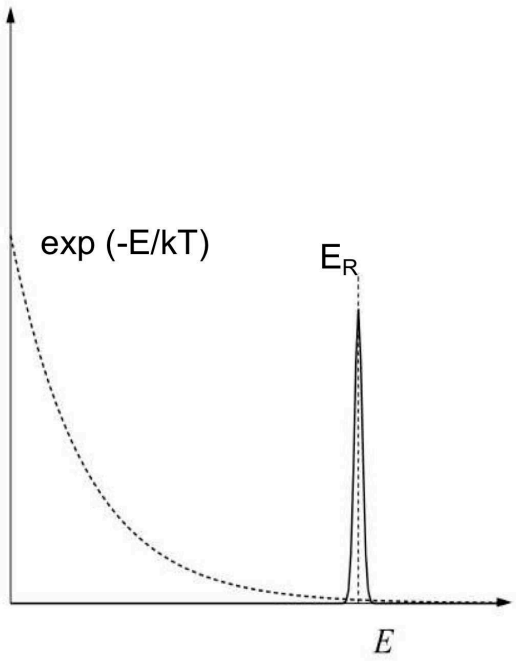

FIGURE 2.5: An isolated and narrow resonance.

By plugging equation 2.31 into equation 2.8, we obtain:

$$< \sigma v >= \left(\frac{8}{\pi\mu}\right)\frac{1}{2}\left(\frac{1}{kT}\right)\frac{3}{2}\int_0^\infty \sigma_{BW}(E)Ee^{\left(-\frac{E}{kT}\right)}dE \tag{2.35}$$

All the widths in equation 2.31 are energy dependent.

If the case of narrow resonances, like the one reported in fig. 2.4, for which the total width Γ of the resonance is much smaller than the resonance energy (typically, if $\frac{\Gamma(E)}{(E_r)}$) <0.1 [1]), then the Maxwell-Boltzmann exponential factor ($Ee^{\left(-\frac{E}{kT}\right)}$) and the partial widths can be evaluated at the resonance energy E = E_r, since only a narrow range of width $\sim \Gamma$ contribute to the integral, and we can then pull them out of the integral:

$$< \sigma v >= \left(\frac{8}{\pi\mu}\right)\frac{1}{2}\left(\frac{1}{kT}\right)\frac{3}{2}E_r e^{\left(-\frac{E_r}{kT}\right)}\int_0^\infty \sigma_{BW}(E)dE \tag{2.36}$$

This can be done since in the case of narrow resonances, all of these factors will be smooth functions of energy that vary very slowly over the widths of the resonances, which is narrow [84].
Moreover, the energy depence of the total and partial widths can be neglected across the resonance, so that:

$$\int_0^\infty \sigma_{BW}(E)dE = \frac{1}{2}\lambda_r^2\frac{2J+1}{(2J_x+1)(2J_a+1)}(1+\delta_{xa})\frac{\Gamma_1\Gamma_2}{\Gamma} = \frac{1}{2}\lambda_r^2\omega\gamma \tag{2.37}$$

where

$$\omega = \frac{2J+1}{(2J_x+1)(2J_a+1)}(1+\delta_{12}) \tag{2.38}$$

and

$$\gamma = \frac{\Gamma_1\Gamma_2}{\Gamma} \tag{2.39}$$

and γ_r is the de Broglie wavelength evaluated for E=E_r.
The product $\omega\gamma$ is the so-called resonance strength and E_r is the resonance energy. These two terms are the nuclear physics dependent terms in the reaction rate. By plugging equation 2.37 into equation 2.36, we obtain

$$< \sigma v >= \left(\frac{2\pi}{\mu kT}\right)^{\frac{3}{2}}\hbar^2\omega\gamma e^{\left(-\frac{E_r}{kT}\right)} \tag{2.40}$$

The exponential term indicates that at given stellar temperature the reaction rate is dominated by resonances with energy E_r close to kT. Thus it is very important to measure the resonance energies which lie in the Gamow window as precisely

as possible, since the contribution of these resonances to the reaction rate is very significant.

In the presence of several narrow resonances, the total resonant reaction rate per particle pair simply varies as the sum of the individual resonance contributions:

$$< \sigma v >= \left(\frac{2\pi}{\mu kT}\right)^{\frac{3}{2}} \hbar^2 \sum_i (\omega\gamma)_i e^{\left(-\frac{E_r^i}{kT}\right)} \tag{2.41}$$

Substituting all the constants into the equation

$$N_A < \sigma v >_R = 1.54X10^{11} x(\mu T_9)^{\frac{3}{2}} \sum_i (\omega\gamma)_i e^{\left(-11.605X\frac{E_i}{T_9}\right)} \tag{2.42}$$

where N_A is the Avogadro number, $N_A < \sigma v >_R$ is the resonant reaction rate in units of $cm^3 mole^{-1} s^{-1}$, μ is the reduced mass, $(\omega\gamma)_i$ is the resonance strength in units of MeV for the state i, and E_i is the corresponding resonance energy in the center of mass system in units of MeV.

Finally, in the case of broad resonances, when the total width is comparable with the resonance energy ($\frac{\Gamma}{E_r}$ >0.1), the energy dependence of the partial widths must be retained and they cannot be pulled out of the integral. In order to calculate the reaction rate per particle pair, one must then evaluate equation 2.31 taking into account the energy dependence of the cross section.
The cross section behavior as the energy varies is described with

$$\sigma(E) = \sigma(r)\frac{E_r}{E}\frac{\Gamma_1(E)}{\Gamma_1(E_r)}\frac{\Gamma_2(E)}{\Gamma_2(E_r)}\frac{(\frac{\Gamma_r}{2})^2}{(E-E_r)^2 + [\frac{\Gamma(E)}{2}]^2} \tag{2.43}$$

where σ_r is the value of the cross section at the resonance energy E_r.
Since the low-energy tail of a broad resonance is a smoothly varying function of energy, can be treated similarly to the non resonant case, with the difference that the S factor at the Gamow energy can be expressed in terms of the parameters of the resonance contributing with its tail to the cross section.

Another kind of the cross-section behavior for resonant reaction is related to the presence of a subthreshold resonance: if the energy E_r of the level C^* of the compound nucleus C does not exceed the Q-value for the reaction, a cross section

increase in the low-energy region will occur.
In this case the resonance peak lies below the interaction energy where the tail of this resonance will influence the behavior of the S-factor in the region relevant for the astrophysical investigation.

2.5 R-Matrix theory of compound nucleus reactions

The R-Matrix formalism is a parameterisation of the properties of compound nucleus reactions. It is of prime importance to note that R-matrix theory is not, by itself, a predictive theory. The theory should be thought of as a framework which needs the input of experimental data in order to have any real physical significance [87]. The more data that is available, the more the nuclear wave functions are constrained, and the more reliable it becomes when attempting to use the theory to extrapolate to nearby unobserved energy regions.
For this reason an analysis usually starts with a simpler analysis, Breit-Wigner for example, in order to obtain an estimate of the partial widths, energies, and spin-parities of the resonances (level parameters). Once this is complete, these roughly determined values can be used as a starting point for the R-matrix analysis. By performing a least squares fitting of the R-matrix parameters to cross section data, more accurate level parameters and the interference signs between the resonance can be obtained.

The basic assumptions of the theory are as follows [88]:

- Non-relativistic quantum mechanics must be applicable to the reaction. This is a reasonable approximation in low energy nuclear physics because the kinetic energies inside nuclei are much smaller than their respective rest masses;
- the theory assumes only two nuclei in the entrance channel and that the processes involved in this measurement do not lead to the production of more than two nuclei in the exit channel;

- the most striking assumption of the theory is the existence of a definite nuclear radius, namely a, defined as the minimum radial distance of separation at which neither nucleus fells the presence of the other. This radius represents a division between the internal region (r<a), where we consider only the short range nuclear force and where the nuclear potential has an effect (in this region the physics of the problem is given by the R-matrix parameters), and the external region, outside the nuclear potential, where we assume no strong nuclear interactions take place between the two particles. Outside this radius the only force acting between the two particles is the Coulomb force. This also means that the R-matrix radius parameter for a given particle channel must be made large enough to contain the nucleus.

We can then proceed to construct a mathematical description of the properties of the wavefunctions in the internal (within the channel radius) and external (outside the channel radius) regions separately. The following discussions follow mainly the formalism of ref [88].

2.5.1 Construction of internal and external wavefunction

The R-matrix aims to solve the Schrödinger equation,

$$H\Psi = E\Psi \tag{2.44}$$

It is assumed that the wave function can be solved by the technique of separation of variables. Then solutions are obtained for the internal and external regions of the configuration space. Relations are then derived with the assumption that the solutions must match at the R-matrix boundary radius.
It is useful at this point to use a simplified physical situation such as the scattering of a spinless particle by a central potential V(r) to derive the basic equations relating the wavefunctions and properties of the compound nucleus to the R-Matrix parameters.

2.5.1.1 Internal Region

A complete set of stationary states are constructed to represent the wavefunction:

$$\Psi = \sum_{\lambda} A_\lambda X_\lambda \tag{2.45}$$

where the coefficients A_λ are of the form:

$$A_\lambda = \int_V X_\lambda \Psi dV \tag{2.46}$$

where the integration is over the whole internal volume.
These stationary states satisfy the Hamiltonian $HX_\lambda = E_\lambda X_\lambda$, where E_λ are the energy eigenvalues of the system and X_λ are the eigenvectors. To make sure that these states relate directly to the actual quasi- stationary states at the nuclear surface, we introduce a boundary constant, b, giving the boundary condition (equ. 2.47) which must be satisfied on the nuclear surface at the channel radius a (the solution of the Schrödinger equation have zero derivate at the surface for the energies correspond to the hamiltonian eigenvalues):

$$\frac{dX_\lambda}{dr} + bX_\lambda|_{r=a} = 0 \tag{2.47}$$

and by substitution and integration we obtained:

$$-\frac{\hbar^2}{2m}\left(\Psi\frac{dX_\lambda}{dr} + X_\lambda\frac{d\Psi}{dr}\right)_{r=a} = (E - E_\lambda)\int_0^a X_\lambda \Psi dr \tag{2.48}$$

Using equ. 2.46 and the boundary condition we can write:

$$A_\lambda = -\frac{\hbar^2}{2m}X_\lambda(a)\frac{\Psi'(a) + b\Psi(a)}{E - E_\lambda} \tag{2.49}$$

By plugging this equation into the 2.45, we obtain:

$$\Psi(r) = G(r,a)(\Psi'(a) + b\Psi(a)) \tag{2.50}$$

where G(r,a) is the Greens' function

$$G(r,a) = -\frac{\hbar^2}{2m}\sum_{\lambda}\frac{X_\lambda^2(a)}{E_\lambda - E} \tag{2.51}$$

The R-function is defined as the value of the Green's function at r = a.

$$R = G(a,a) = -\frac{\hbar^2}{2m}\sum_{\lambda}\frac{X_\lambda^2(a)}{E_\lambda - E} \tag{2.52}$$

To simplify the expression, a new parameter is introduced, γ_λ, such that $\gamma_\lambda^2 = \frac{\hbar^2}{2m}|X_\lambda|^2$; then the R-function is written:

$$R = \sum_{\lambda}\frac{\gamma_\lambda^2}{E - E_\lambda} \tag{2.53}$$

Here E is the energy of the particles and E_λ is the energy eigenvalue, associated with an energy level in the compound nucleus.
To calculate the reaction cross-section, we must derive an expression for the channel wavefunction in the external region.

2.5.1.2 External Region

The total wave function in the external region (where only the Coulomb force is present) can be written as the superposition of the incoming (I) and outgoing waves (O):

$$\Phi_l = I_l - e^{2i\delta_l}O_l = I_l - U_l O_l \tag{2.54}$$

where the quantum number l denote the incident orbital angular momentum of the system and $U_l = e^{2i\delta_l}$ is the collision function which connects the incoming and outgoing waves.
The incident and outgoing waves are related to the regular and irregular Coulomb functions Fl and Gl by

$$I_l = (G_l - iF_l)e^{iw_l} \tag{2.55}$$

$$O_l = (G_l + iF_l)e^{-iw_l} \tag{2.56}$$

where w_l is the Coulomb phase shift, $w_l = \sum_{n=1}^{l} tan^{-1}\frac{\eta_l}{n}$, and η_l the same as in equ. 2.17.

Using the equation 2.54 we can construct the nuclear scattering amplitude A as well as the differential cross section dσ :

$$A(\theta) = \frac{1}{2}ik^{-1}\sum_l (2l+1)(1-U_l)P_l(cos\theta) \tag{2.57}$$

$$\frac{d\sigma(\theta)}{d\Omega} = |A(\theta)|^2 = \frac{1}{4}k^{-2}\left|\sum_l (2l+1)(1-U_l)P_l(cos\theta)\right|^2 \tag{2.58}$$

where the Legendre polynomials are introduced.
We can express the collision function U_l in terms of the R-function by utilizing the boundary conditions and equating the logarithmic derivatives of the internal (provided by the R-function) and external wave functions at the nuclear surface (r = a). This allows U_l to be expressed in terms of a phase shift, δ_l, as:

$$U_l = e^{2i\delta_l} \tag{2.59}$$

where

$$\delta_l = tan^{-1}\left(\frac{P_l R_l}{1 - R_l S_l}\right) - \phi_l \tag{2.60}$$

Here ϕ_l, P_l, and S_l are the hard-sphere phase shift, penetrability, and energy shift function, respectively

$$\Phi_l = tan^{-1}\left(\frac{F_l}{G_l}\right) \tag{2.61}$$

$$P_l = \frac{kr}{(F_l^2 + G_l^2)}|_{r=a} \tag{2.62}$$

$$S_l = P_l(F_l F_l' + G_l G_l') \tag{2.63}$$

From this point, we have an expression for the differential cross-section which depends on the collision function which in turn depends on the phase shifts associated with Coulomb scattering (ω_l), hard-sphere scattering (Φ_l), and reaction scattering (R-function). All the information about the stationary states is contained within the R-function, and these states are related to the physical reality by the boundary constant, b.

2.5.1.3 Multi-channel matrix representation

In single channel calculation with zero spin nuclei, R-matrix is one dimensional and it should to be referred to as R-function being a function of energy.
In many cases there are usually multiple states and channels open and multiple combinations of spin that contribute to the formation of states of different spin-parity. The collision function and R-function then become the collision matrix and R-matrix with indices c = $[\alpha s \nu l m]$ which represent the channel, channel spin, channel spin component, orbital angular momentum, and orbital angular momentum component respectively.

In this representation the R-matrix is given by:

$$R_{cc'} = \sum_{\lambda} \frac{\gamma_{\lambda c'} \gamma_{\lambda c}}{E_\lambda - E} \tag{2.64}$$

where the unprimed and primed indices denote values in the entrance and exit channels respectively; and the collision matrix is related to the R-matrix as:

$$U_{cc'} = (k_c r_c)^{\frac{1}{2}} O_c^{-1} (1 - R_{cc'} L_c)^{-1} (1 - R_{cc'} L_c^*) I_{c'} (k_{c'} r_{c'})^{-\frac{1}{2}} \tag{2.65}$$

where $L_c = S_c$ - B_c + iP_c, with B_c being the matrix form of the boundary constant.

This theoretical approach is characterized by energies E_λ and reduced widths γ_λ. The quantities undetermined from the theory, the reduced width amplitudes γ_λ and the energies E_λ, are then varied using a minimization routine to best match the data. Once this is completed, partial widths and level energies can be extracted.
The formula 2.64 can be applied both to resonant or non-resonant case. In the latter case, the non-resonant behavior is simulated by a high energy pole, referred to as the background contribution, which makes the R- matrix nearly independent on the energy [87].
The pole properties used in the formula 2.64 (E_λ, γ_λ) are associated with the physical energy and width of resonances, but not strictly equal. This is known as the difference between "formal" parameters (γ_λ) and "observed" parameters (E^r_λ, γ^o_λ) deduced from the experiment.

2.5.2 Formal and observed parameters

Resonances are characterized by a resonance energy and partial widths associated to the different decay modes. These are the real physical propertie of the compound nuclear configuration and are known as "observed" parameters, deduced from experiment. In contrast, the parameters in the R-Matrix are associated with the physical energy and width of resonances, but not strictly equal, and depend on the channel radius. These parameters are called "formal" or calculated. In the R-Matrix formalism, the final cross-section over a resonance can be described as having an observed experimental width, which is the physical reality of the situation, and is related to the internal eigenstate parameter γ_λ via the channel radius and boundary condition.
In this sense R-Matrix is a phenomenological approach. It describes the observed cross-section in terms of parameters Γ, without giving any information about the real wavefunctions of the compound nucleus.
The γ_λ parameters are named the reduced widths and have units of $\sqrt{E}$. When the single pole approximation is adopted, widths with units of energy are related by [88]:

$$\Gamma_\lambda(E) = 2P(E)\gamma_{\lambda^2} \tag{2.66}$$

this is the formal width of the resonance. The observed width is given by:

$$\Gamma_{\lambda}^{o}(E) = \frac{2P(E)\gamma_{\lambda^2}}{(1 + \gamma_{\lambda}^{2} S'(E)|_{E=E_r})} \tag{2.67}$$

In fact, when the state energy E_λ is such that the boundary condition is equal to the shift function, then the pole energy and resonance energy are equivalent.
The observed widths are the parameters which are important for calculations, and so once a choice of channel radius and boundary condition have been made, and experimental data fitted, steps need to be taken to extract the observed widths and resonance energies from the parameters E_λ and γ_λ.
In general the theoretical apparatus of the R-matrix formalism provide a way for solving the Schrödinger equation but in astrophysics the method is usually considered as tool to fit the experimental cross section and to extrapolate its behavior down to the astrophysical energies. In that case the pair of formal value (E_λ, γ_λ) are considered as adjustable parameters [87].
The R-Matrix provides a complete description of cross-sections of resonant reactions in cases where one or more nuclear states can be formed in the compound nucleus.
One point which R-Matrix theory takes into account which a simple Breit-Wigner resonance does not, is that neighbouring resonances can interfere with each other leading to phase shift modification.

2.6 The problem of the measurement at the astrophysical energies

The direct measurement of the nuclear reaction cross sections at astrophysical energies between charged particles presents many difficulties. These reactions around the Gamow peak that, as we have seen, represents a energy window centered around the keV's values, while the Coulomb barrier between interacting particles of MeV, thus implying that the reaction proceeds through the tunnel effect.
The expected cross section then shows the exponential decrease $\sigma(E) \propto e^{-2\pi\eta}$ and the corresponding value drastically drops to nano or pico barns as the energy approaches to the astrophysical energies.
This means that in realistic experimental conditions, the expected counting rate is prohibitively low. In fact, a low cross section means a low number of detected particles (N_{det}), the so-called signal, on the detector according to the equation:

$$N_{det} \propto \sigma(E) N_{imp} N_{tar} \Delta\Omega \epsilon \tag{2.68}$$

where
N_{imp} is the number of incident particles per second and cm^2;
N_{tar} is the number of target nuclei;
$\Delta\Omega$ is the solid angle covered by detectors;
ϵ is the detection efficiency.

From the definition 2.68, different parameters can be varied in order to increase N_{det}:

- increasing the number N_{imp} of impinging particles. It is related to the beam current whose the increasing intensity could produce:
  - a rapid heating and then a consequent deterioration of the target due to the dissipation of the beam energy inside the target itself,
  - damaging of the detectors, due to the higher elastic scattering counting rate,
  - an increase of the dead time for the electronics used for both acquisition and storage of the experimental data.

- increasing the target tickness N_{tar}, but in this way both energy-loss and angular-straggling will be increased;
- increasing the solid angle $\Delta\Omega$ of the detector. The maximum theoretical solid angle for a detector is 4π steradiants, but it is difficult to perform such kind of design, moreover increasing the number of detectors the electronics and the possibility to disposing the detectors is more complicated.

Even if N_{det} might increase by improving the experimental setup, this number is affected by the background noise events N_{bkg}, physical processes different from that of interest (such as natural decay of unstable isotopes or interaction with cosmic-rays), the electronics involved in the experimental setup.
For a successful experiment it is important to reach the condition:

$$\frac{N_{det}}{N_{bkg}} >> 1 \tag{2.69}$$

This ratio can be adjusted by increasing the detected particles or by reducing the background noise, with the following techniques:

- using of very low-noise electronics;
- performing nuclear astrophysics experiments in underground laboratories, as the Laboratori Nazionali del Gran Sasso.

Even if these problems could be solved, the astrophysical factor cannot be extracted because of the presence of the effects electron screening. In this context, the first simple way to avoid the experimental problems consists in an extrapolation of the cross section down to astrophysical energies. As already said, the S(E) factor is useful for an extrapolation from experimental data measured at higher energies because of its energy dependence. The standard procedure consists in fitting the high energy data using a proper theoretical function (in the simplest approximation, a polynomial). Then this is extrapolated to the astrophysical energies. Anyway for charged-particles induced reactions the electron screening effect starts to become important with decreasing the beam energy and make the extrapolation not very reliable, as discussed in the next section.

2.6.1 The electron screening effect

In the sections 2.3 and 2.4, non resonant and resonant reactions have been explained by assuming that the interaction between the projectile and target nucleus takes place by means of the Coulomb potential between bare nuclei.
Because of the high temperature at which reactions occur in stellar environment, atoms are generally completely ionized.
However, nuclei itself are immersed in a sea of free electrons, which tend to cluster around the nuclei.
The negative charged area surrounding the nuclei shield the nuclear charge reducing the Coulomb repulsion.
In the condition where the kinetic energy k_bT of plasma particles is much higher than the Coulomb repulsion energy between the particles, the electrons tend to form a spherical shell around the ionized nucleus containing enough electrons to neutralize the positive nuclei (but made up of both electrons and other positively charged nuclei) with Debye-Huckel R_{DH} radius of dimension [1]:

$$R_{DH} = \left(\frac{k_b T}{4\pi e^2 \rho N_A \xi} \right)^{\frac{1}{2}} \tag{2.70}$$

where N_A is the Avogadro number and the quantity ξ is a function of the plasma chemical composition and is expressed by the equation:

$$\xi = \sum_i (Z_i^2 + Z_i) \frac{X_i}{A_i} \tag{2.71}$$

where the sum is over all positive ions and X_i and A_i represents the mass fraction and the mass of nuclei i of charge Z_i.
As the density increase, the Debye-Huckel R_{DH} radius decrease and the screening effects increase. Because the presence of plasma screening will reduce the Coulomb barrier between the positively charged nuclei and an enhancement of the cross section and consequently of the reaction rate factor:

$$f_{pl}(E) = \frac{< \sigma v >_s}{< \sigma_v >_b} = e^{\left(\frac{\pi \eta U_{pl}}{kT}\right)} = e^{\left(\frac{Z_1 Z_2 e^2}{kT R_{DH}}\right)} \tag{2.72}$$

being U_{pl} the potential screening in the stellar plasma; this value could be different from that obtained in laboratory and usually is calculated from theoretical models of plasma theory.

In fact, in the experiments performed in laboratory, the target nucleus is in the form of atom or molecule and the projectile is usually in the form of an ion. This implies that the interacting nuclei are surrounded by the electric cloud having the effect to reduce the potential to zero outside the atomic radius R_a ($\approx 10^{-10}$m) (figure 2.6).
Thus the incident nucleus sees no repulsive Coulomb force until it penetrates beyond the atomic radius, therefore in the region $r < R_a$, where the electrostatic potential of the electron cloud can be considered constant with a value:

$$\phi_a = \frac{Z_1 e}{R_a} \tag{2.73}$$

The projectile then, as shown in figure 2.6, for distances greater than the atomic radius is not affected by the effects of Coulomb repulsion and when it penetrates the electron cloud feels a potential energy effective E_{eff} with a height smaller than the height of the Coulomb barrier [1]:

$$E_{eff} = \frac{Z_1 Z_2 e^2}{R_n} - \frac{Z_1 Z_2 e^2}{R_a} \tag{2.74}$$

When the classical turning point R_c for an impinging nucleus is comparable to the nuclear interaction radius R_n, the influence of the attractive electron potential is negligible, the ratio $\frac{R_n}{R_a}$ being of the order 10^{-5}; this is true only at high energies. At lower energies the classical turning point lays close to atomic radius so that the presence of atomic electrons cannot be neglected. As a consequence of the reduction of the repulsive barrier the interaction cross section and the S(E)-factor shows an increase in the low-energy region with respect to the bare nucleus one.

This enhancement of the cross-section or, equivalently, of the S-factor is described by the empirical relation:

$$f_{lab}(E) = \frac{\sigma_s(E)}{\sigma_b(E)} = \frac{E}{E + U_e} e^{(\frac{\pi \eta U_e}{E})} \tag{2.75}$$

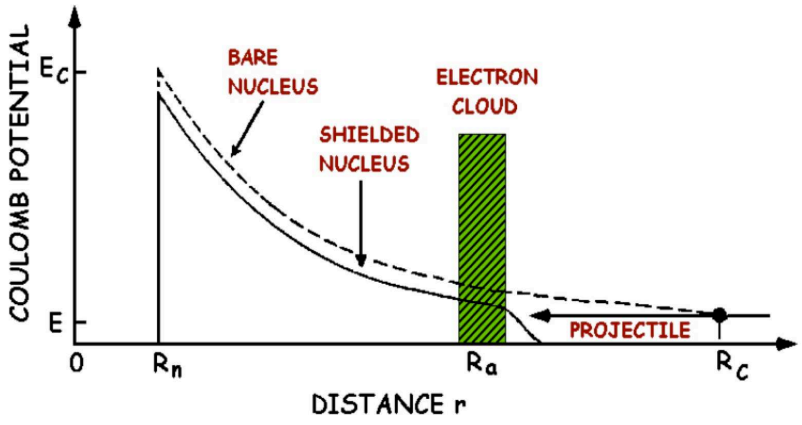

FIGURE 2.6: Schematic representation of the potential between charged particles. The presence of the electron cloud reduces the Coulomb barrier between the interacting nuclei. The electron screening effects cause an enhancement of the S(E)-factor [1].

where σ_s(E) represents the shielded cross section, σ_b(E) the bare ones and U_e represents the screening potential for the studied reaction.

In order to derive the equation 2.75 the relation $E_{eff} = E + U_e$ has been used since the penetration through the screened Coulomb barrier at centre of mass projectile energy E is equivalent to that of bare nuclei at a slightly higher effective energy.

If the ratio $\frac{E}{U_e} > 10^3$ the electron screening effects are negligible so one essentially measures the bare-nucleus cross section $\sigma_b(E)$; while if $\frac{E}{U_e} < 10^2$ these effects are not negligible and they act as an enhancement on the S-factor values [89].

The experimental enhancement has been observed in several fusion reactions and it has been seen that the lower is the interaction energy, the larger is this enhancing factor.

It is necessary to know the electron screening potential in order to extract the bare nucleus cross section. Usually the value of the screening potential U_e is determined theoretically by using different atomic models and experimentally by measuring the cross section at low-energies or by extrapolation.

From the theoretical point of view it's possible to distinguish two opposite case:

- low-velocity case (Adiabatic Approximation). In this case the motion of the nuclei is much slower than the electrons' one. It is possible to determine the

screening potential U_e by

$$U_e = E^1 + E^2 - E^{1+2} \tag{2.76}$$

that is the difference of the binding energy in the entrance channel ($E^1 + E^2$) and the binding energy in the compound system. The adiabatic limit represent the highest theoretical value determinable for a reaction.

- high velocity case (Sudden Approximation). In this model, the electron distribution at fusion time is almost the same as it was in the initial state: therefore the relative velocity between the interacting nuclei is much higher than the electrons' one.

From the experimental point of view usually the screening potential in the region of the Gamow peak comes from extrapolation on the experimental data obtained at much higher energies. In fact, as mentioned above, the direct measurement of the nuclear reaction cross sections at low-energies presents many difficulties.
In this way, the screening potential is extracted using the experimental data for which $\frac{E}{U_e} > 10^3$, where the screening effects are negligible.
Then the experimental data are fitted assuming the extrapolation to be an accurate estimate of the bare-nucleus S(E)-factor and using the unknown U_e as free parameter.
The two result, that is the theoretical upper limit and the experimental ones, show a systematic discrepancy, since in several occasions the experimental U_e has proven larger than the adiabatic limit.
One of the most important uncertainties in the experimental nuclear astrophysics derive from this procedure and, because of this, more exhaustive and precise determinations of σ_b are needed at energies as low as possible.

2.7 Reaction rate involved in fluorine nucleosynthesis

It was discussed in Chapter 1 the mechanism of fluorine nucleosynthesis in various environments. A summary of the reactions involved in the nucleosynthesis process in low-mass AGB stars is as follows. Starting from ^{14}N, a product of the CNO cycle and the abundant ^{4}He nuclei in these environments:

$$^{14}N(\alpha,\gamma)^{18}F(\beta^{+})^{18}O(p,\alpha)^{15}N(\alpha,\gamma)^{19}F \tag{2.77}$$

This nuclear path required protons and neutrons (see chapter 1 for detail).
Within the He-intershell, most of the neutrons released by the ^{13}C(α,n)^{16}O reaction during the inter-pulse period are captured by ^{14}N, via the ^{14}N(n,p)^{14}C reaction and, thus, protons are produced. Then, the ^{14}C(α,γ)^{18}O reaction synthesizes ^{18}O which, in turn, captures the freshly synthesized protons leading to the production of ^{15}N via the ^{18}O(p,α)^{15}N reaction.
This process competes with the main destruction channel of ^{15}N, the ^{15}N(p,α)^{12}C reaction. Later on, at the development of the following TP, ^{15}N captures an α particle producing ^{19}F.
Destruction of ^{19}F could occur by proton, α or neutron capture via:

$$^{19}F(p,\alpha)^{16}O \tag{2.78}$$

$$^{19}F(n,\gamma)^{20}F \tag{2.79}$$

and

$$^{19}F(\alpha,p)^{22}Ne \tag{2.80}$$

A comparison between the rates for the reactions responsible for destruction of fluorine is shown in figure 2.7.
In the temperature range of relevance in the case of extra-mixing phenomena at the bottom of the convective envelope in AGB stars, which are characterized by a maximum temperature of about 10^7 K, the ^{19}F(p,α)^{16}O reaction is the main destruction channel of fluorine and the ^{19}F(α,p)^{22}Ne reaction is only of marginal importance.

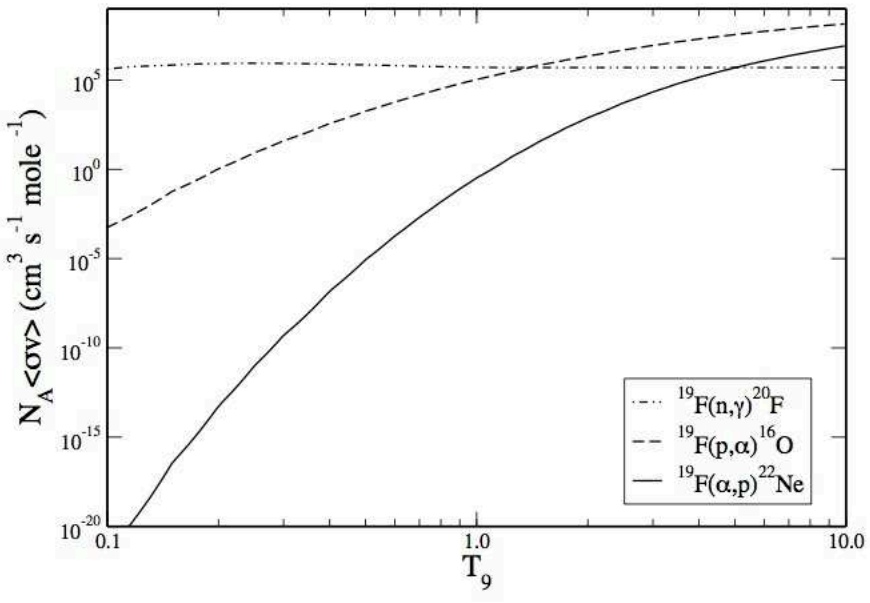

FIGURE 2.7: The reaction rates for the three main mechanisms responsible for destroying fluorine in AGB stars [13].

The problem is that taking into account both the uncertainties related to the partial mixing zone and those related to nuclear reactions, the highest values of ^{19}F enhancements observed in low-mass AGB stars are not matched by the models. This discrepancy requires a revision of the uncertainties in the nuclear reaction rates involved in the synthesis of F in AGB stars and in particular for the ^{19}F(p,α)^{16}O reaction.

As pointed out in the Nuclear Astrophysics Compilation of Reaction Rates (NACRE [15]) and confirmed by Spyrou et al. [14], the ^{19}F(p,α_0)^{16}O channel (^{16}O being left in its ground state following ^{20}Ne decay) is giving the largest contribution to the reaction rate of the ^{19}F(p,α)^{16}O reaction for $0.01 < T_9 < 0.1$.
In fact, the (p,$\alpha\gamma$) branch of the reaction is dominant at high temperatures ($T_9 \geq 0.1$), while the (p,α_0) branch is dominant at low temperatures, as shown in fig. 2.8. So, the contribution of the α_0 channel only is currently regarded as the dominant one at temperatures relevant for AGB stars.

The currently recommended low-energy values of the ^{19}F(p, α_0) astrophysical factor S(E), showing in fig.2.9 are collected in the NACRE [15] and obtained from several works:

- Breuer 1959 ($E_{c.m.}$ = 461- 684 keV, absolute data [22])

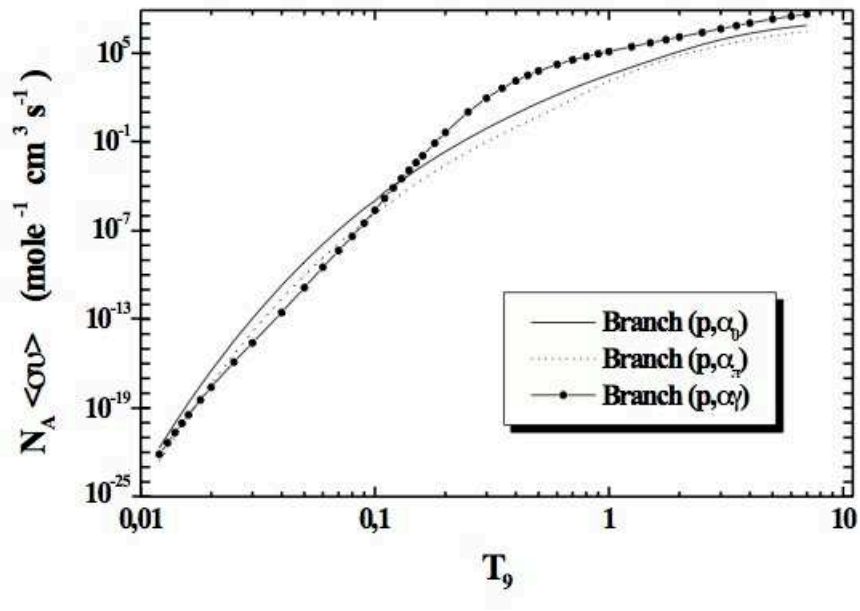

FIGURE 2.8: Reaction rate for the three branches of the ^{19}F(p,α)^{16}O reaction (T_9 in units of 10^9 K) [14].

- Isoya et al 1958 ($E_{c.m.}$ = 598-1385 keV, data normalized by assuming σ = 42 mb at Ecm = 1.3 MeV [25])
- Caracciolo et al 1974($E_{c.m.}$ = 760-817 keV, absolute data [26])
- Cuzzocrea et al 1980($E_{c.m.}$ = 1476-2544 keV, absolute data [90])

The S(E) factor shows several resonances around 1 MeV but no data are available at the energies $E_{c.m.} \lessapprox 300$ keV, where fluorine burning is most effective; the lowest energy direct data reach 461 keV center- of-mass energy (Breuer [22]).

Below $E_{c.m.}$ = 460 keV, only the unpublished data of Lorentz-Wirzba (PhDThesis, 1978) exist. These data extend down to ≈150 keV bombarding energy and support a strong suppression of compound ^{20}Ne decay to the ground state of ^{16}O at Ecm ≈ 0.14-0.6 MeV. However, these results were not included in the NACRE compilation as possible systematic errors affecting the absolute normalization might lead to an underestimate of S(E) by a factor of two [15].

The difficulty arises primarily because this measurement had to be performed inside the energy windows relevant for astrophysics (the Gamow window) that, in a proton rich enviroment, extend from 0.8 down to 0.3 MeV. Anyway these energies are much lower than the coulomb barrier of the ^{19}F+p channel that is

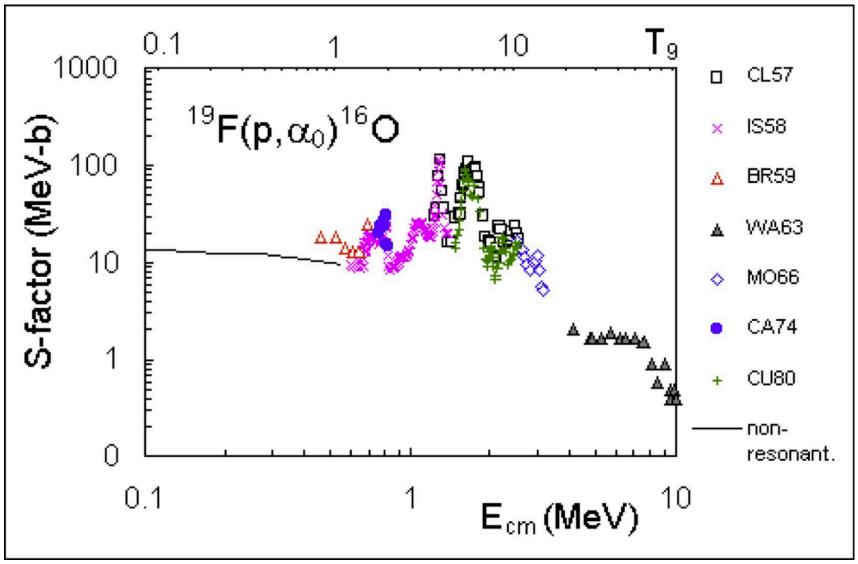

FIGURE 2.9: Astrophysical S(E)-factor for the ^{19}F(p, α_0) reaction from the NACRE compilation [15].

about 2.5 MeV. This makes the cross section measurement of the nuclear processes under investigation very difficult, thus extrapolation is required to estimate the relevant low-energy cross section.

The astrophysical factor was then extrapolated to low energies assuming a dominant contribution of the non-resonant part [15], supported also from the unpublished data.
This conclusion disagrees with older measurements in Breuer that claimed the occurrence of two resonances at around 400 keV.
In any case, the rate for T_9 <0.3 is determined mainly from the non-resonant (p,α_0) channel, causing a progressive increase of the uncertainties up to 50% at the lowest temperatures [15].

Very recently, new data have been provided in the $E_{c.m.} \approx$ 0.6-1 MeV energy interval by Lombardo et al. (2013) [16]. As shown in fig. 2.10, in the energy region around the $E_{c.m.}$>0.7 MeV resonance, the new results agree reasonably well with the data present in literature. On the contrary, in the $E_{c.m.} <$ 0.7 MeV energy range the S(E) factors extracted from direct measurements (Breuer and Isoya) exhibit two different behaviors. The new results are in good agreement with the analogous data extracted from Breuer, being larger by a factor of about 1.4 than the data taken from Isoya. The smooth increase of S(E) in this energy

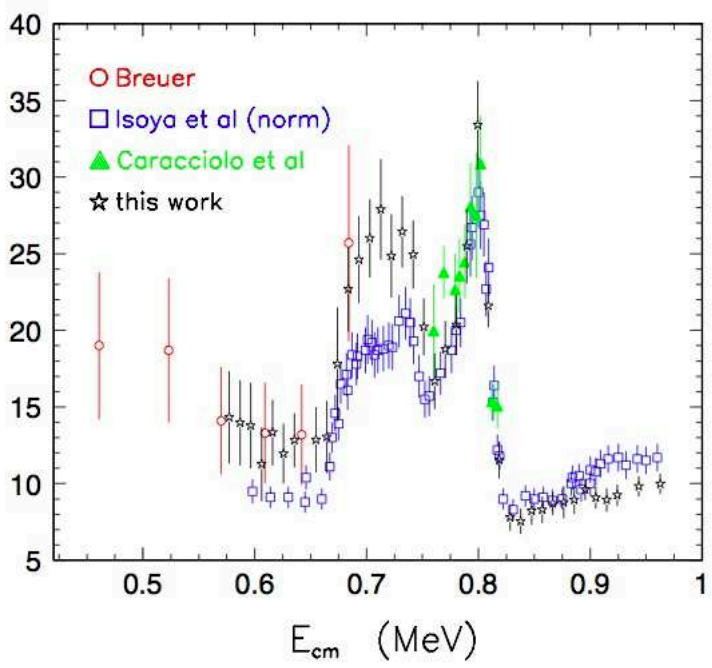

FIGURE 2.10: Astrophysical factor for the ^{19}F(p, α_0) reaction by Lombardo et al. [16].

region suggests the possible existence of two low-lying broad resonances at E_x ≈13.22MeV.

This contradiction and the very simple recommended extrapolation to astrophysical energies have lead to hypothesize a nuclear origin of the discrepancies observed in Galactic fluorine studies.

In the case of extra-mixing phenomena, which are characterized by a maximum temperature of about 10^7 K, the energy region below 500 keV is of key importance, thus requiring further investigation to evaluate the contribution of possible resonances, which could significantly enhance the reaction rate at such low temperatures. New data at a lower incident energy are needed to clarify this question.

Chapter 3

The Trojan Horse Method

As described in the previous chapter, nuclear reaction data play an important role in nuclear physics applications. Cross sections for reactions of neutrons and charged particles taking place at energies from several keV to tens of MeV, are required for nuclear astrophysics and other applications. Unfortunately, for a large number of reactions the relevant data cannot be directly measured in the laboratory or easily determined by calculations. Direct measurements may encounter a variety of difficulties mainly connected to the presence of the Coulomb barrier and the electron screening effect.

In fact, the energy regime relevant for a particular application is often inaccessible, cross sections for charged-particle reactions become vanishingly small as the relative energy of the colliding nuclei decreases. This makes the cross section measurement of the nuclear processes under investigation very difficult and in most cases impossible. For astrophysical purposes, such as descriptions of stellar environments and evolution, reaction rates at energies below 100 keV are needed. Usually this is reached using the extrapolation procedure, made on experimental data obtained at much higher energies, performed under the guidance of nuclear theory, such as the R-matrix technique. But, extrapolation can introduce large errors due to, for istance the presence of subthreshold resonances or the wrong estimate of the electron screening potential.

For these reasons several indirect methods, for example the Coulomb dissociation (CD), the asymptotic normalization coefficient (ANC) method, and the Trojan horse method (THM), have been proposed to overcome the specific difficulties of direct measurements.

3.1 The Indirect Methods

As already mentioned, both the Coulomb barrier penetration and the electron screening effects represent problems that must be overcome in order to get the cross-section for charged-particle induced reactions in the energy domain relevant for astrophysics. In order to overcome these limitations, several innovative indirect methods have been proposed in recent years, all of which rely on a combination of theory and experiment for success. In particular, ANC and CD methods provide information about astrophysical relevant reactions involving photons, while the THM is applied to reactions between charged particles.

3.1.1 Coulomb Dissociation

Among indirect methods, Coulomb dissociation has been used to extract cross sections (or, equivalently, astrophysical S factors) for radiative-capture reactions, a(b,γ)c, by studying the time-reversed breakup reaction in which the Coulomb field of a highly-charged target provides a virtual photon that is absorbed by the projectile. Due to the high flux of virtual photons provided by the target nucleus, the cross section of the breakup, C(c, ab)C, is much larger than the capture cross section and can be related to the latter via the principle of detailed balance [28].

Coulomb dissociation is a simple and powerful reaction mechanism. Since the electromagnetic interaction is well known, valuable nuclear structure and reaction information can be obtained from experiments in which nuclear effects are excluded.
The suppression of nuclear effects can be accomplished by selecting bombarding energies below the Coulomb barrier or, if higher energies are desired, by observing the breakup products at small forward scattering angles which (classically) correspond to large impact parameters.

It was used, for example, in the $^{12}C(\alpha,\gamma)^{16}O$ reaction [91], key reaction in the synthesis of heavy elements in massive stars, after ^{4}He burning, or in $^7Be(p,\gamma)^8Be$ [91, 92], that has great importance in the solar-neutrino problem.

In detail, the idea of the method is to derive the cross section of the reaction:

$$a + b \rightarrow c + \gamma \tag{3.1}$$

from the cross section of the inverse photo disintegration reaction:

$$c + \gamma \rightarrow a + b \tag{3.2}$$

where the breakup is induced by the intense Coulomb field of a high-Z target nucleus. Thus, the reaction effectively studied is the three-body reaction:

$$c + C \rightarrow a + b + C \tag{3.3}$$

where the nucleus C is the source of virtual photons and is unchanged at the end of the breakup process.
From the indirect experiment it is possible to extract the photo dissociation cross section:

$$\sigma^{photo}_{E_\lambda}(c + \gamma \rightarrow a + b) \tag{3.4}$$

and to convert it to a radiative capture cross section employing the theorem of detailed balance.

$$\sigma(a + b \rightarrow c + \gamma) = \frac{(2j_c + 1)2}{(2j_a + 1)(2j_b + 1)} \frac{k_\gamma^2}{k^2} \sigma(c + \gamma \rightarrow a + b) \tag{3.5}$$

where, the wave number k in the (a+b) channel is:

$$k = \sqrt{\frac{2\mu_{ab} E_{c.m.}}{\hbar^2}} \tag{3.6}$$

and the photon wave number is given in terms of the Q-value of the capture reaction:

$$k_\gamma = \frac{E_\gamma}{\hbar c} = \frac{E_{c.m.} + Q}{\hbar c} \tag{3.7}$$

Usually k$\gamma \ll$ k so that the phase space favors the photodisintegration cross section as compared to the radiative capture.

CD method, experimentally, offers two advantages:

- selecting the adequate kinematical conditions allows more precisely measurements at astrophysical energies, using beams at energies above the Coulomb barrier. In this way, thanks to the larger cross section and the possibility of using thicker targets, because of the high energies involved, the reaction yield is much higher than one could get in a direct measurement [28];
- the large number of virtual photons seen by the passing projectile leads to an enhancement of the cross section.

Rate enhancement is evident considering the break-up differential cross-section referred to the projectile in a certain multipole order $\pi\lambda$ [28]:

$$\frac{d^2\sigma}{d\Omega dE_\gamma} = \frac{1}{E_\gamma}\frac{dn_{\pi\lambda}}{d\Omega}\sigma_{\pi\lambda}^{photo} \tag{3.8}$$

This equation presents three terms:

- a kinematical factor $\frac{1}{E_\gamma}$
- the number of virtual photons in respect of the solid angle $\frac{dn_{\pi\lambda}}{d\Omega}$
- the photo-disintegration cross section $\sigma_{\pi\lambda}^{photo}$

The second term, called equivalent photon spectrum, is responsible of the increasing reaction rate (even of some order of magnitude), in comparison with the radioactive capture [28]. This equation is valid only as an approximation, since the process we are trying to study is on-energy-shell, and involves a real photon [28], an can be used only if the process is solely given the Coulomb interaction, therefore the reaction has to be peripheral. Otherwise it is necessary to take into account strong-interaction effects.

3.1.1.1 Experimental Applications

The CD method proves to be useful in studying radioactive capture phenomena, because it allows us to select the relative low-energy region between the two fragments (near-parallel emission).
Is it also necessary to underline the the break-up process can occur by means of electro-magnetic field or by strong-interaction. These two process cannot be discerned and give rise to interference phenomena.
As an example of this the reaction $^{7}Be(p,\gamma)^{8}B$ can be taken in account: this reaction, studied through $^{208}Pb(^{8}B, p^{7}Be)^{208}Pb$ [91, 92] shows the clear presence of interference in the cross-section between the two reaction mechanisms.
The CD method can be used, in this case, because ^{8}B has a weak binding energy (0.1375 MeV), and the dissociation cross-section is three orders of magnitude bigger than the nuclear effects [91, 92].

3.1.2 Asymptotic Normalization Coefficient

The second indirect technique presented is the so-called ANC (Asymptotic Normalization Coefficient) method [93], which provides the normalization coefficients of the tails of the overlap functions, and determines S factors for direct capture reactions at astrophysical energies. The ANC technique is based on the fact that direct proton-capture reactions of astrophysical interest often involve systems where the binding energy of the captured particle is low. Hence, at stellar energy the capture proceeds through the tail of the nuclear overlap function. The shape of the tail of the overlap function is completely determined by the Coulomb interaction and its amplitude fixes the rate of the capture reaction.

The starting point of this method is to obtain the normalization coefficient C of the bound system B=A+p or B=A+α, so in case of a nucleus formed by a core (A) and a proton or a alpha particle [94]. This coefficient will tell us the probability to find a nucleus B in A+p or A+α configuration, at distances far bigger than the strong-interaction range, the wave function behavior determined essentially by the Coulomb interaction. In this way is possible to calculate the reaction rate in a accurate way, analyzing the tail of the wave function [95]. Let us consider a

peripheral transfer process:

$$A + X \rightarrow B + Y \tag{3.9}$$

in which X=Y+a and B=A+a, and where a is the transfer particle. In distorted wave born approximation (DWBA), calling M the process amplitude, and the particle-particle interaction is peripheral, this amplitude will be [96]:

$$M(E, cos\theta) = \sum M_a \left(\chi_f^{(-)} I_{Aa}^B(\vec{r}_{Aa}) |\Delta V| I_{Ya}^X(\vec{r}_{Ya}) \chi_i^{(+)} \right) \tag{3.10}$$

with: E_i relative kinetic energy between A and X, θ diffusion angle in the C.M. system, $\chi_i^{(+)}$ and $\chi_f^{(-)}$ distorted waves in the entrance and exit channels respectively, ΔV transition operator and $I_{\beta\gamma}^{\alpha}(\vec{r}_{\beta\gamma})$ function of the two nuclei β and γ, that forms the bound state $\alpha = \beta + \gamma$. In this method the overlap function referred to the transfer process must be the same that appears in the direct radiative capture amplitude:

$$M_{DC} = \lambda \left(I_{Aa}^B(\vec{r}_{Aa}) |O| \Psi_i^{(+)}(\vec{r}_{Aa}) \right) \tag{3.11}$$

in which λ is a kinematic factor, O is the electromagnetic transition operator and Ψ_i^+ represents the scattering wave function in the entrance channel. If the diagram in fig. 3.1 describes the transfer reaction, the DWBA cross-section can be written in terms of spectroscopic factors of the incoming and outcoming nuclei [96]:

$$\frac{d\sigma}{d\Omega} = \sum_{j_B j_x} S_{A_a l_B j_B} S_{Y_a l_x j_x} \sigma^{DW}_{l_B j_B l_x j_x} \tag{3.12}$$

Spectroscopic factors, if calculated using approximation, are strongly dependent because the behavior of the wave function inside the nucleus is strongly influenced by them. On the other hand, the asymptotic normalization coefficient is tied to the behavior of the wave function at distances bigger than the nuclear radius. This makes the coefficient less dependent from the model than spectroscopical factor [96].

The extraction of the ANC follows a procedure analogous to the one adopted in evaluating the spectroscopic factors from transfer reactions (by normalizing the

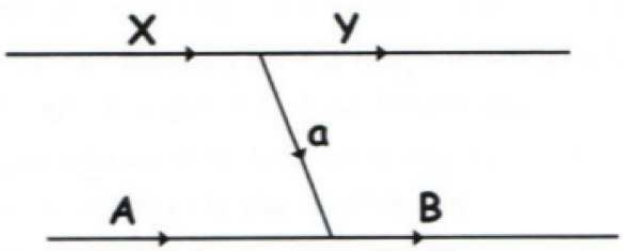

FIGURE 3.1: Schematic view of the transfer reaction mechanism A+X → B+Y, where X = Y ⊕ a and B = A ⊕ a, preceeding through the transfer of particle a from X to the nucleus A.

DWBA cross section to the experimental one). If is adopted the equation

$$I_{\beta_\lambda l_\alpha j_\alpha} = S_{\beta_\gamma l_\alpha} j_\alpha^{\frac{1}{2}} b_{\beta_\gamma l_\alpha l_\alpha} \tag{3.13}$$

as the radial part of the overlap wave function, in which $b_{\beta_\lambda j_\alpha j_\alpha}$ is a normalization constant, multiplied by the wave function of the relative motion between the two clusters β and γ. The transfer cross section is therefore paramiterized in terms of the spectroscopic factor for the X = Y ⊕ a and B = A ⊕ a bound system:

$$\frac{d\sigma}{d\Omega} = \sum_{l-Bj_Bj_xl_x} (S_{A_a l_B j_B})(S_{Y_a l_x j_x}) \sigma^{DW}_{l_B j_B l_x j_x} \tag{3.14}$$

A modified DWBA cross section can be introduced in which a more suitable normalization for pheripheral process is adopted in terms of the ANC's for the B and X bound states:

$$\frac{d\sigma}{d\Omega} = \sum_{j_Bj_xl_Bl_x} (C^B_{A_a l_B j_B})^2 (C_{Y_a l_x j_x})^2 R_{l_B j_B l_x j_x} \tag{3.15}$$

where $\mathrm{R}_{l_B j_B l_x j_x}$ is

$$R_{l_B j_B l_x j_x} = \frac{\sigma_{l_B j_B l_x j_x}}{b_{A_a l_B j_B} b^2_{Y_a l_x j_x}}^2 \tag{3.16}$$

and

$$C_{\beta_\lambda l_\alpha j_\alpha} = S_{\beta_\gamma l_\alpha j_\alpha^{\frac{1}{2}}} b_{\beta_\gamma l_\alpha l_\alpha} \tag{3.17}$$

is the ANC of the overlap function. in this equation $S_{\beta_\gamma l_\alpha j_\alpha^{\frac{1}{2}}}$ is the spectroscopic factor.

Since the ANC is much less affected by the uncertainties on the nuclear potential with respect to spectroscopic factors, the astrophysical factor extracted through this procedure constitutes a very accurate, largely model independent estimate.
To applicate the ANC method, it is necessary to experimentally isolate the transfer contribution. To do this the differential cross-section, calculated using DWBA formalism, has to be normalized to experimental data at little angles, in which transfer reaction is expected to dominate.

The method can be applied for the analysis of direct radiative capture processes, where the binding energy of the captured charged particle is low. Moreover, the ANC technique turns out to be very productive for the analysis of the astrophysical process in presence of a sub-threshold state [29]. Recently, a work by Johnson et al. (2006) [97] developed ANC techniques in order to determine the astrophysical factor also for reactions different from radiative capture processes.

3.1.2.1 Experimental Applications

ANC method can be used, for example, in the study of the ^{8}Be $\rightarrow$ ^{7}Be+p using ^{10}B(^{7}Be,^{8}B)^{9}Be reaction, and then calculate the S(E)-factor for the capture reaction ^{7}Be(p,γ)^{8}B, determining for first the asymptotic normalization coefficient in the virtual decay ^{10}B $\rightarrow$ ^{9}Be+p. Using the ANC determined from the proton exchange reaction ^{9}B(^{10}B,^{9}B)^{10}B, the component of the astrophysical factor at low energy for the ^{10}B $\rightarrow$ ^{9}Be+p reaction was obtained. Using this method $S_{17}(0)$=17.3+1.8 eV b was obtained [95]. This value is in accordance with the one adopted in literature (19^{+4}_{-2} eV b) [98]. This value is also similar to what is obtained using CD method [99], and with direct measurements [100].

3.2 Quasi-free break-up and sequential mechanism

In the study of nuclear reactions , it is possible to distinguish between two extremes: direct reactions and compound nucleus formation [86]. The compound nucleus provides the formation of an excited state of an intermediate nucleus after the collision between the interacting nuclei. In this case, the nuclear reaction take place in two stage (see fig. 3.2):

- the incident low energy particle strikes the target nucleus and combines with it to form a new nucleus, known as compound nucleus. The atomic number and mass number of the compound nucleus are the sum of the atomic numbers and mass numbers of incident particle and the target nucleus;
- the compound (excited) nucleus decays into the final products.

Since the lifetime of compound nucleus (10^{-14} s) is much greater than the time taken by the incident particle to traverse the nucleus (10^{-22} s), it can be assumed that the mode of decay of the compound nucleus is independent of the mode of its formation.

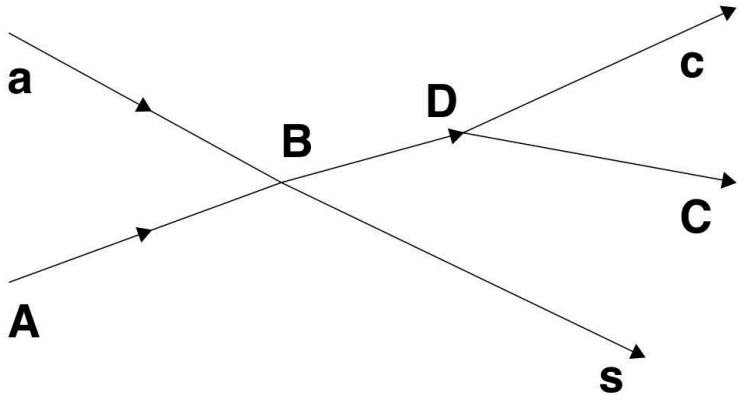

FIGURE 3.2: Sequential decay mechanism proceeding through compound nucleus formation, B.

In the case of direct processes, the interacting nuclei do not form any intermediate state; because these reactions occur quickly and proceed directly from initial to final states they are called direct reactions. Example for such interaction are

the inelastic scattering, the stripping and the knockout reactions [86]. All these reactions have one common thing, the time of interaction (of the order of 10^{-22} s) is much shorter than the life time (10^{-14} s) of compound nucleus. If a nucleus A can be thought constituted by an aggregation of nucleons, called clusters, following an interaction can be separated into its constituent, giving rise to a process of break-up. This process is direct reaction.

In particular, the so-called quasi-free (QF) processes characterized by the presence of a spectator in the exit channel, therefore only a fraction of the target or of the projectile is involved in the reaction while the other counterpart does not participate to the reaction.

In particular, let us consider the nucleus A having a strong probability to be described as a cluster structure A = x $\oplus$ s. The overall reaction is:

$$a + A \rightarrow s + c + C \tag{3.18}$$

As sketched in figure 3.3, the interaction between a and A can cause the break-up of the latter one in its clusters, with s having in the exit channel the same momentum it had before the interaction. This means that s can be considered unaffected by the interaction, representing then the spectator to the virtual interaction:

$$a + x \rightarrow c + C \tag{3.19}$$

Contrary to the sequential mechanism, QF are direct processes.

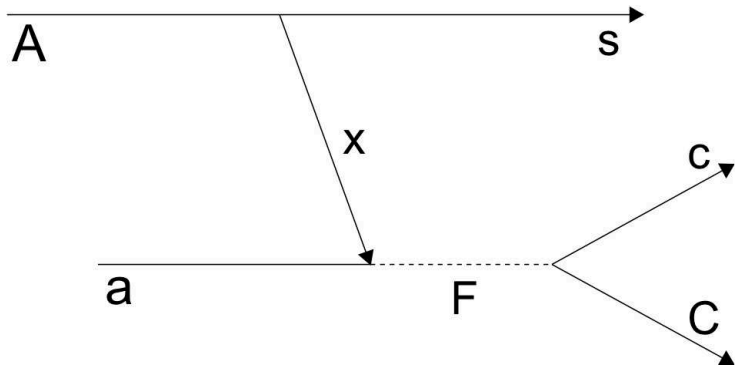

FIGURE 3.3: Schematic view of a quasi-free three-body reaction.

Since the THM is based on the selection of the QF coincidence yield it is necessary to discriminate this process from other possible mechanisms that may occur between the target and projectile, giving the same particles in the final state, such as sequential mechanism (SM). In such sense the SM represent a noise that one has to eliminate during the off-line analysis. Since in the QF-process the exit channel is characterized by the presence of a spectator nucleus, it will possible to fix both kinematic and energetic conditions at which the QF is dominant and well separable from other mechanisms.

3.3 The Trojan Horse Method

In the section 3.1.1 and 3.1.2 two indirect methods, developed to study radiative capture reactions such as (p, γ) or (α, γ) processes, were briefly discussed. But, in nuclear astrophysics there are a large number of reactions with charged particles or neutrons in the exit channel.
THM has been introduced as a tool for extracting low-energy cross section for nuclear reactions having charged particles or neutrons in the exit channel [30, 112]. In fact, it is an experimental indirect technique which selects the QF contribution of an appropriate three-body reaction performed at energies well above the coulomb barrier, to extract a charged-particle two-body cross section at astrophysical energies free from coulomb suppression.

Trojan Horse approach, as suggested by Baur [101], is based on the theory of the quasi-free break-up mechanism in which the interaction between two nuclei produces the break of one particle in its constituting nuclei.

A reaction A+a $\rightarrow$ C+c+s, with nucleus a having a strong x$\oplus$s cluster structure and with three particles in the final states, can proceed by various reaction mechanism.
In the application of the THM we are interested in the process where the Trojan horse nucleus a breaks up into a cluster x that is the transferred particle and where the nucleus s can be regarded as a spectator to the two-body subreaction A+x $\rightarrow$ C+c.
If the QF conditions are fulfilled, the cluster s maintains the same momentum it had in the nucleus a before interacting. As sketched in fig.3.3 the particle x is

conducted inside the nuclear field of A, where the reaction takes place, from a, which for this reason is named Trojan horse nucleus, while the nucleus s does not participate to the reaction and it can be considered as a spectator for the x(a, c)C reaction.

If the energy of the incoming nucleus is chosen high enough to overcome the Coulomb barrier in the entrance channel of the three-body reaction, the decay will occurs in the nuclear field and both Coulomb barrier penetration and electron screening effects are negligible. In the original paper [101] it was proposed that the initial velocity v_a of the projectile a is compensated for by the velocity v_F of the intercluster motion of particle x inside the Trojan Horse nucleus a. In this framework, a momentum of hundreds of MeV/c is required. In the case of TH nuclei having the momentum distribution peaked around 0 MeV/c (e.g. deuteron), such momenta populate the tail of the momentum distribution, making the separation from eventual background mechanisms very difficult.

In order to overcome these problems, a different approach based on the idea that the initial projectile velocity is compensated for by the $x - s$ binding energy was introduced [30, 102, 103]. Thus the two-body $A - x$ reaction can take place at astrophysical energies. Moreover, the role of the cutoff in the momentum distribution, which is related to the Fermi motion of s inside the Trojan Horse nucleus a, consist in fixing the range of energies around the QF energy accessible in the astrophysical relevant reaction, as given by:

$$\Delta E_{qf} = E_{Ax} - B_{xs} \pm E_{xs} \tag{3.20}$$

where E_{Ax} is the beam energy in the center of mass of the $A - x$ system, B_{xs} represent the $x + s$ binding energy and E_{xs} correspond to the energy of their inter-cluster motion within the chosen cutoff in the momentum [104].

A great advantage of the method is the possibility of extracting a full excitation function, e.g from zero energy up to the Coulomb barrier region, by means of a single beam energy.

The QF break-up mechanism can be described by different theoretical formalisms, such as the Distorted Wave Impulse Approximation (DWIA) [105, 106], the Distorted Wave Born Approximation (DWBA) [107] and the Plane Wave Impulse Approximation [108, 109].

3.4 Plane Wave Impulse Approximation

Let us consider as a typical case a simple particle (e.g. a nucleon) colliding with a complex system (a deuteron or light nucleus) having a cluster structure $a = x \oplus s$. This approximation is based essentially on the following three assumptions:

- the projectile A does not interact strongly with two constituents of the system (x and s) at the same time. Equivalently, the average distance between the two constituent of the system is larger than the range of interaction with the projectile;
- The amplitude of the incident wave falling on each constituent is nearly the same as if that constituent alone.The interaction between the projectile a with x is the same as x was free; the presence of s does not influence the interaction;
- the binding energy of the clusters x and s inside A is supposed to be negligible compared to the energy of the incident projectile.

Under these hypotheses and assuming that the incident and outgoing particles can be described by plane waves without any distorting effects due to the Coulomb interaction between particles the cross section for the three-body reaction takes a very simple form [108]:

$$\frac{d^3\sigma}{dE_c d\Omega_c d\Omega_C} \propto KF|\Phi(\vec{p_s})|^2 \left(\frac{d\sigma_{ax}}{d\Omega}\right)^{HOES} \tag{3.21}$$

where:

- KF is a kinematical factor containing the final state phase-space factor and is derived by assuming that the momentum of the spectator to the virtual two-body reaction is equal to the one before the reaction:

$$KF = \frac{k_c k_C^2 E_s E_{c.m.}^2}{k_a E_x \{k_c E_s + E_c[k_c - k_a cos\theta_C + k_C cos(\theta_C - \theta_c)]\}} \tag{3.22}$$

  k_i and E_i are the radial wave number and the energy of i-th particle and θ_i the respective emission angle.

- $|\Phi(\vec{p_s})|^2$ is the Fourier transform of the radial wave function $\chi(\vec{r})$ for the $x - s$ intercluster motion, usually described in terms of Hankel, Eckart and Hulthen functions depending on the $x - s$ system properties:

$$\Phi(\vec{p_s}) = (2\pi)^{-\frac{3}{2}} \int_{-\infty}^{+\infty} \Psi(\vec{r}) e^{(-i\vec{K_s}\vec{r})d\vec{r}} \tag{3.23}$$

- $\frac{d\sigma_{ax}^{HOES}}{d\Omega}$ is the half-off-energy-shell (HOES) differential cross section for the two body reaction A(x,c)C at the center of mass energy $E_{c.m.}$ given in post-collision prescription by:

$$E_{c.m.} = E_{cC} - Q_{2body} \tag{3.24}$$

  where Q_{2b} is the Q-value of the binary reaction A+x $\rightarrow$ C+c and E_{cC} is the relative energy of the outgoing particles c and C.

The deduced total two-body cross section $\frac{d\sigma_{ax}^{HOES}}{d\Omega}$ appearing in equation 3.21 consists of the nuclear part only. The superscript HOES is due to the virtuality of the transferred particle x, because in the entry channel it is not a free particle being bound inside a.
Indeed a is a stable nucleus so it cannot spontaneously decay to the $x + s$ channel, that is satisfying the energy conservation principle. It means that the relation between the energy and momentum for the nucleus x is not valid:

$$E_x \neq \frac{p_x^2}{2m_x} \tag{3.25}$$

However, in the QF approximation the off-energy-shell are neglected and the $\frac{d\sigma_{ax}^{HOES}}{d\Omega}$ is replaced by a suitable two-body-on-shell cross section (OES).

Since the two-body interaction occurs without the effects of penetration through the Coulomb barrier, it is necessary to introduce an appropriate penetration function P_l in order to account for these effects affecting the direct data below the Coulomb barrier

Thus, the HOES cross-section is converted to the relevant OES cross section by taking the linear combination:

$$\frac{d\sigma}{d\Omega} = \sum_l P_l \frac{d\sigma_l^{HOES}}{d\Omega} \tag{3.26}$$

being P_l the penetrability for the l-th partial wave and $\frac{d\sigma_l^{HOES}}{d\Omega}$ the corresponding cross section [30]. In this way, if the momentum distribution is known from independent measurements or calculations and evaluating KF taking into account the experimental and kinematical conditions, it is then possible to derive $\frac{d\sigma_l^{HOES}}{d\Omega}$ from a measurement of the three-body differential cross-section by using equation 3.21 and finally it is possible to extract the two-body cross section after inserting the appropriate penetration function.

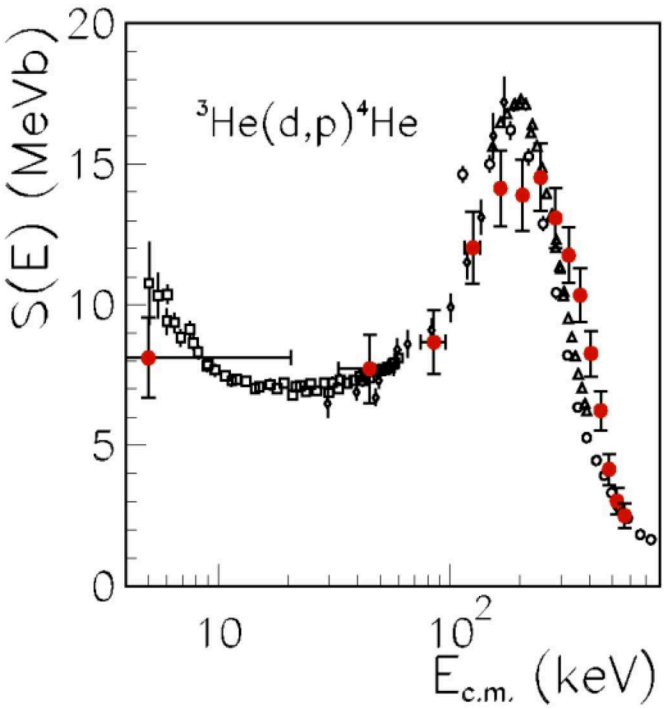

FIGURE 3.4: The TH S(E)-factor (red circles) compared with direct data (open symbols) [17].

Using the cross section derived in equ.3.26, we obtain the astrophysical $S_b(E)$-factor:

$$S_b(E) = E\sigma(E)e^{-(2\pi\eta)} \tag{3.27}$$

which can be compared with the one obtained from direct measurement in order to determine the correction f_{lab} for the reaction and therefore calculate S_{pl}.

The ^{3}He(d,p)^{4}He represents one of the most important examples of the enhancement of the low-energy cross-section caused by the electron screening. Reaction presents a strong increase in the low-energy cross-section, more than what is expected.
Indirect measurements shown in fig. 3.4, obtained through THM method, presents a good agreement with previous works, showing that electron screening has a great effect in enhancing the S(E)-factor in comparison with bare-nuclei case.

3.5 Distorted Wave Impulse Approximation and Modified Plane Wave Born Approximation

In addition to the PWIA approach, the QF-reaction can be described by the Distorted Wave Impulse Approximation treatment. This theoretical formalism allows one to obtain spectroscopic information related to the intercluster wave function $\chi(\vec{r})$. In the DWIA the radial wave functions are deduced from optical-model potentials so that $|\Phi(\vec{p}_s)|^2$, in equation 3.21, turns out to be dependent on the considered reaction as well as on the energy. The main differences between the momentum distributions calculated in PWIA and in DWIA are [108, 110]:

- The tails of the $x - s$ momentum distribution. For recoil momenta, $p_s < 40$ MeV/c, the essential features of $|\Phi(\vec{p}_s)|^2$ are the same in both procedures. However, while the PWIA introduces unphysical zeros in the momentum distribution, they are properly filled in a DWIA treatment.
- The absolute value of the cross section. Indeed, in the DWIA treatment the absolute value of the momentum distribution undergoes a dramatic decrease

due to wave absorption effects, which are not taken into account in PWIA. The reduction factor ranges from a few units to several orders of magnitudes.

In particular, because of the various approximations involved in the THM and of the assumption that off-energy-shell effects are negligible, it is not possible to obtain absolute values of the two-body cross section, as expressed from the relation 3.21.

However this values can be obtained through normalization procedure of the indirect data, usually extracted in the region of low p_s (usually $p_s \leq 40$MeV/c), to the direct data available at energies above the Coulomb barrier. Thanks to this, selecting the region of low spectator momentum, where PWIA and DWIA wave functions have very similar shapes [105], the astrophysical S(E)-factor can be deduced by the relation [30, 102]:

$$S(E) = E \sum_l P_l \sigma_l^{HOES} e^{(2\pi\eta)} \tag{3.28}$$

Thus, the TH method is a complementary tool to direct measurements for the investigation of the charged particle induced reactions of interest for astrophysics.

When the projectile energy is not very high and off-energy-shell effects are not negligible, a more sophisticated approach based on a Modified Plane Wave Born Approximation (MPWBA) [107, 111] turns out to be useful since Coulomb effect and off-energy-shell distortions in the two-body entrance channel are fully included in it [17].

The main aim of the MPWBA is to deduce, in the same way as the PWIA, a connection between the three-body cross reaction and the astrophysically relevant two-body cross section, from the exact T-matrix element and by applying both the DWBA and the surface approximation [107, 111]

In this approach, the differential three-body cross section takes the form:

$$\frac{d^3\sigma}{dE_c d\Omega_c d\Omega_C} = KF|T_{fi}|^2 \tag{3.29}$$

where the T-matrix element T_{fi} contains all the essential information relevant to the scattering process and it has the form:

$$T_{fi} = \langle e^{(i\vec{k}_{Bs}\vec{r}_{Bs})}\phi_B\phi_s|V_{Bs}|\Psi^{(+)}_{Aa}(\vec{k}_{Aa},\vec{r}_{Aa})\rangle \tag{3.30}$$

where B stands for the $c+C$ system, $\Psi^{(+)}_{Aa}(\vec{k}_{Aa},\vec{r}_{Aa})$ is the exact scattering wave function in the initial state, ϕ_B and ϕ_s the wave function for the B and s system. In the distorted wave born approximation (DWBA) it becomes:

$$T_{fi} = \langle \chi^{(-)}_{Bs}\Psi^{(-)}_{Cc}\phi_s|V_{xs}|\chi^{(+)}_{Aa}\phi_A\phi_a\rangle \tag{3.31}$$

ϕ_A, ϕ_a and ϕ_s being the internal wave function of nuclei A, a and s respectively; $\Psi^{(-)}_{Cc}$ the full scattering wave function for the $c+C$ system; $\chi^{(-)}_{Bs}$ and $\chi^{(+)}_{Aa}$ the distorted waves which describe the relative motion in the initial and final channel and V_{xs} the interaction potential between the transferred particle x and the spectator s.

At this point, introducing the surface approximation [107] it is possible to establish a connection between T_{fi} of the three-body reaction and the S-matrix elements of the two-body reaction.
Using this approximation, only peripheral reactions are supposed to contribute significantly to the matrix element, while absorption at smaller distances between the colliding nuclei is assumed very strong [112].
Under these hypotheses, the QF three body cross section can be expressed as [111]:

$$\frac{d^3\sigma}{dE_c d\Omega_c d\Omega_C} = KF|W(\vec{Q}_{Bs})|^2\frac{16\pi^2}{(k_{Ax}\vec{Q}_{Aa})^2}\frac{d\sigma^{TH}}{d\Omega_{Ax}} \tag{3.32}$$

where the momenta $\vec{Q}_{Aa}$ and $\vec{Q}_{Bs}$ are defined as:

$$\vec{Q}_{Aa} = \vec{k}_{Aa} - \frac{m_A}{m_A+m_x}\vec{k}_{Bs} \tag{3.33}$$

$$\vec{Q}_{Bs} = \vec{k}_{Bs} - \frac{m_s}{m_s+m_x}\vec{k}_{Aa} \tag{3.34}$$

The momentum distribution $W(\vec{Q}_{Bs})$ is connected to the wave function of a in momentum space. By taking the Fourier transform of the Schrodinger equation for the $a = x \oplus s$ bound system, it can be shown that [107, 111]:

$$W(\vec{Q}_{Bs}) = -\left(\epsilon_a + \frac{\hbar^2 Q_{Bs}^2}{2\mu_{xs}}\right)\Phi_a(\vec{Q}_{Bs}) \tag{3.35}$$

The momentum $\hbar\vec{Q}_{Bs}$ is the relative momentum of the spectator and the transferred particles. If the intercluster motion is neglected, -$\vec{Q}_{Bs}$ represents the momentum transfer to the spectator nucleus s, thus in QF conditions describes the momentum of s inside a and -$\vec{Q}_{Aa}$ the momentum transfer to A by the cluster x. The THM cross section is:

$$\frac{d\sigma^{TH}}{d\Omega}(Cc \to Ax) = \frac{1}{4k_{Cc}^2}|\sum_l (2l+1)P_l(\widehat{Q}_{Aa}\widehat{k}_{Cc})[S_l J_l^{(+)} - \delta_{(Ax)(Cc)}J_l^{(-)}]|^2 \tag{3.36}$$

with the total (nuclear + Coulomb) S-matrix elements S_l completely describing the reaction C+c $\to$ A+x, where $\delta_{(Ax)(Cc)}$ is the Kronecker symbol. It has the form of a usual two body cross section except for the function $J^{(\pm)}$ which are a consequence of the half-off-energy-shell nature of the two-body process. They can be well approximated by:

$$J^{(\pm)} = D_l k_{ax} Q_{Aa} R^2 e^{\mp i\sigma l}[G_l(k_{ax}R) \pm iF_l(k_{ax}R)] \tag{3.37}$$

where D_l is a constant, F_l and G_l are the regular and irregular Coulomb functions, σ_l is the Coulomb phase shift in partial wave l and R is cut-off radius originating from the surface approximation.

The argument of the Legendre polynomial P_l is the cosine of the center-of-mass scattering angle for the two-body reaction. The analysis is simplified if the reaction of astrophysical interest is a nonelastic two body process with different initial and final channels. Then, assuming that only one partial wave l contributes to the total cross section, we obtain:

$$\frac{d^3\sigma}{dE_c d\Omega_c d\Omega_C} = KF|W(\vec{Q}_{Bs})|^2 \frac{v_{Cc}}{v_{Ax}} P_l^{-1} C_l \frac{d\sigma_l}{d\Omega_{Ax}}(Cc \to Ax) \tag{3.38}$$

with the on-shell two-body cross section $\frac{d\sigma_l}{d\Omega_{Ax}}$ for the reaction C+c $\rightarrow$ A+x in partial wave l and a constant C_l. Here, G_l represents the Coulomb penetrability factor given by:

$$P_l(k_{Ax}R) = \frac{1}{G_l^2(k_{Ax}R) + F_l^2(k_{Ax}R)} \tag{3.39}$$

which compensates for the strong suppression in the two-body cross section at small energies due to the Coulomb repulsion. Because of the presence of the factor C_l and the surface approximation, as said before, the two body cross section can only be obtained with an arbitrary normalization. Absolute cross sections can be obtained only after normalization to the directly-measured excitation function.

3.6 Validity Test

In fig.3.5 and fig.3.6, two results of THM applications at astrophysical energies are shown. In the first is reported a comparison between ^{7}Li(p,α)^{4}He (connected with the lithium-depletion problem) measured using THM, through d(^{7}Li,$\alpha\alpha$)n reaction at 20MeV beam energy [18], and S(E)-factor from direct measurements [113].
In this study the deuteron was used like TH-nucleus and the neutron acted as spectator of the virtual two-body reaction. The agreement between the two direct (open circles) and indirect (full circles) set of data was a first test of validity for the application of the extension of the QF-processes to the study of key reactions in astrophysics.

Similar results can be obtained considering ^{6}Li(d,α)^{4}He reaction, as shown in fig.3.6. Normalizing at high energies (where electron screening actually are not strong enough), direct and indirect measurements must be in accord to each other, as shown in fig.3.5 and fig.3.6. In these two figures the dual convenience coming from THM method application are shown. It allows low- energy measurements (few keV in this case) in the quasi-free center of mass system, even if the beam

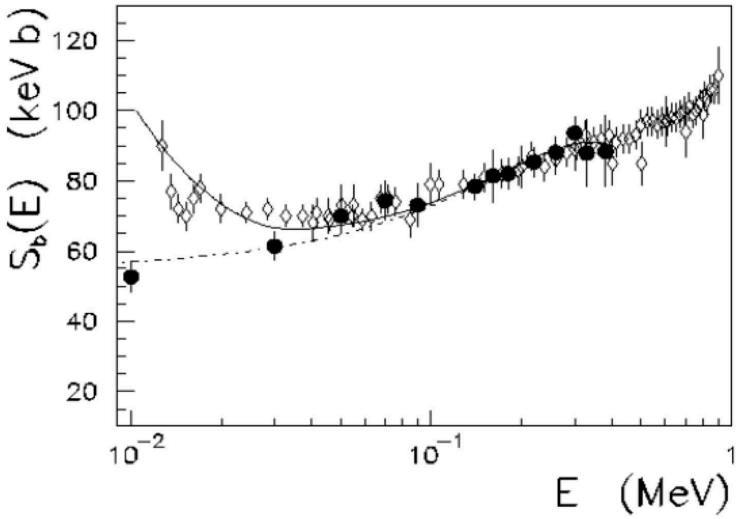

FIGURE 3.5: The ^{7}Li(p,α)^{4}He TH S(E)-factor (full circles) [18] compared with direct data (open circles) [18]. In this study the deuteron was used like TH-nucleus and the neutron acted as spectator.

energy is above the Coulomb barrier, and the possibility to gain access to the bare-nucleus cross-section.

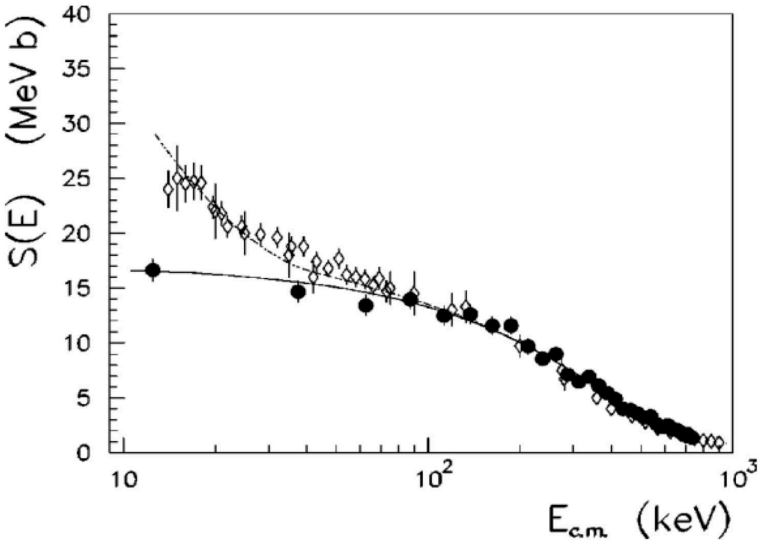

FIGURE 3.6: The ^{6}Li(d,α)^{4}He TH S(E)-factor (full circles) [19] compared with direct data (open circles).

Another validity test can be done measuring a two-body cross-section using two different three-body reaction using THM, verifying the independence of the cross-section from the Trojan Horse nucleus [114]. For example the ^{7}Li(p,α)^{4}He can be studied using d(^{7}Li,$\alpha\alpha$)n (deuterium break-up) or ^{7}Li(^{3}He,$\alpha\alpha$)d (^{3}He break-up). In fig.3.7a) the experimental excitation function of ^{7}Li(p,α)^{4}He, obtained using

THM using ^{3}He as TH nucleus (full circles), is shown in comparison with direct data (empty symbols). In 3.7b) is shown a comparison between ^{7}Li(p,α)^{4}He cross section evaluated using ^{3}He(full circles) and d(empty circles) as TH nucleus.
In both works, two resonances, associated with the group of ^{8}Be states between 19.9 and 20.2 MeV and that around 22.2 MeV of excitation energy were observed and well reproduce within the experimental uncertainties.

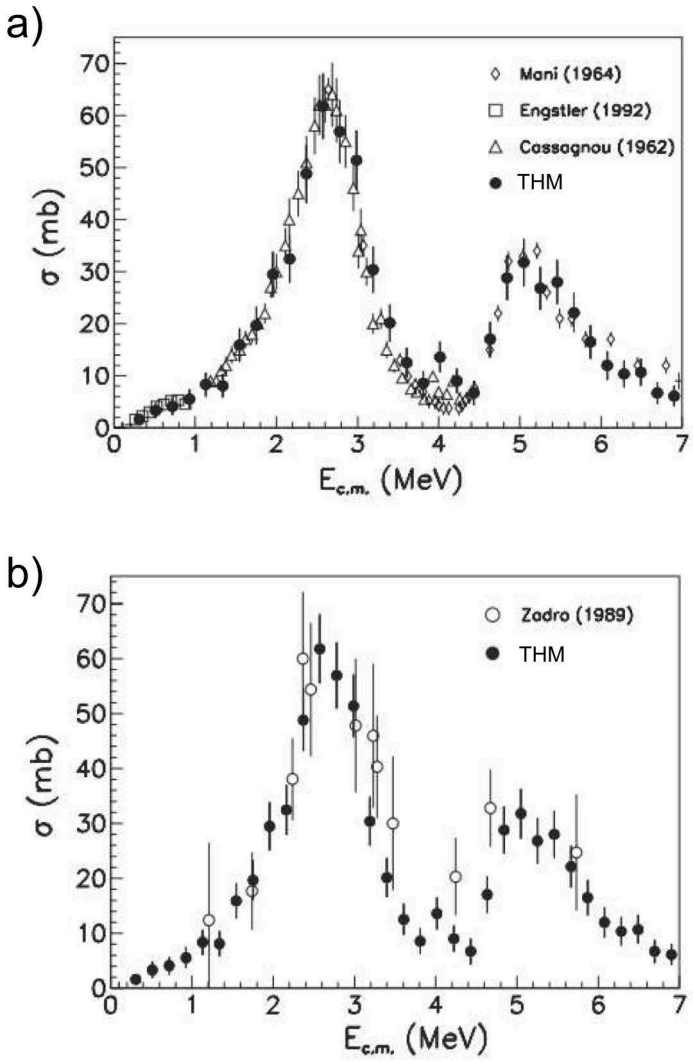

FIGURE 3.7: The ^{7}Li(p,α)^{4}He TH S(E)-factor obtained using the ^{3}He (panel a)) and deuteron (panel b)) like TH-nucleus respectively.

This confirms the polar invariance, the A+x $\rightarrow$ c+C cross section located at the lower vertex in fig.3.3 is independent from the virtual break-up in the upper vertex. Briefly, according to the theoretical description of the method, no hypothesis are made on the nature of the TH nucleus in the three-body channel: therefore, if

the participant is the same in the two-body channel (e.g. ^{7}Li+p), the changing of the spectator (neutron as in d(^{7}Li,$\alpha\alpha$)n or deuteron as in ^{7}Li(p,α)^{4}He) does not influence the final result of interest.
So it is possible to say that the cross-section is independent from the s cluster (the spectator), or at least distortion effects in both cases are inside the experimental errors.

3.7 Application of the THM

The Trojan Horse Method consents to study a large amount of reaction and has been applied in several experiments in order to cover the open questions regarding the cross-section of the astrophysically relevant reactions in astrophysics.

A list of the reactions studied by means of THM is given in Table 3.1 together with the relevant references. In particular, in this table we can see the main topics investigated by the THM:

- Primordial Nucleosynthesis: nuclear reaction rates are among the most important input for understanding the primordial nucleosynthesis and therefore for a quantitative description of the early Universe. Focusing only on the products of the BBN, according to the Standard Big Bang Nucleosynthesis model (SBBN), only the formation of light nuclei (^{2}H,^{3}H,^{4}He,^{7}Li) is predicted in observable quantities, starting from protons and neutrons. Reactions of interest for the SBBN model, i.e. ^{7}Li(p,α)^{4}He, ^{2}H(d,p)^{3}H, ^{2}H(d,n)^{3}He, ^{3}He(d,p)^{4}He, were studied by means of the THM in the energy range of interest and their measurements were performed in an experimental campaign which took place in the last decade. The knowledge of the bare nucleus cross section is important in the study of the primordial nucleosynthesis, in particular to constrain the present-day models. On the other hand, they have been used to validate the most common models used to calculate the electron screening potential. In particular, reactions among light nuclei bear a great relevance as they might be used in fusion reactors, in the same energy range (E<100 keV) as astrophysics.

Two-body reaction	**three-body reaction**	**TH nucleus (x cluster)**	**Reference**
p(p,p)p	d(p,pp)n	^{2}H (p)	[115]
d(d,p)^{3}H	d(^{6}Li, p^{3}H)^{4}He	^{6}Li (d)	[116]
d(d,p)^{3}H	d(^{3}He, p^{3}H)H	^{3}He (d)	[117]
d(d,n)^{3}He	d(^{3}He, n^{3}He)H	^{3}He (d)	[117]
^{3}He(d,p)^{4}He	^{6}Li(^{3}He, pα)^{4}He	^{6}Li (d)	[17]
^{6}Li(d,α)^{4}He	^{6}Li(^{6}Li,$\alpha\alpha$)^{4}He	^{6}Li (d)	[19]
^{6}Li(p,α)^{3}He	d(^{6}Li,α^{3}He)n	^{2}H (p)	[104, 118]
^{7}Li(p,α)^{4}He	d(^{7}Li,$\alpha\alpha$)n	^{2}H (p)	[19]
^{7}Li(p,α)^{4}He	^{7}Li(^{3}He,$\alpha\alpha$)d	^{3}He (p)	[118, 119]
^{9}Be(p,α)^{6}Li	d(^{9}Be,α ^{6}Li)n	^{2}H (p)	[120]
^{10}B(p,α)^{7}Be	d(^{10}B,α ^{7}Be)n	^{2}H (p)	[121]
^{11}B(p,α)^{8}Be	d(^{11}B,α ^{8}Be)n	^{2}H (p)	[102, 122]
^{15} N(p,α)^{12}C	d(^{15}N,α ^{12}C)n	^{2}H (p)	[123]
^{18}O(p,α)^{15}N	d(^{18}O,α ^{15}N)n	^{2}H (p)	[124]
^{17}O(p,α)^{14}N	d(^{17}O,α ^{14}N)n	^{2}H (p)	[125]
^{13}C(α,n)^{16}O	^{13}C(^{6}Li,n^{16}O)d	^{6}Li (α)	[126]
^{19}F(p, α)^{16}O	d(^{19}F, α^{16}O)n	^{2}H (p)	[127]
^{6}Li(n,α)^{3}H	d(^{6}Li,α ^{3}H)p	^{2}H (n)	[128]

TABLE 3.1: Application of the THM.

- Light-elements depletion problem: the abundance of the light elements, such as lithium, beryllium and boron, plays a key role for a number of not yet completely solved astrophysical problems, e.g. the big bang nucleosynthesis and the lithium depletion in the Sun or in other galactic stars. Both production and destruction mechanisms must be studied and their cross sections should be measured in the relevant Gamow energy window. These elements are mainly destroyed in the stellar interior by (p,α) reactions and the cross sections of these reactions are necessary inputs for astrophysical models studying the light element abundance in the universe. Then great effort has been devoted to the study of relevant reactions, such as ^{6}Li(p, α)^{3}He, ^{6}Li(d, α)^{4}He, ^{7}Li(p, α)^{4}He, ^{9}Be(p, α)^{6}Li, ^{10}B(p, α)^{7}Be, ^{11}B(p, α)^{8}Be, at astrophysical energies.

- Fluorine Nucleosynthesis in AGB stars: the fluorine abundances is very sensitive to the physical condition in giant stars and for this reason it is used as probe for AGB models and nucleosynthesis and is one of the most important input parameters for an analysis of s-process in AGB star conditions. Thus, the study of the nuclear reactions involved in ^{19}F production and destruction is needed. A key role for ^{19}F production is played by the ^{15}N(p, α)^{12}C reaction which removes both ^{15}N and protons from the production chain of ^{19}F in AGB stars. Also the ^{19}F(α,p)^{22}Ne and ^{18}O(p,α)^{15}N reactions can affect fluorine abundance in AGB stars, the first one being involved in ^{19}F destruction, whereas the second reaction implies the production of ^{15}N that can increase the nitrogen supply in the burning chain producing ^{19}F. In the case of extra-mixing phenomena, which are characterized by a maximum temperature of about 10^7 K, the ^{19}F(p, α)^{16}O reaction is of key importance. These reactions have been studied by means of the THM.

- Neutron induced reactions: the THM was successfully applied to the d(^{6}Li,α^3H)p reaction with the aim to study the quasi-free contribution to the ^{6}Li(n,α)^{3}H reaction, where the Coulomb barrier effects are absent. The very good agreement with direct data in the literature validates the pole approximation for this experiment. This kind of application needs to be further confirmed also in view of future applications to key astrophysical reactions using deuterons as a source of a virtual neutron beam.

- Nuclear Physics application: another application of the THM concerns the indirect study of the p-p elastic scattering. It is well known that in such a simple process the interference terms between Coulomb and nuclear amplitudes are expected to contribute to the cross section. In particular the combination of the two effects gives rise to a destructive interference which leads to a deep minimum in the cross section. The THM has been applied to the d(p,pp)n reaction. In the THM hypothesis the Coulomb effects are suppressed in the two-body cross section at sub-Coulomb energies. For this reason, we can expect that the interference contribution should be absent and the two-body cross section should not display the deep minimum. The THM data shows that the p-p cross section is completely dominated by the nuclear field as is expected in the higher energy region. This strongly confirms the Coulomb suppression hypothesis which makes the THM the unique

experimental method able to investigate nuclear effects at low energies, not only in the framework of nuclear astophysics.

3.8 The ^{19}F(p,α)^{16}O: the first run

The astrophysical environments where the ^{19}F(p,α)^{16}O reaction plays an important role were illustrated in the chapter 1.
To provide a more accurate S-factor at astophysical energies, we have applied the THM to the d(^{19}F, $\alpha_0{}^{16}$O)n quasi-free reaction.
The experiment was performed at Laboratori Nazionali del Sud di Catania in 2008 where the Tandem accelerator provided a 50 MeV ^{19}F beam impinging onto deuterated polyethylene targets.
In this case the reaction occurring through ^{2}H break-up, where the proton is the participant and neutron is the spectator of the two-body reaction.
The experimental setup consisted of a telescope devoted to oxygen detection, made up of an ionization chamber and a silicon position sensitive detector on one side with respect to the beam direction and four additional silicon PSD on the opposite side of the beam axis optimized for coincident detection of the α particles.

The experimental data show the presence of three resonance groups corresponding to ^{20}Ne states at:

- 12.957 and 13.048 MeV;
- 13.222, 13.224, and 13.226 MeV;
- 13.529, 13.586, and 13.642 MeV.

The normalized yield was fitted simultaneously with four Gaussian curves to separate the resonance contributions, as shown in fig. 3.8.

It was obtained by evaluating the E_{cm} spectrum (where $E_{c.m.}$, as defined in equ. 4.6, is the ^{19}F-p relative kinetic energy related to $E_{\alpha-^{16}O}$ relative energy by the energy conservation law:

$$E_{cm} = E_{^{19}F-p} = E_{\alpha-^{16}O} - Q_{2body} = E_{\alpha-^{16}O} - 8.11MeV \tag{3.40}$$

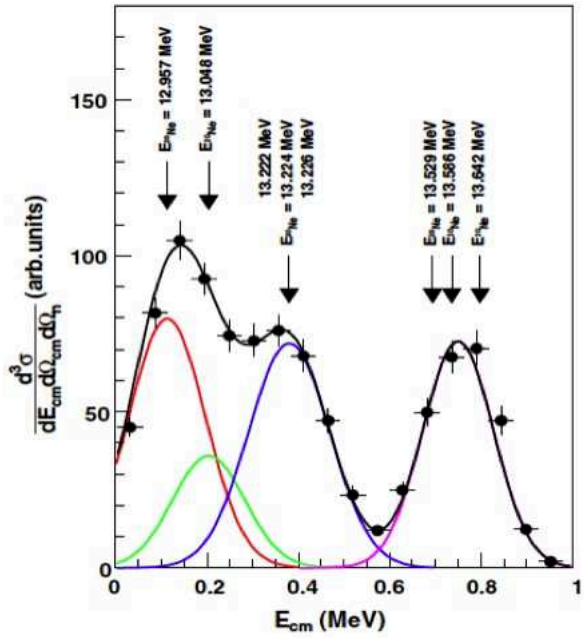

FIGURE 3.8: Normalized coincidence yield of the d(^{19}F, α_0^{16}O)n reaction. The black circles are the experimental data, the horizontal error bars p-^{19}F-relative-energy binning and the vertical ones the statistical uncertainties.

) and dividing out the expected modulation by the product of the phase-space factor and of the p-n momentum distribution.

By integrating over the angular distributions of the ^{19}F(p,α_0)^{16}O sub-reaction, the $\frac{d_2\sigma}{d\Omega_n dE_{cm}}$ cross section is deduced in arbitrary units, as shown in fig.3.9. This cross section clearly shows a resonance behaviour, in particular the peak centred at about 800 keV can be attributed to the overlap of the 13.573, 13.586 and 13.642 MeV levels of ^{20}Ne. The two peak at lower energies can be due to the population of the 13.222, 13.224 and 13.226 MeV states, leading to a enhancement of the $\frac{d_2\sigma}{d\Omega_n dE_{cm}}$ cross section around 0.4 MeV, while the peak sitting at ∼150 keV might be traced back to the decay from the 13.048 and 12.957 MeV levels in ^{20}Ne.

The experimental TH cross section was analyzed in the modified R-matrix approach to explore the energy region $E_{c.m.} \leq 1$ MeV, spanning both the range of astrophysical importance and the energy interval 600 keV $\leq E_{c.m.} \leq$ 800 keV, where resonances were present that could be used for normalization. In particular, above 0.6 MeV, the reduced partial widths were obtained through an R-matrix fit of direct data, below 0.6 MeV, the resonance parameters were obtained from the modified R-matrix fit and finally the non-resonant contribution is taken from NACRE.

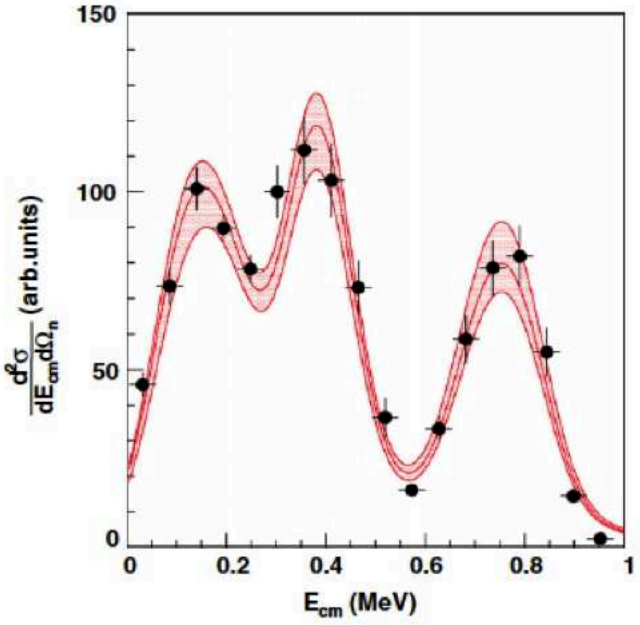

FIGURE 3.9: QF cross section of the d(^{19}F, α_0^{16}O)n reaction in arbitrary units. The red band is the cross section calculated in the modified R-matrix approach, normalized to the peak at about 750 keV and convoluted with the experimental resolution. The vertical error bars statistical and angular-distribution integration uncertainties.

As said in section 3.3 under the simplified assumptions used to deduce the THM astrophysical factor no absolute values could be defined and normalization to direct data was necessary. As a first step to normalization, a weighed fit of the direct S(E)-factor data available in the literature, down to about 0.6 MeV, was performed by means of standard R-matrix formulas (see section 2.64, [88]). In this way, the resonance parameters of the 13.529, 13.586 and 13.642 MeV states in ^{20}Ne were obtained. The normalization factor was then deduced by scaling the calculated $\frac{d_2\sigma}{d\Omega_n dE_{cm}}$ to the experimental TH cross section in the overlap region between direct and indirect data.

Cross section data have been transformed into the S(E) astrophysical factor and compared to data reported in the literature; the results are shown in fig. 3.10.

The S(E)-factor of the α_0 channel shows the presence of resonant structures not observed before which is in disagreement with the NACRE S(E)-factor showing a non-resonant behavior from 0.6 MeV downward, but confirmed by the new data in [16] (see section 2.7).

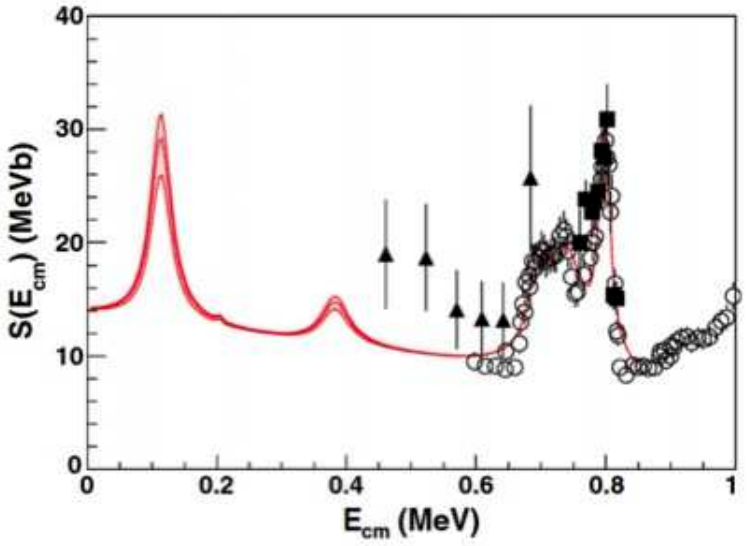

FIGURE 3.10: R-matrix parameterization of the 19F(p,α_0)16O astrophysical factor.

The preliminary results for the α_0 channel are shown in a letter to the Astrophysical Journal [127]. To sum up, for the first time the presence of resonances in the ^{19}F(p,α_0)^{16}O reaction at astrophysical energies has been pointed out, that cause a significant increase in the reaction rate at astrophysical temperatures, with important consequences for stellar nucleosynthesis.

Anyway, statistics turned out to be scarce as the α_1 channel was dominant, preventing one to draw accurate quantitative conclusions from the data for the α_0 channel. The promising results motivate the request of a second run focused on the investigation of the α_0 channel that I will show in the next chapter. In fact, from the previous experiment a phase-space region has been found where the α_1 channel is suppressed, thus leading to an improved determination of the ^{19}F(p,α_0)^{16}O cross section.

Chapter 4

A new measurement of the ^{19}F(p,α)^{16}O reaction through the Trojan Horse Method

As mentioned in the previous chapter, an improved study of the ^{19}F(p,α)^{16}O reaction cross section in the relevant astrophysics region has been performed by means of the Trojan Horse Method [102].

In general, relatively simple experimental setups in THM experiments are needed. Usually the detection setup consists of two or more couples of coincidence telescopes arranged at opposite side of the beam direction at quite forward angles, the experiments being usually performed in inverse kinematics with a deuteron target as a virtual-proton target. Only two of the three emitted particles in a reaction event are detected in coincidence, while the third one (tipically the neutron spectator) is not detected. To completely determine the kinematical properties of the spectator particle, in particular its momentum distribution, energies and emission angles of the two particles must be measured.

Moreover, is important to optimize the kinematical conditions for the presence of QF mechanism under the assumptions of the IA. In fact, a necessary condition for the application of the method is that QF mechanism yields a dominant contribution to the $2 \rightarrow 3$ cross section. But, competing reaction mechanisms might contribute in the same relative momentum region.

For this reason an accurate experimental planning is required in order to fulfill

the model approximations and a number of steps are involved in the data analysis before the two-body cross section of astrophysical relevance can be extracted.

4.1 Application of the THM

A first task in planning a THM measurement is the selection of an appropriate three-body reaction and of a suitable TH-nucleus that has a large amplitude for the cluster configuration. A list of possible TH-nuclei is shown in table 4.1.

TH nucleus	**x-s cluster structure**	**Orbital angular momentum**	**Binding energy (MeV)**
^{2}H	p-n	0	2.225
^{3}H	d-n	0	6.257
^{3}He	d-p	0	5.493
^{6}Li	d-α	0	1.474
^{9}Be	^{5}He-α	0	2.464
^{16}O	^{12}C-α	0	7.162
^{20}Ne	^{16}O-α	0	4.730

TABLE 4.1: Structure, orbital angular momentum and binding energy for some TH-nuclei.

The TH-nuclei listed in the table are characterized by an orbital angular momentum l=0 for the intercluster motion. In this condition, the momentum distribution shows a peak at $p_s = 0$. This choice is linked to the reduction of experimental difficulties when selecting the QF mechanism. However, other system with l=1 orbital angular momentum are also available, i.e. ^{7}Li (^{3}H+α) or ^{7}Be (^{3}He+α).
A large number of reaction studied by means of the THM are (p, α) reactions at stellar energies performed in inverse kinematics with a deuterated polyethylene target to supply virtual protons from the deuteron with neutron as spectator (B_{pn}=2.225 MeV).
An alternative source of virtual protons is represented by ^{3}He, in which case deuteron act as a spectator (B_{pd}=5.493 MeV).
It is clear that different choices of TH nuclei are available to get the same virtual participant.

The choice of an appropriate TH-nucleus among those made up of the same participant cluster but different spectator is mainly linked to [129]:

- the minimum value of binding energy of the cluster system in the TH nucleus;
- the appropriate incident energy of the projectile;
- the Q-value of the three-body reaction and the value of the transferred momentum;
- the population of kinematic regions where the different contributing reaction mechanism with three particles in the final state (i.e. sequential decay or direct break-up) are minimized;
- the knowledge of the intercluster momentum distribution.

The choice of a deuteron as the Trojan Horse nucleus is suggested by a number of reasons [129]:

- its binding energy is low;
- its wave function is well known [130];
- it has a simple cluster structure (proton plus neutron);
- the cluster spectator is not charged (neutron);
- the p-n intercluster motion takes place at $l = 0$ and the QF break-up occurs in the target nucleus, thus the momentum distribution has a maximum for $p_s = 0$ MeV/c.

In addition, the deuteron can be used as a source besides virtual protons also neutrons, thus allowing for investigations of neutron-induced reactions avoiding the experimental problems connected to the use of neutron beams [128, 131].

Therefore the d(^{19}F,α^{16}O)n three-body reaction has been chosen in order to extract the ^{19}F(p,α)^{16}O two-body cross section.
In particular a ^{19}F beam has been adopted so that no gas target is necessary, deuterium being available in solid form as deuterated polyethylene.

4.2 Experimental planning

A schematic view of the QF three-body reaction proceeding through deuteron break-up is reported in fig.4.1

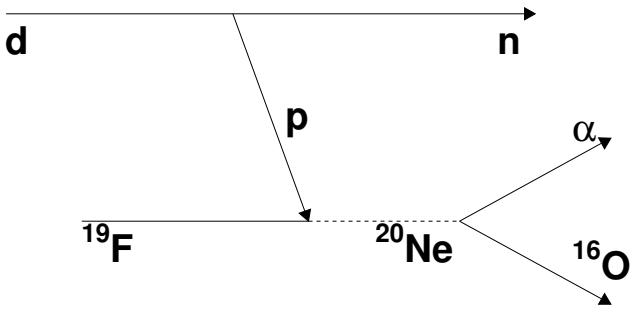

FIGURE 4.1: Schematic diagram representing the d(^{19}F,α^{16}O)n QF process.

In this figure the upper pole represents the virtual two body reaction and the lower pole represents the break-up for the deuteron used asTH nucleus.
Since the relative motion of the neutron-proton system inside deuteron takes place essentially in s-wave (l=0), and the QF break-up occurs in the target nucleus, the experimental momentum distribution is expected to be peaked at p_n=0 MeV/c. Its analytical expression is given in terms of Hulthen wave function [130] with a maximum at relative momentum p_n=0 Mev/c.
Under these hypotheses, the ^{19}F is considered to interact only with a part (proton) of the deuterium nucleus, while the other part (neutron) is considered as spectator to the ^{19}F(p, α)^{16}O virtual reaction.
As regards the beam energy, the main physical constraint is connected to the hypothesis that the energy of the impinging particles overcomes the Coulomb barrier in the entrance channel of the three-body reaction A+a→c+C+s, this allows to extract the cross section of the astrophysical reaction of interest, x+A→c+C, free of Coulomb suppression. Also the incident energy in the center-of-mass system E_{aA} as well as the detection angles have to be chosen so that the relative energy E_{xA} can span the region below the Coulomb barrier, as said in the section 3.3.

In the present case the beam energy in the center-of-mass system of the ^{19}F+d channel exceed about 2.5 MeV, that is the Coulomb barrier evaluated by means

of equation 2.10. Using the formula described in the section 3.3:

$$\Delta E_{qf} = E_{Ax} - B_{xs} \pm E_{xs} \tag{4.1}$$

The beam energy is then fixed by inverting this relation:

$$E_{Ax} = E_{qf} + B_{xs} \tag{4.2}$$

where E_{ax} is the value of the beam energy in the center of mass of the two body reaction, B_{xs} represents the binding energy of the p-n system in the deuteron and E_{qf} represents the Gamow peak energy, which in this case is about 40 keV. Assuming E_{qf} =40 keV and using the deuteron binding energy B_{xs}=2.2 MeV the beam energy is:

$$E_{beam} = (B_{p-n} + E_{qf}) \left(\frac{m_p + m_{^{19}F}}{m_p} \right) \approx 45 MeV \tag{4.3}$$

The beam energy as derived from this equation is not strictly determined, allowing to select the phase space region where the quasi-free contribution are expected be dominant.
For this reason in the first run we selected a 50 MeV beam energy. In this second run a 55 MeV beam energy was selected.
The increase of 5 MeV in the beam energy with respect to the previous experiment would allow for a better coverage of the relevant energy region (0-1 MeV) for the selected angular ranges. These were chosen to reduce the contribution of the α_1 channel. Indeed, from the previous THM run, it turned out that only at large α-emission angles (with respect to the beam direction) the detection of the α_1 channel is less likely as the available phase space region is strongly limited (25% of the one available for the decay to the ^{16}O ground state).

Once that the beam energy is fixed, it is possible to perform a detailed study of the simulated kinematical condition for the chosen three-body reaction at this energy.

4.3 QF kinematical conditions

From a detailed study of a Monte Carlo simulation it is possible to derive all the quantities of interest for the three-body reaction, such as energies and angles of the particles in the exit channel. In this way, is possible to select the kinematical condition at which the QF contribution to the three-body cross section is expected to be maximum.

By considering the energy and momentum conservation laws for a general reaction A(a,cC)s, it is possible to write the following system:

$$\begin{cases} E_A + Q = E_c + E_C + E_s \\ \vec{p_A} = \vec{p_c} + \vec{p_C} + \vec{p_s} \end{cases} \tag{4.4}$$

If the relative motion of the spectator particle occurs mainly with l=0, it will possible to assume p_s=0 MeV/c, that is E_s=0 MeV. By using this assumption, the system 4.4 can be written as

$$\begin{cases} E_A + Q = E_c + E_C \\ p_A = p_c cos\theta_c + p_C cos\theta_C \\ 0 = p_c sen\theta_c + p_C sen\theta_C \end{cases} \tag{4.5}$$

This equation system is made of three relations, the unknown variables being the energies and emission of ejectiles c and C. Therefore for every fixed detection angle of particle c or C, the emission angle of the other particle is fully determined by the system 4.5 and a particular locus in the $\theta_c - \theta_C$ two-dimensional plot is picked out.

The angular pair (θ_c, θ_C) represents the QF-angular pair, at which the detected particle have an high probability to derive from the QF-process. In this case of a dominant s-wave in the x-s relative motion are the angles at which $p_{sx} = 0$ MeV/c. The same consideration can be made in the case of a TH nucleus having an intercluster motion that occurs mainly in terms of a $l \neq 0$ partial wave. For instance, if the momentum distribution has a maximum for a given p_l, to derive the QF angles should impose p_s=p_l and equivalently $E_s = \frac{p_l^2}{2m_s}$.

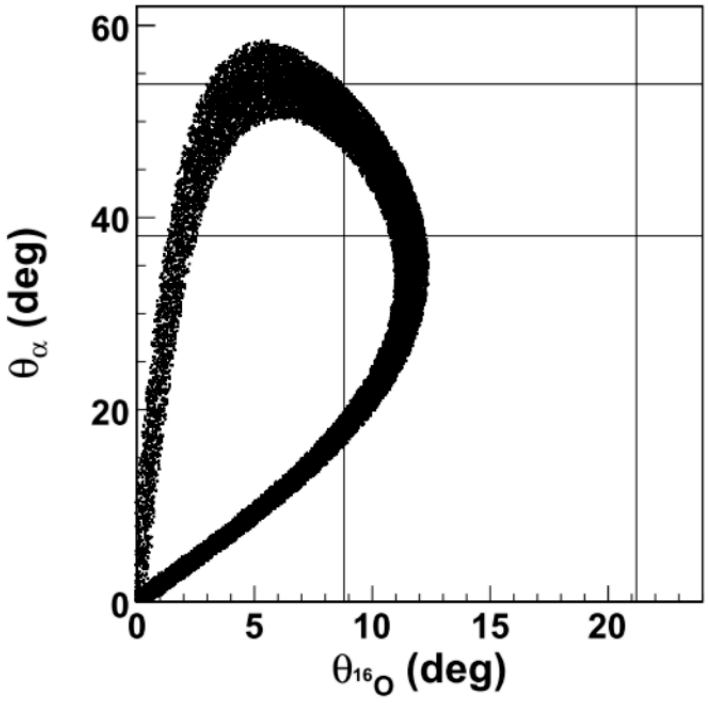

FIGURE 4.2: θ_{He} vs. $\theta_{^{16}O}$ two-dimensional plot for the d(^{19}F,α^{16}O)n reaction, for $|p_s|$<10MeV/c (QF kinematical conditions). Vertical lines: detector 1 (see text), spanning 8.8°−21.2°, optimized for ^{16}O detection. Horizontal lines mark the angular range spanned by detector 2 (see text) for α-particle detection, 38.1°−53.9°.

The $\theta_{^4He}$ vs. $\theta_{^{16}O}$ spectrum shown in Fig.4.2 is the result of a Monte Carlo calculation performed at 55 MeV beam energy, in which only the QF kinematics has been selected, that is only events with a spectator momentum $|p_s|$ <10 MeV/c were reported. In the actual approach the spectator particle is a neutron, coming from direct deuteron breakup. In these kinematical conditions the momentum transferred to the spectator is very small, the THM applicability conditions are best fulfilled and thus the QF reaction mechanism is expected to be more important.

As shown in Fig. 4.2, the ^{16}O fragments from the d(^{19}F,α^{16}O)n QF reaction cover the 0° -12° angular region whereas the α-particles are emitted from 0° to 60°, in the reaction plane, on the opposite side with respect to the beam direction.

However, the position of detectors has to take into account a number of experimental constraints. For instance, very small angles have to be ruled out because of the high elastic scattering counting rate.

For this reason the regions where we detected ^{16}O and α-particles emitted in a QF

reaction event, respectively, spanning 8.8° - 21.2° and 37.1° - 54.9°.
Moreover QF angles are selected in such a way to span the A-x relative energy interval of astrophysical interest and where no contributions from sequential mechanism are expected.

The kinematical locus for the events coming from the d(^{19}F,$\alpha_0{}^{16}$O)n three-body reaction performed at 55 MeV beam energy was studied; the result is reported in figure 5.3.

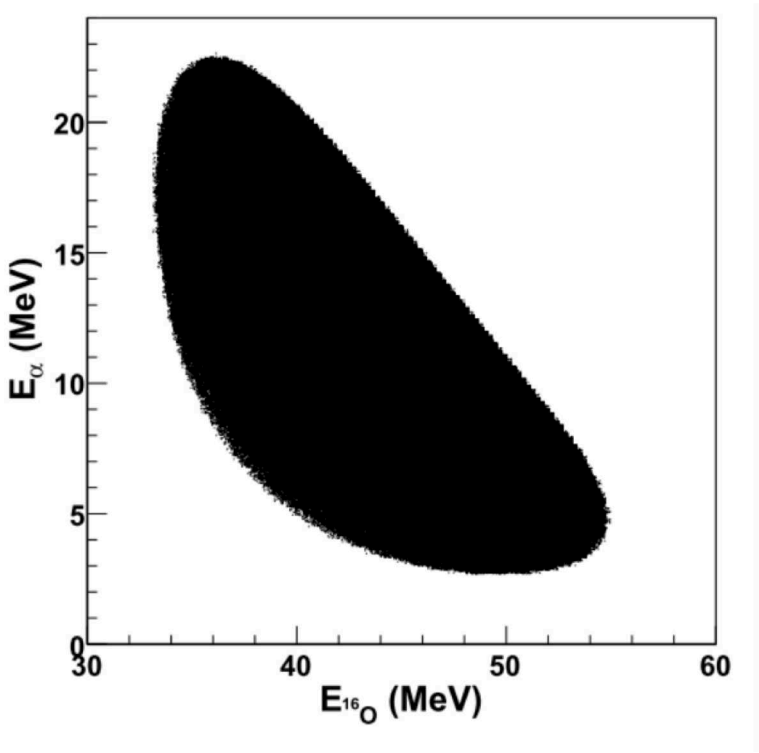

FIGURE 4.3: $E_{^4He}$ vs. $E_{^{16}O}$ two-dimensional plot for the d(^{19}F,$\alpha_0{}^{16}$O)n reaction, for the whole p_s range.

The knowledge of the spanned energy intervals is needed for a more convenient detector choise.

The relative energies E_{cm}, at which the two-body astrophysically relevant reaction is induced, is easily calculated from the post-collision prescription as the difference:

$$E_{cm} = E_{^{19}F-p} = E_{\alpha-^{16}O} - Q_{2body} \tag{4.6}$$

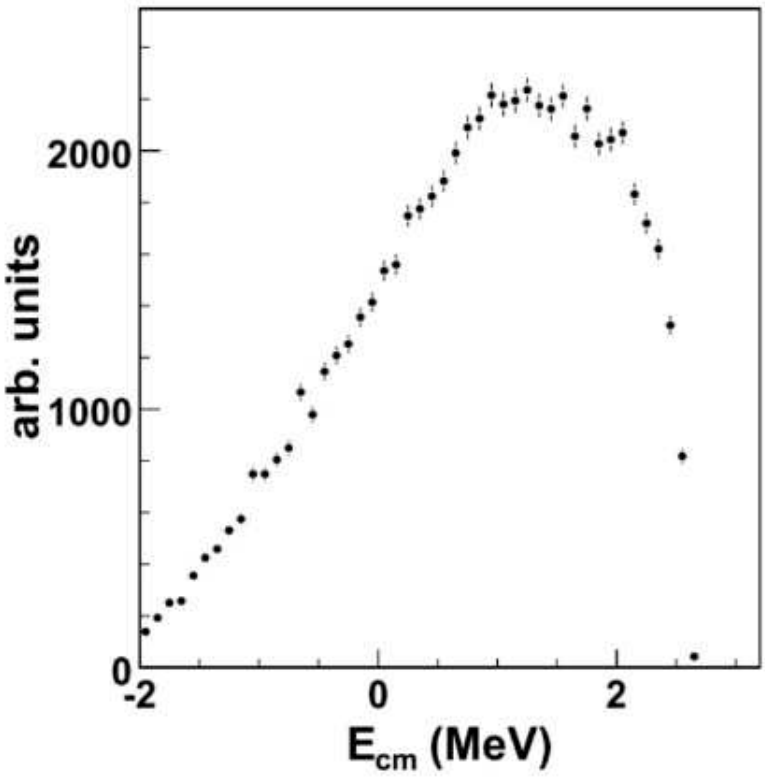

FIGURE 4.4: Simulated phase space factor as a function of $E_{c.m.}$ for the d(^{19}F,$\alpha_0{}^{16}$O)n reaction. The angular and momentum conditions (p_s<40 MeV/c) are all included. The energy region between 0 and 1 MeV is fully covered, as well the sub-threshold region.

where $E_{\alpha-^{16}O}$ represents the relative energy between the detected ^{16}O and α particles and Q_{2body} is the Q-value for the two-body reaction of interest (for the present reaction Q_{2body}=8.11 MeV).

From this approach, it is obvious that one of the most important quantities to study is the relative energy between these two particles. Figure 4.4 represent the $E_{\alpha-^{16}O}$ spectrum, while figure 4.5 represents the diagram describing the behavior of the relative energy $E_{\alpha-^{16}O}$ as a function of the neutron momentum p_n.

From this last one, it can be observed that the energetic region of astrophysical interest corresponds to the low-momenta for the neutron: the selection of such values for the neutron momentum, and then the selection of a kinematical region in which these condition are fulfilled, corresponds to the selection of a region in which a strong contribution of the QF-mechanism to the three-body reaction is expected.

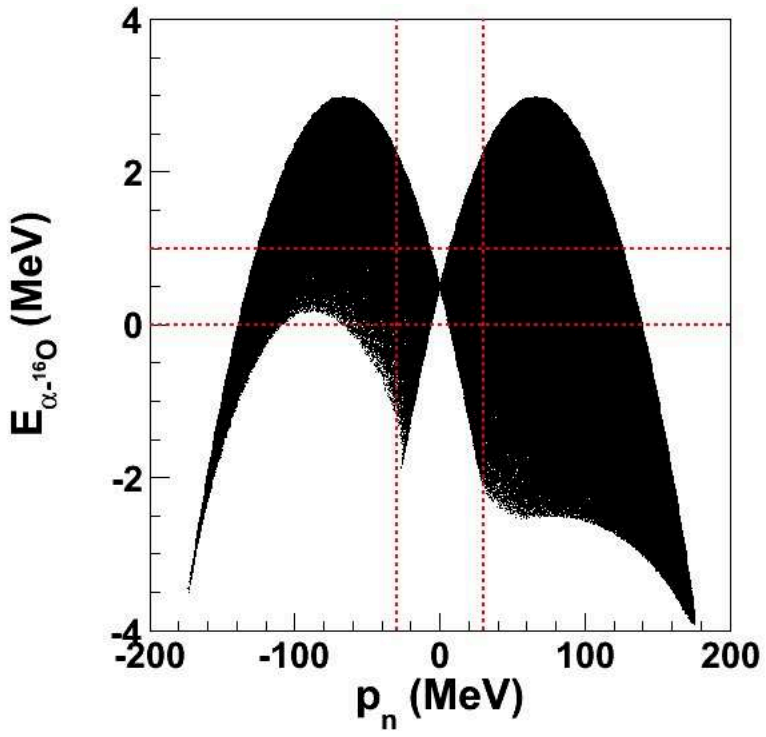

FIGURE 4.5: Simulated $E_{\alpha-^{16}O}$ vs. p_n two-dimensional plot: the energetic region of astrophysical interest (0-1 MeV) is reached for low-momentum values ($|p_s|$<30 MeV/c) of the neutron. This assures the selection of the kinematical condition at which a strong contribution of the QF-mechanism on the three-body reaction is expected.

4.4 Sequential Decay

As said in section 3.2, besides QF contribution, the $^{16}O + \alpha +$ n exit channel can be fed through different reaction mechanism, in particular sequential decay (SD) and direct break-up (DBU).

In order to apply the Trojan Horse Method one needs to separate this contribution from all the others which may occur between the same target and projectile, giving the same particles in the exit channel.

Therefore an accurate preliminary investigation of the resonance states in ^{17}O and ^{5}He compound nuclei, that can be excited in the selected phace space region of the d(^{19}F,$\alpha^{16}O$)n three-body reaction, has needed.

A schematic view of the SD mechanism proceeding through the formation of the ^{20}Ne (panel a)),^{17}O (panel b)) and ^{5}He (panel c)) compound system is reported in figure 4.6. In the first one case the SD contribution feeding the same exit channel is given by the QF contribution and the procedure to disentangle the QF mechanism

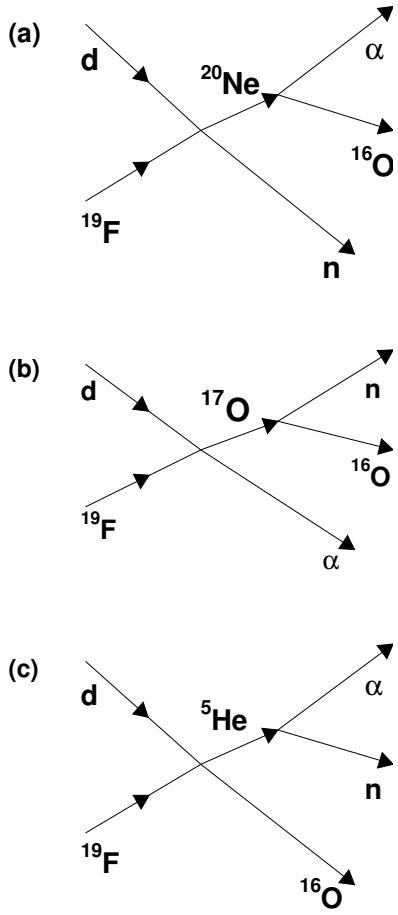

FIGURE 4.6: Schematic diagram representing the SD processes which can contribute to the d(^{19}F,α^{16}O)n reaction cross section.

from the SD contribution is more complex. The presence of a correlation between the three-body cross section and the neutron momentum represent a necessary condition for the occurrence of the QF reaction mechanism and it can be useful to disentangle the QF from SD yield.

In this context it is clear that a detailed study and the discrimination of such mechanisms represents an important stage of a TH analysis.

This kind of information can be reached studying the relative energy between the particles in the exit channel. In particular, the study of any two among the $E_{\alpha-16O}$, E_{n-16O} and $E_{\alpha-n}$ relative energies allows to obtain information on the presence of excited states of ^{20}Ne, ^{17}O and ^{5}He. Once this stage of analysis is confirmed, it will be possible to apply the THM to the three-body data for the extraction of the cross-section of interest. A more detailed discussion is reported in the following sections.

4.5 Experimental setup and procedures

The new measurement was performed in July 2012 at the Laboratori Nazionali di Legnaro (INFN-LNL) where the Tandem-XTU accelerator provided a 55 MeV ^{19}F beam with a spot size on target of 1 mm and intensities around 1-3 nA. Thin self-supported deuterated polyethylene target (CD_2) of about 95 μg/cm^2, was adopted in order to minimize energy and angular straggling and was placed at 90° with respect to the beam direction.

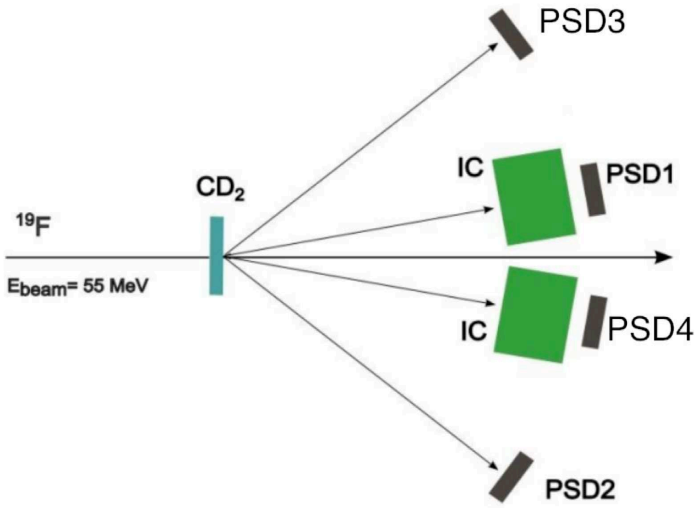

FIGURE 4.7: Schematic view of the experimental setup.

A drawing of the experimental setup is given in figure 4.7. It consisted of a telescope optimized for ^{16}O detection to discriminate oxygen nuclei via the ΔE-E technique (as explained below), made up of an ionization chamber (IC) and a silicon position sensitive detector (PSD1) on one side with respect to the beam direction and an additional silicon PSD on the opposite side of the beam axis optimized for coincident detection of the alfa particles (PSD2). A symmetric setup allowed to double the statistics. Angles and distances for each PSD are summarized in table 4.2. In figure 4.8 a picture of the detection setup is shown.
In order to minimize the angular straggling in PSD1, a 0.9 μm thick Mylar foil was used as the entrance window; the opposite side was closed by a 1.5 μm thick Mylar foil. The IC was filled with 50 mbar butane gas that provided an energy resolution of about 10%, which was enough to discriminate the impinging particles

according to their nuclear charge but not their mass. No threshold was introduced in the ^{16}O detection by the ionization chamber.
The two 1000-micron PSD (5.1 cm^2) having energy and position resolution 0.5% and 0.3 mm respectively and covering the 8.8° - 21.2° and 37.1° - 54.9° angular range.

	PSD1	**PSD2**	**PSD4**	**PSD3**	**IC**
Center (deg)	15	46	15	46	15
Distance from target	23	18	23	18	16
Thickness (μm)	1000	1000	1000	1000	50000

TABLE 4.2: Detector angles, positions and thicknesses.

To decrease the detection threshold, no ΔE detectors were put in front of PSD2 and the symmetric one, therefore α-particle identification was done from the kinematics of events. Energy and emission angle of the detected α's and emission angle of ^{16}O nuclei were used in the subsequent analysis to enhance energy resolution.

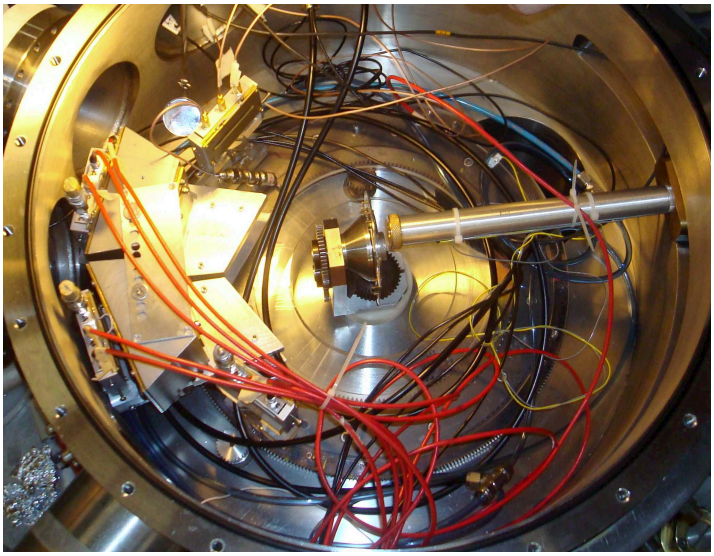

FIGURE 4.8: Picture of the scattering chamber located in the LNL.

The alignment of all detectors was checked by an optical system. The trigger for the event acquisition was given by coincidences between ^{16}O detected in the telescope and the signal of α particles coming from the other two PSDs. This allowed for the kinematical identification of our specific exit channel of reaction d(^{19}F,α^{16}O)n.

Energy and position signals for the detected particles were processed by standard electronics (see fig. 4.9) and sent to the acquisition system for on-line monitoring and data storage for off-line processing.

The position signal was directly sent to the ADC after a pre-amplification and an amplification stage. The E signal, after passing through the pre-amplifier (its role is to amplify the detector signal to a level suitable for further electronic modules), was instead split in two lines. The first one was sent to a linear amplifier, used to amplify the signal an appropriate amount (the analogical to digital converter, ADC, accepts signals up to 1V in amplitude) and then to the ADC, as for the P signal, while the second E line passed a quicker amplifier (Time Filter Ampifier, TFA) and then a discriminator module to have a logic signal before it was sent to a TAC-SCA (Time to Amplitude Converter-Single Channel Analyzer) in order to produce the coincidence event trigger.

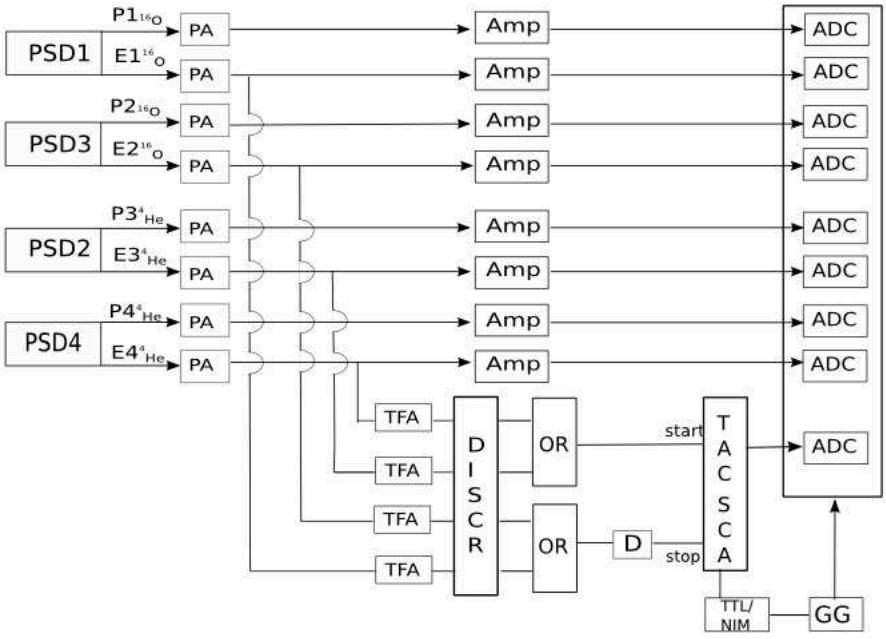

FIGURE 4.9: The electronic chain used in the experiment (see the text for details).

The start input of TAC-SCA was given by a logical-or signal coming from PSD2 and PSD4, while the signal corresponding to the ^{16}O provided the stop.

In summary, a ^{19}F beam, previously accelerated by a tandem, interacted with a ^{2}H target producing α and ^{16}O detected in four PSDs. Detector signals were processed by standard electronic chains and sent to the acquisition system which allowed the on-line monitoring of the experiment and the data storage for off-line analysis.

4.6 Detector calibrations

Before the data analysis procedure is necessary to calibrate all detectors involved in our experimental setup. Since for the application of the method is necessary to have information about the relative energies between the outgoing particle, that is correlated to the angles and energy of the involved product, the measurements of both quantities, energies and angles, is needed. In this sense the detector used are Position Sensitive Detectors that gives information about the energy of the particle and moreover the position at which the particle penetrates the detectors, so it is possible to obtain two signals: energy and position (E,P).

4.6.1 PSD working principles

Heavy charged particles lose energy by Coulomb interaction with electrons and the nuclei of the absorbing materials. The collision of heavy charged particles with free and bound electrons results in the ionization or excitation of the absorbing atom, whereas the interaction with the nuclei leads only to a Rutherford scattering between the two types of nuclei. Thus the energy spent by the particle in electronic collisions results in the creation of electron-hole pairs, whereas the energy spent in nuclear collision is lost to the detection process.
Since the net effect of a moving particle across a semiconductor is the creation of electron-hole pairs, it will be important to collect the signal produced, or the correspondent current i(t).
For the THM application is important to have information about the relative energies between the outgoing particles. Since these kinematical quantities depend on the angles and the energies of the involved products, a detector that can give information about these (E,θ) quantities for the particles is needed. In particular Position-Sensitive silicon Detectors (PSD) have the advantage to produce, from a single event of passing charged particle, an E- signal that carries the information about the energy of the particle and a P-signal that is related to the position at which the particle penetrates the detector.

In a schematic picture, a PSD can be assumed as formed by a semiconductor diode with two electrodes, as sketched in figure 4.10. In particular, while the energy E-signal is extracted from the layer with lower resistivity, the position P-signal is

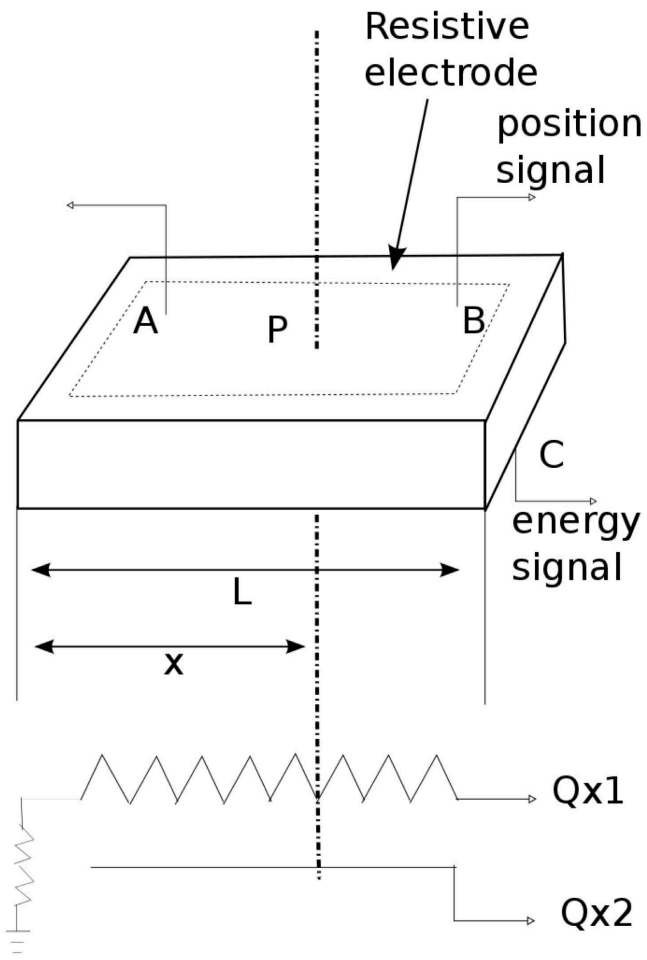

FIGURE 4.10: Schematic drawing of a Position Sensitive Detector.

extracted from the more resistant layer thanks to the charge division principle. Indeed one of the two electrodes of the detector has a non negligible resistance, thus when the electron-hole pairs that are produced by the interaction of the impinging particles with the silicon bulk are collected by the resistive electrode, the heights of the signals at the two sides of the resistive layer are inversely proportional to the resistances corresponding to distances x and L-x.
For instance, if a particle hits the detector at a point P, so that the distance of P from the left side A is x (as shown in figure 4.10), the charge collected at the right side connection B is:

$$Q_{x1} = \frac{R_2}{R_{tot}} Q_E \tag{4.7}$$

- Q_E is the total charge produced, extracted from the low-resistive electrode, that is the energy signal;

- $R_2 = \rho\frac{x}{s}$, where ρ and s are the resistivity and the surface area of the resistive electrode respectively;
- $R_{tot} = \rho\frac{L}{s}$ is the total resistance of the electrode.

Therefore the signal taken from right edge of the resistive electrode is proportional to the position, measured from the left side of the electrode itself, hit by the impinging particle:

$$Q_{x1} = \frac{x}{L}Q_E \tag{4.8}$$

Since the total charge produced is closely related to the energy of the reaction product before entering the silicon detector, the position signal is also proportional to the particle energy.
Thus one of the main aims of the position calibration is to remove the energy dependence of the position signal, as discused in the next section.

The used PSD (from Micron Semiconductors) presents three readout contacts:

- The first contact connected to the ground. It is usually grounded via 0.5 - 1 kΩ, corresponding at about 20% of the total resistive layer, which ensures a measurable signal also when the hit position is close to this end.
- The one in the middle is connected to the cathode and provides the energy signal.
- The last one is connected to the resistive anode where the charge fraction that provided the position signal is collected.

Such detectors are usually rectangular with a surface area of 50 x 10 mm^2, while their typical position resolution is about 0.1-0.3 mm FWHM, corresponding to about 150 μm, and an energy resolution better than 1% FWHM.

The signals produced are processed by a standard electronic and converted in channels for the online acquisition. In order to extract the correct information for the future analysis, it will be important to convert both E and P signals, expressed in channels, to the quantities of interest energy and position expressed in MeV and

degrees respectively. This represents the first stage of a typical experiment data analysis, that is the calibration of the involved detectors.

4.6.2 Position calibration

At the initial stage of the measurement, masks with a number of equally spaced slits were placed in front of each PSD to perform position calibration, as shown in figure 4.11.

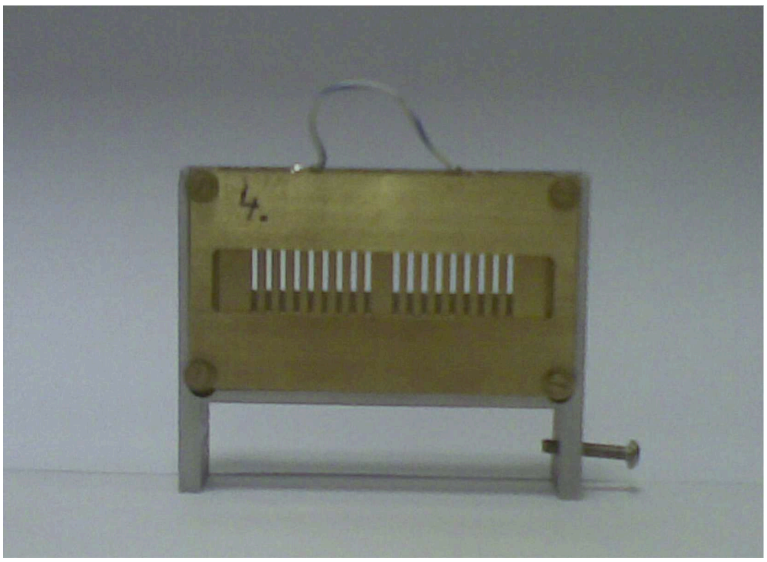

FIGURE 4.11: Picture of a PSDs holder. A grid with 18 slits is placed in front of the holder to perform the position calibration of the detector.

A typical plot of the set of position data versus energy, expressed in channels is shown in figure 4.12 for PSD3. The matrix, in most cases because of statistics and detector resolution, shows well separated lines corresponding to the various slits and almost vertical highly populated zones, representing tracks left by two-body reactions.

The angle of each slit with respect to the beam direction was measured by means of an optical system, making it possible to establish a correspondence between position signal from the PSDs and detection angle of the impinging particles.

In practice, the central angular position of each detector θ_0 was measured using a theodolite and the angular position corresponding to each slit was calculated by means of trigonometric identities.

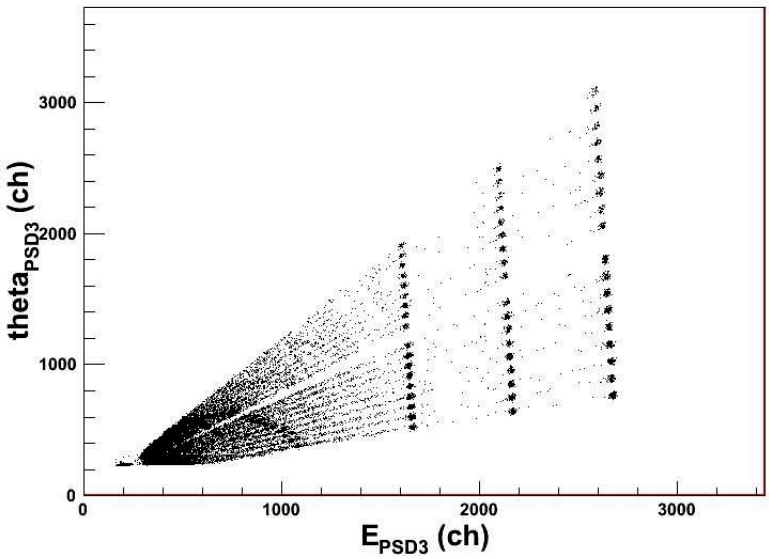

FIGURE 4.12: A typical position-energy two-dimension matrix of a PSD. Both energy and position signals are expressed in channels.

For the reasons pointed out in the previous section and as it is clear from figure 4.12, the position signal for each particle is a linear function of its energy, then the linear position of the particle hitting the detector can be derived by inverting the expression 4.8 and introducing the variable:

$$x_i = \frac{P - P_0}{E - E_0} \tag{4.9}$$

where x is the linear position on the detector in arbitrary units; P and E are the position and energy signals and E_0 and P_0 are constants determined by using a fit for all slits, taking into account the fact that the P and E signals are processed by different electronic chains.

At this point, it is possible to obtain the relation linking each x to the measured angle of corresponding slit:

$$\theta = \theta_0 + \left(\frac{180^\circ}{\pi}\right) arctan[c_1(x_i - x_0) + c_2(x_i - x_0))^2] \tag{4.10}$$

the coefficients c_1, c_2 and x_0 are the results of the best fit performed among all slits, while θ_0 represents detector central angle.

Besides the known correction to divide out the energy dependence of the P detector output, a second correction is introduced to take into account possible or unexpected detector nonlinearities by means of the quadratic term in equation 4.10

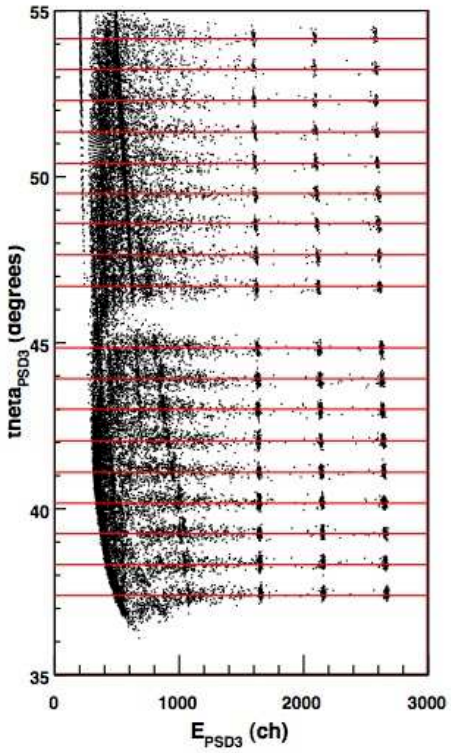

FIGURE 4.13: A typical matrix of a PSD after position calibration.

As a consequence, the matrix shown in figure 4.12 became made of straight horizontal lines, as in figure 4.13, with physical angles measured in degrees on the y-axis.

The described procedure must be repeated for every detector.

4.6.3 Energy calibration

Energy calibration was performed according to the usual procedure, that is by means of standard peaks of known energy, deriving the linear relation that links the energy signals digitalized by the ADC's to the particle energies.

In the present case detector calibration were performed using ^{16}O elastic and inelastic scattering in the energy range 30 - 60 MeV due to the interaction with

a gold and carbon targets for PSD1, PSD4 and IC calibration (by difference in the residual energy measured by PSD1 and PSD4 when the IC is empty and filled with butane at the working pressure).
The calibration of PSD2 and PSD3 were performed by means of the same ^{19}F beam, by detecting the α particles from the ^{19}F(p,α)^{16}O reaction induced onto a CD_2 target, performed at 55 MeV. A standard three-peak α-source (^{239}Pu, ^{241}Am, and ^{244}Cm) will also be needed to calibrate PSD2 and PSD3 at low energies.
In detail, in order to perform the energy calibration, the following calibration points were used:

1. ^{16}O beam Au 80μ/cm^2 (E= 60, 50, 40, 30 MeV)
2. ^{16}O beam C 28μ/cm^2 (E= 60, 50, 40, 30 MeV)
3. ^{19}F beam CD_2 95μ/cm^2 E= 55 MeV
4. three-peak α source

In this way calibrations are performed with the same particles we are interested in, improving the accuracy of the calibration procedure.

The ionization chamber was evacuate during calibrations, thus reducing angular and energy straggling of the scattered particles. At the end the IC was calibrated in energy by measuring the energy difference between scattered nuclei when the ionization chambers was evacuated and filled with 50 mbar butane gas.

The total kinetic energy of the detected particles was reconstructed off-line, taking into account the energy loss in the target and in the entrance and exit windows of the ionization chamber and in the other dead layers. The energy associated with each calibration point was derived through kinematic calculations made by the analysis program LISE++ [132].
In the hypothesis that there is a relation of direct proportionality between the energy of the detected particle and the conversion from the ADC in the electronic chain used for the on-line acquisition, the behavior of such quantities can be described by the relation:

$$E_{MeV} = a + bE_{ch} \tag{4.11}$$

where E is the energy of the particle expressed in MeV.
An angle dependent correction is introduced for taking into account detector non-linearities. Thus, the adopted calibration curve is given by:

$$E_{MeV} = a + bE_{ch}[1 + c_3(\theta - \theta_0) + c_4(\theta - \theta_0)^2] \tag{4.12}$$

where a, b, c_3 and c_4 are fitting parameters.

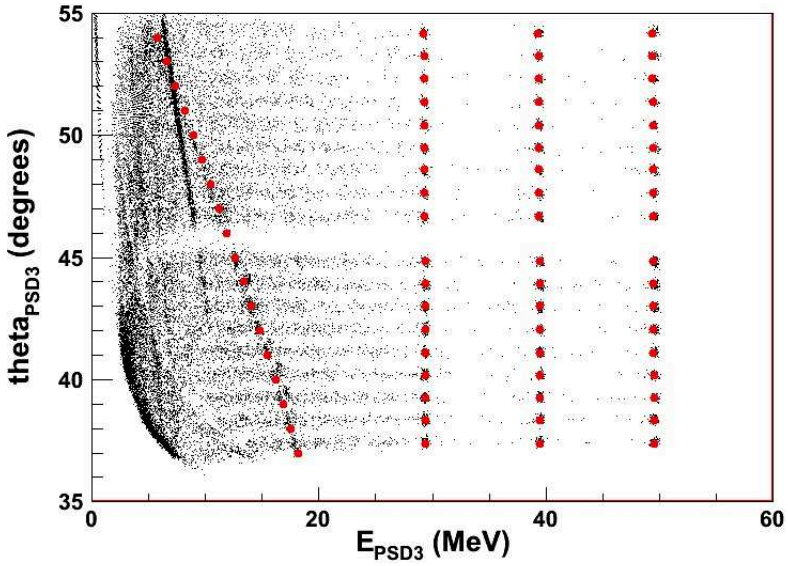

FIGURE 4.14: A typical matrix of a PSD after position and energy calibration.

Figure 4.14 shown a typical matrix of a calibrated detector. In order to have a check of the procedure, the theoretical points (red points) corresponding to the ^{16}O+Au elastic scattering and ^{16}O+d reaction, were plotted over the matrix. The good agreement confirms the accuracy of the performed calibration.
A similar procedure was adopted for the energy calibration of the ionization chamber, assuming as standard peaks the differences of the energies of scattered ^{16}O nuclei when the IC was empty and filled with 50 mbar butane, as measured by PSD1.

The energies measured by the PSD's are just residual energies because of the energy loss in the dead layers (i.e. target, windows). Thus energy reconstruction is needed to deduce the total kinetic energies of the reaction product just after the reaction taken place. This was accomplished off-line by determining the analytical function relating the energy loss to the residual energy (usually using one or more

parameters) for fixed material layers (half CD_2, alluminium, target, mylar foils in IC entrance and exit windows and detector dead layers) and impinging particles (see figures 4.15, 4.16).

In particular, it was conventionally assumed that reactions take place at half target.

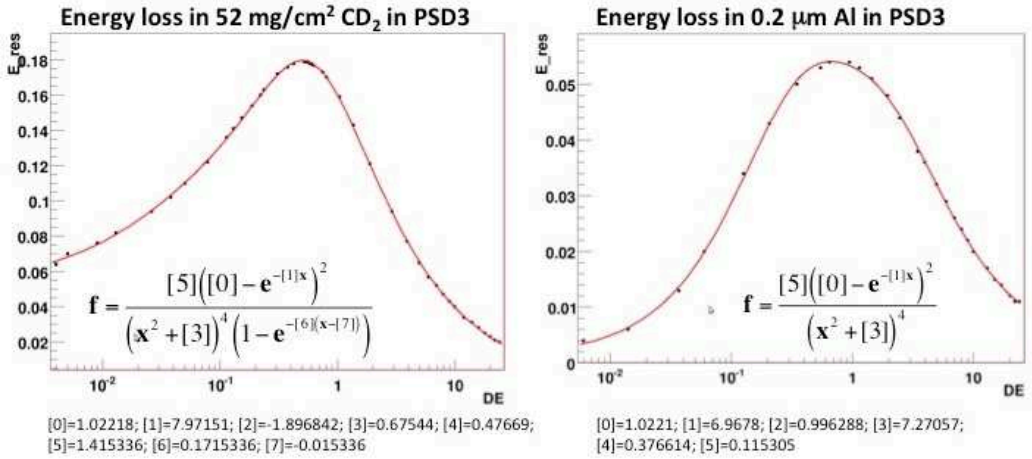

FIGURE 4.15: Energy loss function when a α particle passes through the aluminium dead layer of PSD2 (thickness = 0.2μm) and the half target. The analytic expression with all parameters is also shown. This is angular independent, so that it is the same for PSD2.

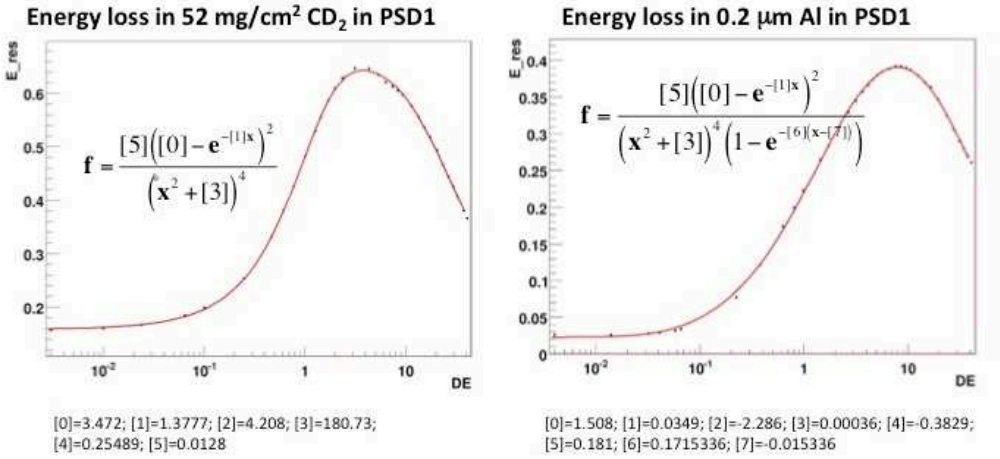

FIGURE 4.16: Energy loss function when a ^{16}O particle passes through the aluminium dead layer of PSD1 (thickness = 0.2μm) and the half target. The analytic expression with all parameters is also shown. This is angular independent, so that it is the same for PSD4.

Chapter 5

Data Analysis

5.1 Data analysis: Selection of the reaction channel

After energy and position detector calibration, the ^{2}H(^{19}F,α_0^{16}O)n channel has been selected by gating on the ΔE-E spectra. In fact, several different reactions can be induced on the same target owing to the presence of contaminants or several open channels. These parasitic reactions might introduce background that has to be identified and removed.
The 2 $\rightarrow$ 3 reactions allow for a number of kinematic tests suited to disentangle the A+a $\rightarrow$ c+C+s channel from others, which complement the standard particle identification approaches, such as the ΔE-E tecnique.
Since both the angle of emission and the kinetic energy of two of the three outgoing particles are detected and these lay on the same plane as the impinging nucleus, the Q-value spectrum for the coincidence events can be deduced and comparated with the theoretical value, calculated taking the mass of the undetected particle from the energy-momentum plot, as discussed in the next section [20].

5.1.1 Selection of the ^{2}H(^{19}F,α_0^{16}O)n channel

Since different reactions can be induced by the ^{19}F beam on the measurement target, the reaction channel selection is mandatory.

This is accomplished first through a selection of the oxygen locus with the standard ΔE-E technique.
The general idea behind the method is that using two detectors of known thickness, a particle entering them at a known angle θ will deposit energy ΔE in the top thin detector and energy E' in the bottom detector (which has a thickness large enough to stop the incident particles). From the measurement of these energies is possible to discriminate the different nuclear species in Z.

The expression of the average energy loss per unit length of charged particles other than electrons is known as the Bethe-Bloch equation [133]. If z is the charge of the particle, v its velocity, Z the atomic number of the material and A its atomic mass, the derivative dE/dx (energy loss per unit pathlength) can be approximated by the quantity:

$$-\frac{dE}{dx} \propto \frac{Z}{A}\frac{z^2}{v^2} \tag{5.1}$$

The total particle energy is approximated by E', the energy deposited in the bottom detector. This is a reasonable assumption, as it has been found that charged particles tend to lose most of their energy near the end of their range. For non-relativistic energy particles:

$$v^2 \propto \frac{2E}{m} \tag{5.2}$$

and therefore:

$$-\frac{dE}{dx} \propto \frac{Z}{A}\frac{mz^2}{2E} \tag{5.3}$$

this is sufficient in principle to uniquely identify the particle, as z^2m is unique for every nucleus we investigate. When a number of such events are collected, ΔE vs E' data will lie approximately along hyperbolas of constant z^2m.

Figure 5.1 displays the particle-identification two-dimensional spectrum provided by telescope A, where the different reaction products are well distinguished in Z but not in A.

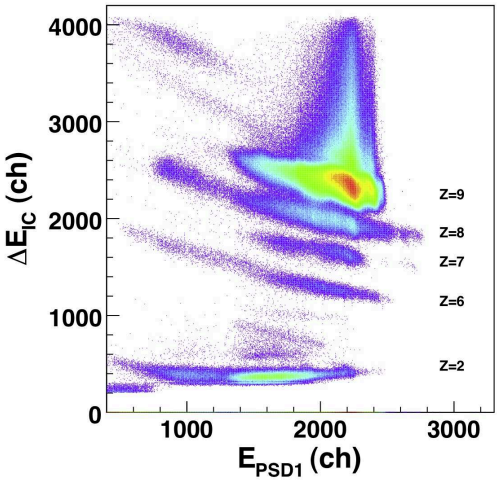

FIGURE 5.1: Particle ID with the standard ΔE-E technique.

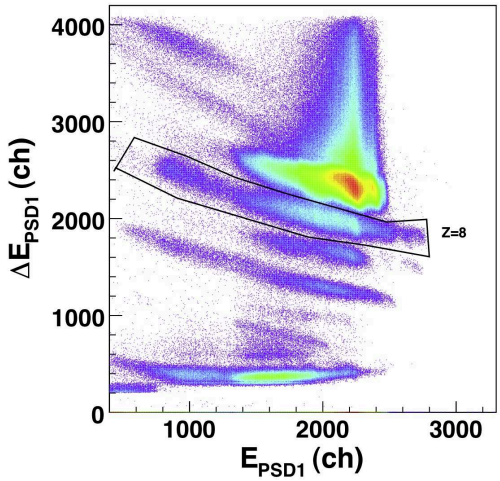

FIGURE 5.2: Graphical cut in the oxygen locus.

This figure shows that the contribution from scattered ^{19}F beam particles (Z=9) is clearly separated from the oxygen locus (Z=8).

In detail, the channel selection procedure begins with the separation of the oxygen locus in the ΔE-E two-dimensional plot by means of a graphical cut.
The graphical cut shown in figure 5.2 allows to select the events belonging to the locus of oxygen nuclei on the ΔE-E spectrum from the two telescopes. Only these are taken into account in the further analysis.

A further kinematic selection of the reaction channel is required because ^{16}O ejectiles are not resolved from ^{17}O nuclei in telescope, due to the quite poor energy resolution of the ionization chamber. The same is true for the α particles which cannot be separated from other reaction product in PSD2 and PSD3, these one having no ΔE detectors in front of them. In addition, neutrons is not detected, its energy and angle of emission being deduced event by event from three-body reaction kinematics. Therefore after oxygen identification and the assumption of mass number A=4 for the other particle detected in the same coincidence event for total energy reconstruction, the loci of events in E_{PSD1} vs. E_{PSD2} and the symmetric one two-dimensional plots are deduced and comparated with a Monte Carlo simulation fro the ^{2}H(^{19}F, $\alpha_0{}^{16}$O)n reaction channel.

It is well known that particles from a reactions with three nuclei in the exit channel have kinetic energies that are correlated by energy and momentum conservation equations. Therefore, E_{PSD1} vs E_{PSD2} and E_{PSD3} vs E_{PSD4} correlation plots were

drawn for those events belonging to the oxygen locus in figure 5.2. As an example, the E_{PSD1} vs E_{PSD2} energy correlation plot is given in figure 5.3. From this figure it turns out that several reaction channels contribute in the explored phase space region.

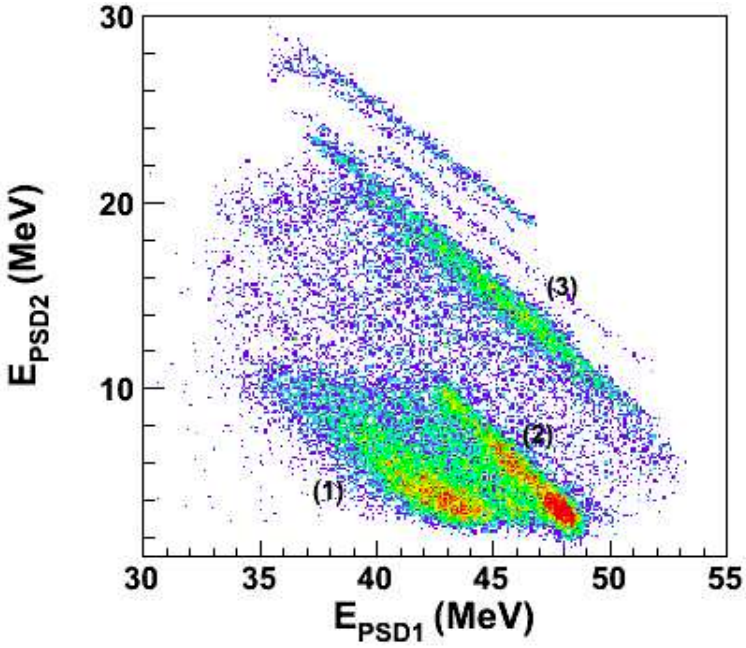

FIGURE 5.3: Kinematic locus from the PSD1-2 coincidence with selection of oxygen nuclei (Z = 8) on the ΔE - E two-dimensional spectrum in figure 5.2. 1 and 2 mark two loci corresponding to two-body background reactions.

In fact, three different kinematic loci show up in the picture. The events corresponding to the ^{2}H(^{19}F, α_0 ^{16}O)n TH reaction were singled out by comparison with a Monte Carlo simulation of that process, taking into account detection thresholds, energy losses and the kinematics of the TH reaction. The two additional spots located in the lower part of figure 5.3 marked with 1 and 2, correspond to binary reactions that constitute an easily removable background to the TH reaction.
From its analysis (1) is recognized as the locus of the ^{2}H(^{19}F, α_0 ^{16}O)n reaction while (2) and (3) are attributable to binary reactions which present an oxygen in the exit channel:

1. ^{19}F(^{12}C, ^{14}N)^{17}O
2. ^{19}F(^{12}C, ^{15}N)^{16}O
3. ^{2}H(^{19}F, α_0 ^{16}O)n

Since both the angle of emission and the kinetic energy of two of the three outgoing particles are detected and these lay on the same plane as the impinging nucleus, the Q-value spectrum for the coincidence events can be deduced and compared with the theoretical value, calculated taking the mass of the undetected particle from the energy-momentum plot, as discussed in [20].
The Q-value spectra for the two coincidences are calculated for the selected events by imposing energy balance for the three-body reaction.

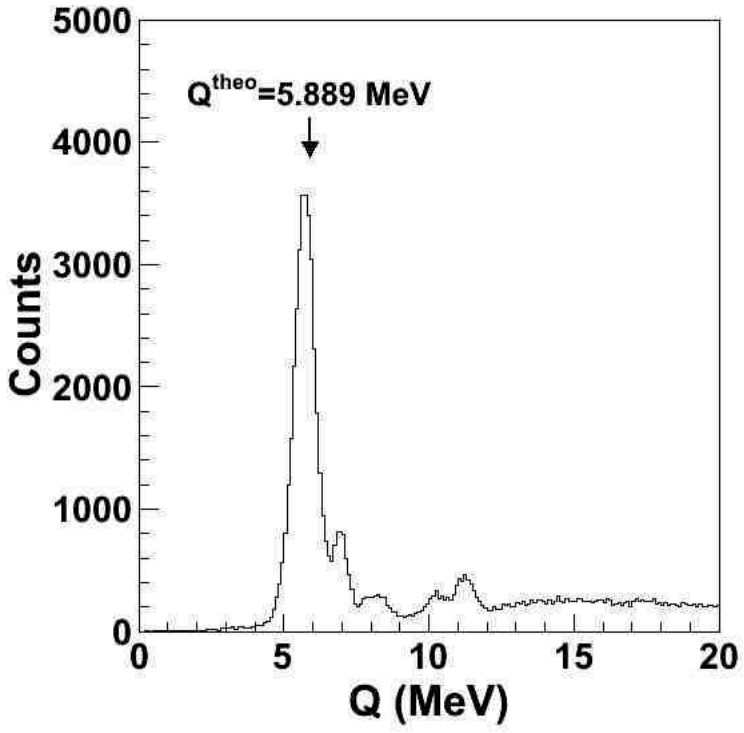

FIGURE 5.4: Reconstructed Q-value spectrum fro the coincidence PSD1-PSD2.

In figure 5.4 the Q-value spectrum is reported, showing several peaks that confirms the presence of contributions from background reactions on CD_2 target.

In the present experiment, only two of the three emitted particles were detected. This leaves the system underdetermined due to the overlapping of different kinematic loci in the same phase-space region, corresponding to reactions having different undetected particles. To identify the mass of the undetected particle s, the procedure discussed by Costanzo et al. (1990) [20] was applied on the events extracted with the procedure followed until now.
Since its momentum is deduced from the energies and emission angles of particles c and C by applying the momentum conservation equation, the variable $x = \frac{p_s^2}{2u}$ is

independent of the mass of the undetected fragment s (u being the unit mass in a.m.u.). If we define:

$$y = E_{beam} - E_c - E_C \qquad and \qquad x = \frac{p_s^2}{2u} \tag{5.4a, b}$$

the energy conservation equation can be cast in the form:

$$y = \frac{1}{A_s}x - Q_{2\to 3} \tag{5.5}$$

thus the mass of particle s can be inferred by fitting the line that best reproduces the experimental data. Therefore, this test allows for a comparison of the expected locus (a straight line) with the experimental one, and it establishes the mass of s with no need of a measurement. Indeed, events from reactions where a bad identification of the detected ejectiles is carried out do not gather along a straight line as equation 5.5 does not apply.

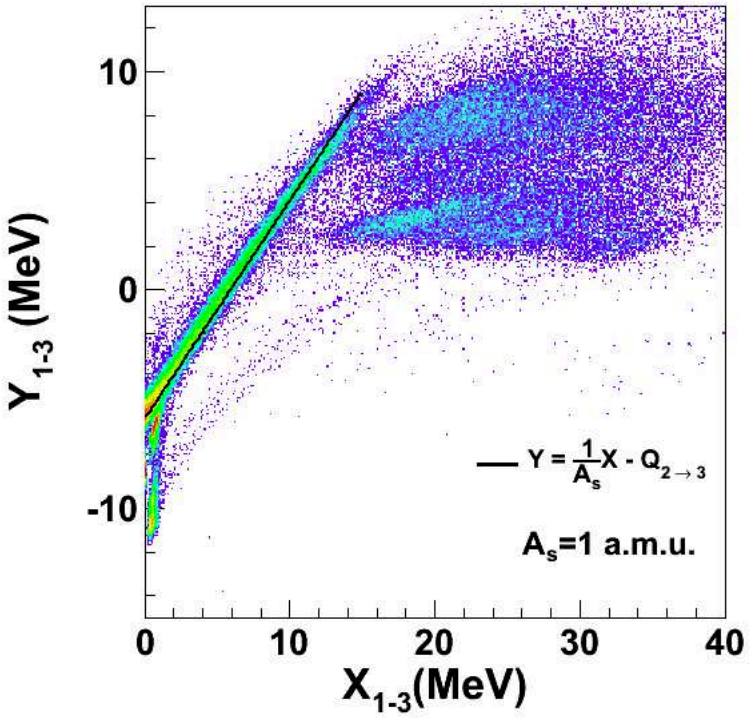

FIGURE 5.5: Identification of particle s according to the procedure of [20], applied to the PSD3-PSD4 coincidences.

In this case, in order to establish whether mass 1 assumption for the third particles is accurate, if the variable y = $E_{beam} - E_c - E_C$ is plotted as a function of x= $\frac{p_s^2}{2u}$ the events corresponding to the ^{2}H(^{19}F, α_0^{16}O)n reaction should gather around the straight line of equation:

$$y = x - 5.889 \tag{5.6}$$

the unity slope being due to the A_s=1. As figure 5.5 clearly displays the slope and the intercept confirm that the locus of the ^{2}H(^{19}F, α_0^{16}O)n three-body reaction is well reproduced and it is can be easily disentangled from the other as they are well separated in figure 5.3.
Indeed, to rule out these additional channels contributing to the experimental kinematical loci, a graphical cut was introduced in the figure 5.5 in order to remove the contaminant events, as shown in figure 5.6.

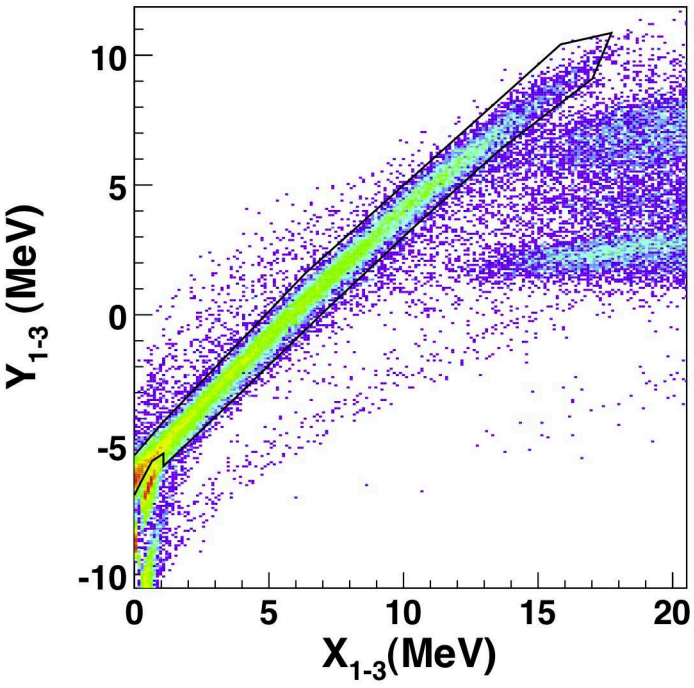

FIGURE 5.6: The graphical cut introduced to single out the background events.

In the subsequent analysis only these events are retained.
The resulting kinematic loci of the three-body reaction for these events is reportes in figure 5.7.

Clearly, no additional channels contribute to the experimental kinematic locus.

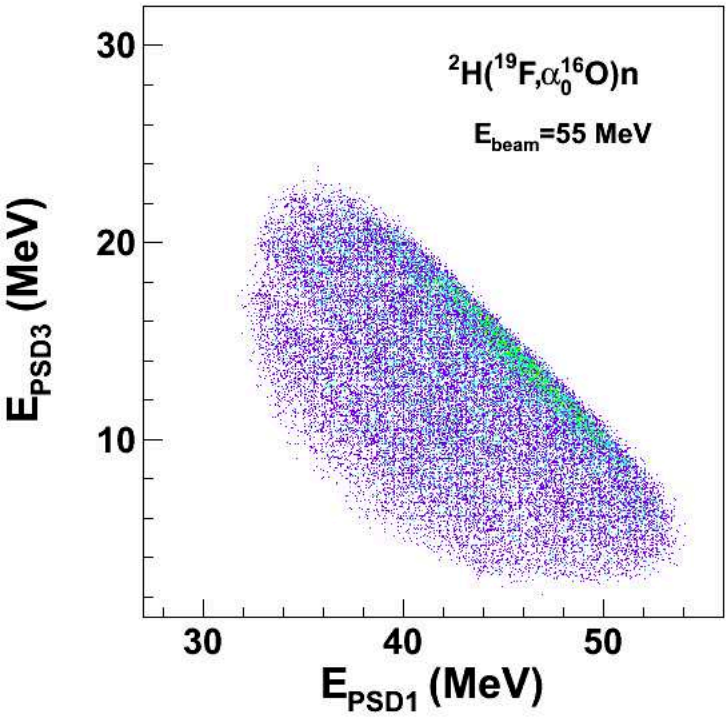

FIGURE 5.7: Kinematic locus of the ^{2}H(^{19}F, $\alpha_0{}^{16}$O)n reaction channel.

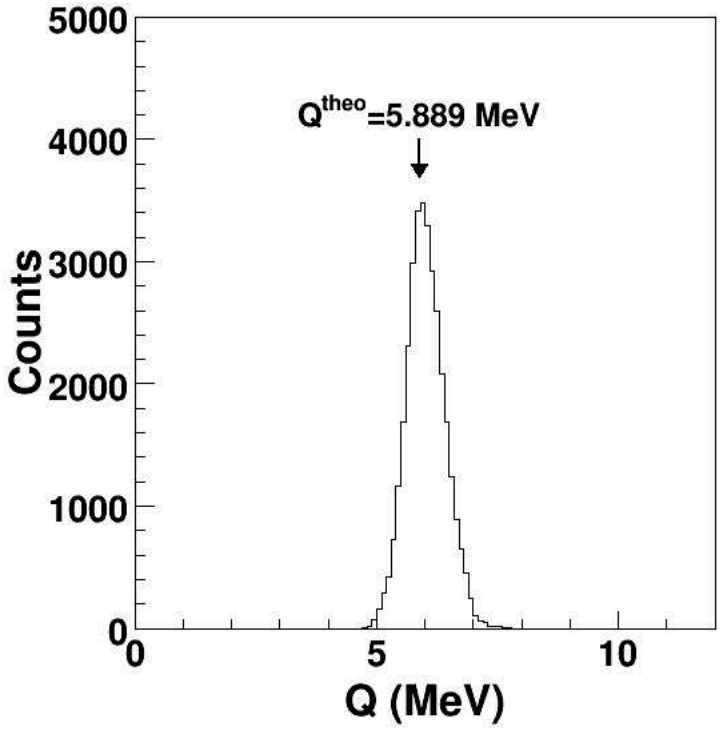

FIGURE 5.8: Q-value from the PSD1-2 coincidence, obtained by singling out the spurious contributions observed in figure 5.3.

This result was supported by the experimental Q-value spectrum where a single peak corresponding to the ^{2}H(^{19}F, α_0^{16}O)n process is apparent, centered at an energy of about Q_{3-body}=5.889 MeV.
The good agreement between the experimental and the theoretical Q-values (indicated by an arrow in figure 5.8) confirms not only the identification of the reaction channel but also the accuracy of the performed calibration. The presence of a single and symmetric peak, centered at the expected Q-value, rule out the occurrence of significant systematic errors.
Similar results are deduced from the other cuple.
The result of figures 5.7 and 5.8 make us confident on the identification of the three-body reaction channel. Thus, in the following, data analysis is restricted to such events.

Once the event corresponding to the ^{2}H(^{19}F, α_0^{16}O)n reaction has been disentangled from the other, by equating the Q-value to the theoretical one (because of the good agreement between the two) the kinematic variables such as the relative energies as well as the neutron momentum can be evaluated from just three experimentally measured variables.
These quantities are chosen with the aim of reducing the uncertainties on the calculated ones: for this reason the measured ^{16}O energy is neglected in the further data reduction because of the energy straggling due to the presence of the ionization chamber. This procedure is possible since the performed experiment was kinematically complete, that is all kinematic information can be deduced from the measured quantities [20].

5.2 Data analysis: Selection of the mechanism

As extensively discussed in the previous chapters, the main idea of the THM is to extract the astrophysical two-body cross-section for an astrophysically relevant reaction by measuring the QF-contribution of a suitable three-body reaction. From the experimental point of view, this kind of solution needs some tests, each one related to the behavior of the three-body cross section with the momentum values of the spectator in the exit channel.

Thus, after the selection of the α_0+^{16}O+n exit channel, the following step in data analysis is to establish whether in the selected experimental kinematic regions the contribution of the QF process to overall α_0+^{16}O coincidence yield is evident and well separated from others. As already mentioned, since the analysis of the experimental results is in general complicated by the presence of other reaction mechanism feeding the same particles in the final state, such as SD and DBU, an exhaustive study of those reaction mechanism is a necessary step to disentangle the QF from other background process (see figures 4.6 for SD mechanism ending up in the same α_0+^{16}O+n exit channel.)

5.2.1 Study of the SD channels

In order to study the SD process which take place through the formation of the ^{5}He and ^{17}O compound nuclei, such that the neutron cannot be regarded as a spectator in the interaction between the participant proton and the impinging ^{19}F nucleus, the two-dimensional plots showing the relative energies for any two of the three final particles are derived.
In particular the correlation plots for the relative energies of the particles in the exit channel $E_{^{16}O-n}$ vs. $E_{\alpha-^{16}O}$ and $E_{\alpha-n}$ vs. $E_{\alpha-^{16}O}$ are reported in figures 5.9 for the PSD3-PSD4 detector coincidence.

The relative energy spectra represent the excitation energy spectra for ^{20}Ne, ^{17}O and ^{5}He nuclei above the threshold for alfa or neutron decay.
The examination of this plots allows to understand quite easily if peaks in the three-body cross section have to be attributed to the decay of ^{20}Ne or the SD of ^{5}He and ^{17}O excited states. Indeed, if compound nuclei form later decaying to the observed final state, peaks should appear that correspond to levels populated following the interaction.

For example, if horizontal loci in figure 5.9 show up, populating a region of constant $E_{\alpha-n}$ or constant $E_{^{17}O-n}$, this means that an excited state of ^{5}He or ^{17}O respectively has been populated in the process. Similarly, if a locus is present of constant $E_{^{16}O-\alpha}$ relative-energy, then an excited state of ^{20}Ne has been fed.

From the examination of figure 5.9 very clear vertical loci appear in the $E_{^{16}O-n}$ vs. $E_{\alpha-^{16}O}$ relative energy two-dimensional plots, corresponding to excited states

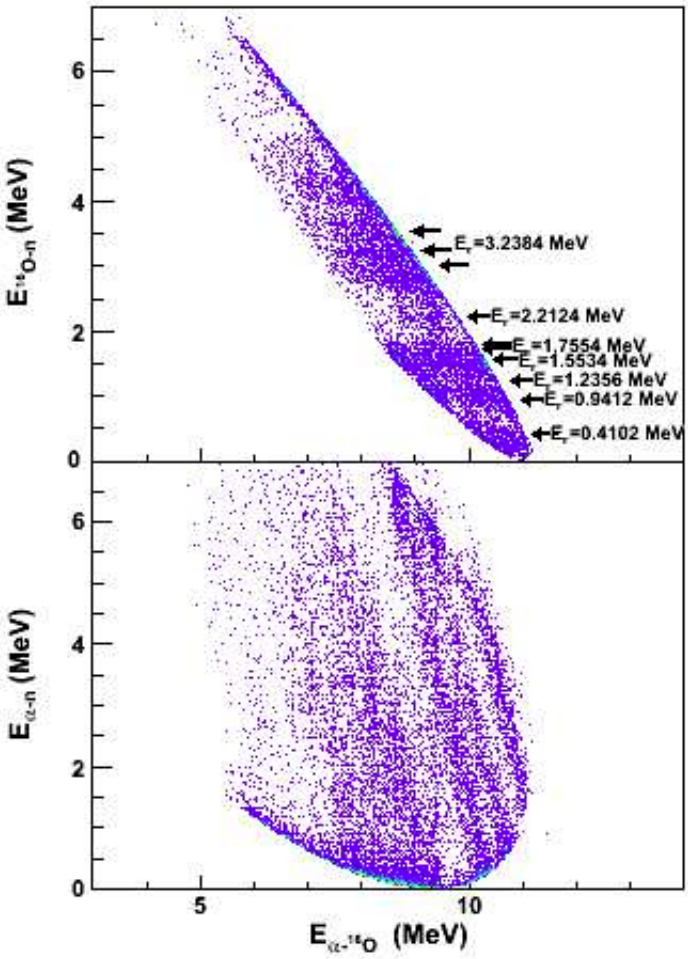

FIGURE 5.9: Energy correlation two-dimensional spectra. $E_{^{16}O-n}$, $E_{\alpha-^{16}O}$, and $E_{\alpha-n}$ are the ^{16}O-n, ^{16}O-α, and α-n relative energies, respectively. Horizontal loci in the lower panel correspond to ^{17}O excited states, while the vertical one correspond to ^{20}Ne excited states

of ^{20}Ne [24]. An additional contribution to the three-body cross section due to the sequential decays of the ^{17}O excited states [134] is also apparent, corresponding to the horizontal loci in figure 5.9 panel a).

Such sequential processes, corresponding to the simplified scheme in fig.4.6, give a negligible contribution to the coincidence yield in the astrophysically relevant energy region below MeV (from equation 4.6 one can deduce that zero energy in the ^{19}F(p,α_0)^{16}O channel corresponds to 8.11 MeV in the ^{16}O-α relative energy spectrum), as clearly shown in figure 5.10 where the grey box emphasizes the energy range of astrophysical interest.

Finally, no horizontal loci appear in the panel c) of figure 4.6 ruling out any contribution from ^{5}He sequential decay.

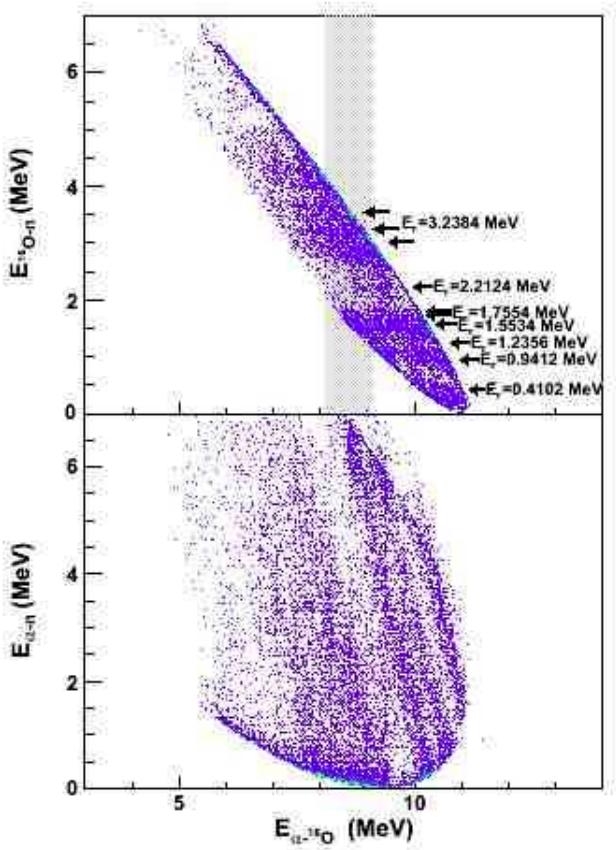

FIGURE 5.10: Energy correlation two-dimensional spectra. $E_{^{16}O-n}$, $E_{\alpha-^{16}O}$, and $E_{\alpha-n}$ are the ^{16}O-n, ^{16}O-α, and α-n relative energies, respectively. The grey box emphasizes the energy range of astrophysical interest.

Of course, the occurrence of sequential mechanisms in the α - ^{16}O channel cannot be ruled out by studying the relative energy correlation plots only, because the decay of ^{20}Ne compound system can take place both via a SD or a QF process and additional tests are required.

5.2.2 Data as a function of the neutron momentum

A preliminary but simple way to discriminate between SD and QF events is through the study of the correlation plot of the $E_{\alpha-^{16}O}$ relative energy and of the neutron momentum p_s.

As mentioned before, the QF-mechanism is connected with the behavior of the undetected third particle in the exit channel. In the present case, if it is possible to find a strong dependence of the three-body cross section from its momentum, the undetected neutron can be assumed as spectator.

Figure 5.11 shows the α - ^{16}O relative energy as a function of the neutron momentum p_s in a two-dimensional plot. The horizontal lines correspond to the excited states of the ^{20}Ne, as discussed in the previous section. In particular the kinematic loci extending to low p_s in the energy range o<$E_{c.m.}$<1 MeV (indicated in figure with black lines) constituting the most relevant for astrophysical applications.

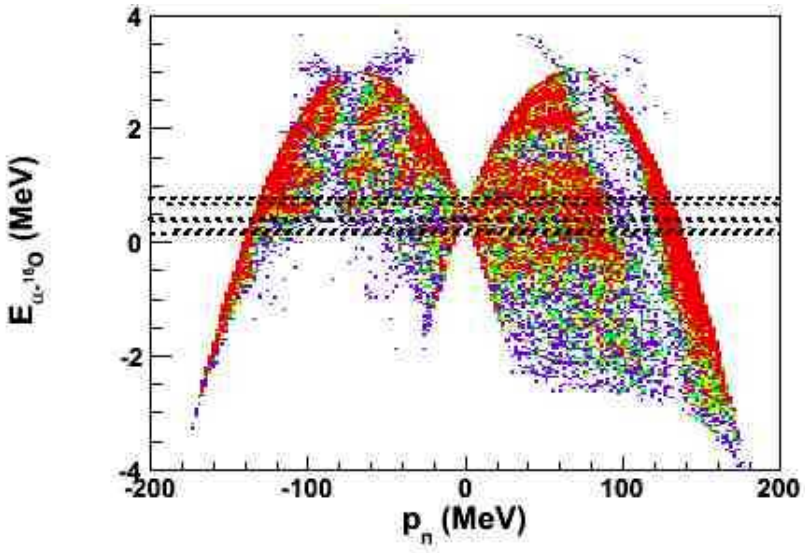

FIGURE 5.11: $E_{\alpha-^{16}O}$ relative energy as a function of the neutron momentum p_s.

At higher p_s the presence of the ^{17}O levels is clearly visible, but their contribution in the astrophysically relevant energy region is very small, since the decays from ^{17}O intermediate states leave the final neutron with a momentum larger then about 40 MeV/c.

The levels of interest are characterized by a larger cross section as p_s approaches zero: this is a clear signature of the QF nature of the excited ^{20}Ne levels if phase space effects turn out to be negligible. Anyway this result might be not a sufficient condition, since the discussed correlation can be partially dependent on phase-space population effects, regardless of its SD or QF origin. Additional tests are thus required to establish the presence of the QF contribution.

5.2.3 Study of $E_{c.m.}$ spectra for different p_s ranges

While ^{17}O states are formed only through sequential mechanism, the ^{20}Ne excited states can be populated via quasi-free mechanism or via sequential decay.

Indeed, an enhancement of the cross section close to zero neutron momentum is a necessary condition for the occurrence of the QF mechanism, marking the presence of a modulation of the TH cross section by the neutron momentum distribution inside the deuteron. This feature is expected for a QF reaction because the momentum distribution of the n - p system inside the deuteron has a maximum for $p_s = 0$ MeV/c.
Since the experimental range of the spectator particle momentum extends well beyond the interval where the QF contribution is supposed to be dominant, namely the full width at half maximum of the Hulthen momentum distribution (see the next section), a comparison of the coincidence yield for small p_s and larger p_s can be performed.

Thus, the coincidence yield spectra as a function of $E_{c.m.}$ was reconstructed for all coincidence events, for different neutron momentum ranges. $E_{c.m.}$, as defined in equ. 4.6, is the ^{19}F-p relative kinetic energy related to $E_{\alpha-^{16}O}$ relative energy by the energy conservation law:

$$E_{cm} = E_{^{19}F-p} = E_{\alpha-^{16}O} - Q_{2body} = E_{\alpha-^{16}O} - 8.11 MeV \tag{5.7}$$

Such spectra were divided by the kinematic factor in order to remove the pure kinematical effects due to the experimental phase-space selection. The dividing factor is evaluated by means of a Monte Carlo calculation in which no modulation coming from deuteron momentum distribution is introduced. In this way it is possible to study the momentum dependence of the excitation functions, as it shown in figure 5.12 for the PSD1-PSD2 coincidence.
In detail, these spectra, were obtained by selecting the $|p_s| < 20$ MeV/c (upper panel), $20 < |p_s| < 40$ MeV/c (middle panel), and $40 < |p_s| < 60$ MeV/c (lower panel) intervals of the neutron momentum p_s.

Such a picture clearly demonstrates that in the energy range of interest for astrophysics, around 0-0.5 MeV, the coincidence yield is much higher for $|p_s| < 20$

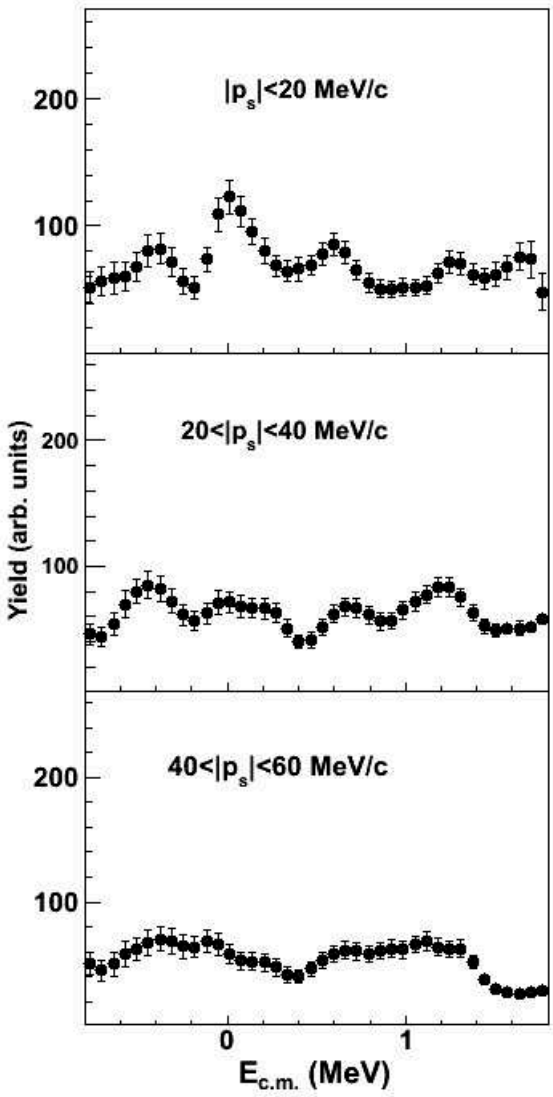

FIGURE 5.12: Normalized reaction yield for different p_s ranges. The reaction yield monotonically decreases moving to high p_s values, as expected for a QF reaction using deuteron as TH nucleus. This represent a first test of the occurrence of the QF mechanism in the ^{2}H(^{19}F, α_0 ^{16}O)n reaction.

MeV/c than what is obtained at larger p_s momenta. Indeed, at higher momenta ($20 < |p_s| < 40$ MeV/c and $40 < |p_s| < 60$ MeV/c) it drastically decreases and the resonance becomes barely visible compared to the background.

A very similar result is obtained for the PSD3-PSD4 coincidence events.

These data provide strong evidence of a clear correlation between coincidence yield and spectator neutron momentum p_s, which is a necessary condition for the occurrence of the QF reaction mechanism.

The previous discussion can be made more quantitative as the neutron momentum distribution inside the deuteron can be measured by means of the ^{2}H(^{19}F, α_0 ^{16}O)n QF reaction.

5.2.4 Study of the experimental momentum distribution

An observable very sensitive to the reaction mechanism is the shape of the experimental momentum distribution of the cluster s in the TH-nucleus a. Indeed, if the a+A $\rightarrow$ c+C+s reaction is direct and can be described by the diagram in figure 3.3, s should keep the same momentum as inside a before interaction with the impinging particle, thus the comparition of the experimental and theoretical momentum distributions can be used to disentangle the QF reaction mechanism from others.

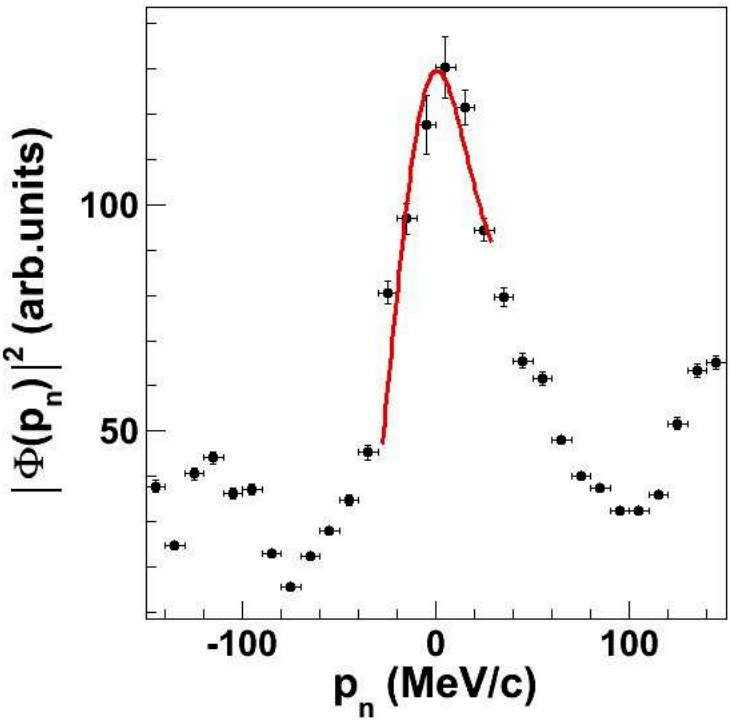

FIGURE 5.13: Experimental momentum distribution (full dots) compared with theoretical ones, given by the square of the Hulthen wave function in momentum space (black solid line) -40<p_s<20 MeV/c

The experimental p_s momentum distributions is given in arbitrary units by the equation:

$$|\phi(p_s)|^2 \propto \left[\frac{d^3\sigma}{d\Omega_\alpha d\Omega_{^{16}O} dE_{c.m.}}\right] [KF]^{-1} \tag{5.8}$$

and is reported in figure 5.13, error bars including only the statistical error.

It is compared with the expected theoretical one, given by the square of Fourier transform of the radial bound-state wave function for the x-s system in the PWIA approach. In the case of the deuteron, the theoretical distribution is given in terms of the square Hulthen wave function in momentum space:

$$|\Phi(p_s)|^2 = \frac{1}{\pi}\sqrt{\frac{ab(a+b)}{(a-b)^2}}\left[\frac{1}{a^2+p_s^2} - \frac{1}{b^2+p_s^2}\right] \tag{5.9}$$

with parameters a=0.2317 fm^{-1} and b = 1.202 fm^{-1} for the deuteron [130].

The square Hulthen function in momentum space superimposed onto the data only for -40<p_s<20 MeV/c range (red line), contains a single fitting parameter, the normalization constant fixed by the experimental maximum.

From figure 5.13 it is apparent that equation 5.9 accurately reproduces the shape of experimental data for -40<p_s<20 MeV/c.

The good agreement, within the error bars, between the experimental data and the theoretical Hulthen function for the p-n motion inside the deuteron represents a strong experimental evidence that the neutron acted as a spectator during the break-up occurred in the ^{2}H(^{19}F, α_0^{16}O)n reaction.

In particular, the experimental full-width at half-maximum (FWHM) is 61± 10 MeV/c, in good agreement with the theoretical value of 58 MeV/c.

Distortions should influence only the tails of the distribution, beyond the range of interest, corresponding to short n - p relative distances, as only the nuclear interaction can influence the p-^{19}F interaction [102].

Since the expression for the TH cross section derives from the application of the impulse approximation, good agreement is found if the momentum transfer, defined by the Galilean invariant equation [21].

$$q_t = \left(\frac{m_F}{m_A}\right)^{\frac{1}{2}} p_A - \left(\frac{m_A}{m_F}\right)^{\frac{1}{2}} p_F \tag{5.10}$$

is large enough to make distortions negligible.

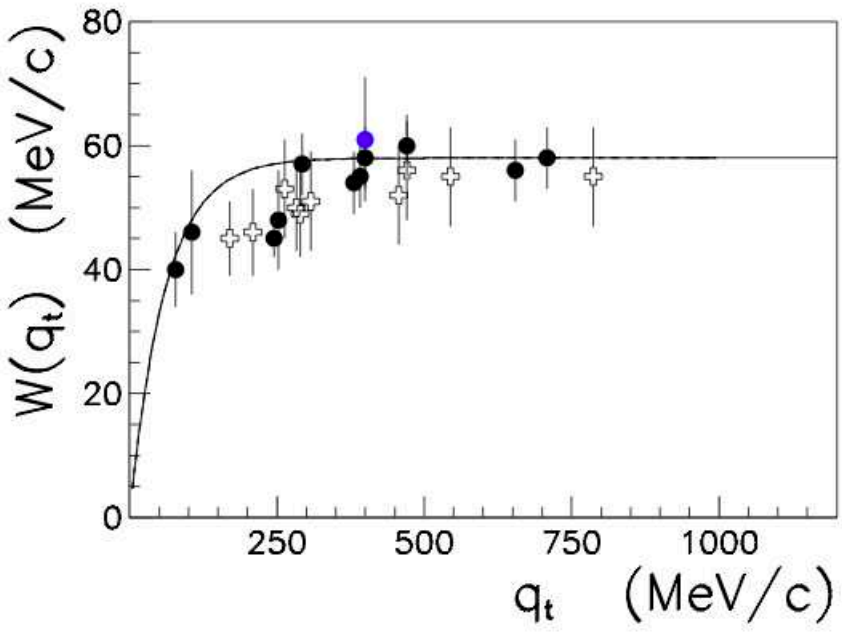

FIGURE 5.14: Behavior of FWHM for the p-n momentum distribution as a function of the transferred momentum q_t [21]. The blue point indicate the value obtained in this measurement. The FWHM is deduced from the experimental p-n momentum distribution, while the q_t value is calculated from the reaction kinematics.

In this case the incident ^{19}F energy is 55 MeV and the transferred momentum corresponding to the QF condition is 403 MeV/c, leading to an experimental FWHM that matches the value characterizing the Hulthen function, which can be ragarded as the asymptotic value achieved only for large transferred momenta. This is clearly presented in figure 5.14, where the trend of the experimentally measured FWHM of the deuteron momentum distribution as a function of the transferred momentum is displayed.

Therefore we can conclude that in the experimental kinematic regions the QF mechanism gives the main contribution to the ^{2}H(^{19}F, $\alpha_0{}^{16}$O)n three-body reaction, at least within the -40<p_s<20 MeV/c range.

5.2.5 Result of the selection

Instead the investigation of the relative energies and momentum distribution plots allows one to discriminate the sequential mechanism by introducing graphical selections which leave outside of the astrophysically relevant energy region the events corresponding to sequential decays from the intermediate compound nucleus. Thus only events with spectator momentum -40< p_s< 20 MeV/c were considered.

The effect of the selection of events satisfying the -40<p_s<20 MeV/c condition is shown in figure 5.15 for the $E_{^{16}O-n}$ and $E_{\alpha-n}$ relative energy spectra. Figure clearly show that no yield from sequential decay is present in the selected phase space region, so no SD levels contributes to the three-body cross-section in the astrophysically relevant energy region.

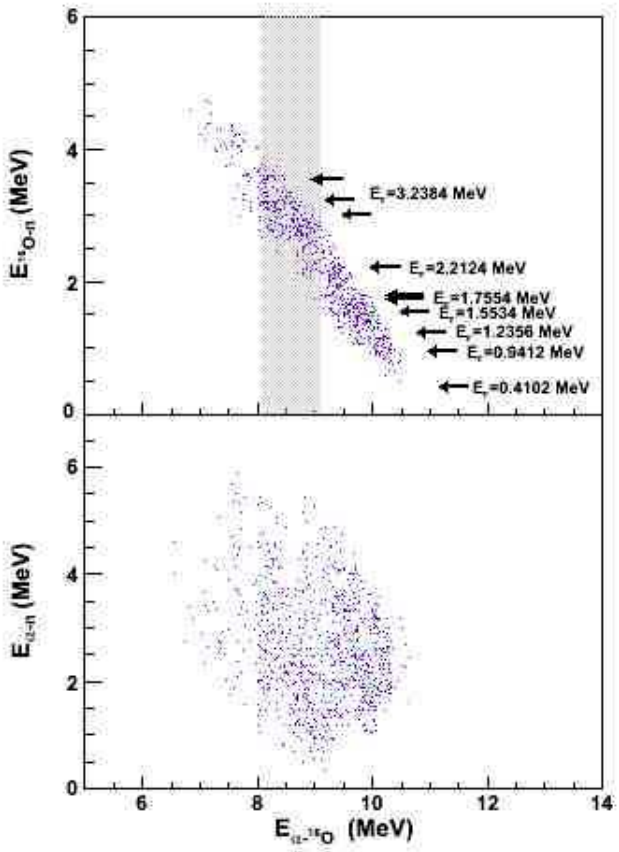

FIGURE 5.15: Energy correlation two-dimensional spectra. The momentum condition mentioned in the text is included.

This means on one hand that no significant contributions from contaminant SD processes enter the three-body cross section and on the other the PWIA provides an accurate description of the process, thanks to the high transferred momentum.

For these reasons, in the following analysis, only the phase-space region where -40<p_s<20 MeV/c is taken into account, allowing us to apply the PWIA in the following calculations without introducing significant systematic uncertainties. Together with the previous tests, the good agreement between the theoretical and experimental distributions makes us confident that the QF mechanism gives the main contribution to the ^{19}F+d reaction at an energy of 55 MeV in the experimental kinematical regions.

5.3 Extraction of the two-body cross-section

After the identification of the QF mechanism only events with spectator momentum -40< p_s < 20 MeV/c were considered. Since PWIA approach supplies the off-energy-shell two-body cross section, it is necessary to perform the appropriate validity tests on the indirect two-body cross section before extracting the low-energy cross section of astrophysical interest. In this phase, first the angular distribution test is performed and then the excitation function are deduced.

5.3.1 Angular distributions

A first test of validity of the THM approach is represented by the comparison between the indirectly extracted angular distributions and the direct behavior.

The relevant angle in order to get the indirect angular distributions, i.e. the emission angle for the alpha-particle in the α-^{16}O center of mass system, can be calculated according to the relation [108]:

$$\theta_{c.m.} = arccos\frac{(\vec{v}_{^{19}F} - \vec{v}_p)(\vec{v}_\alpha - \vec{v}_{^{16}O})}{|\vec{v}_p - \vec{v}_{^{19}F}||\vec{v}_\alpha - \vec{v}_{^{16}O}|} \tag{5.11}$$

These quantities can be calculated from their corresponding momenta in the laboratory system, where the momentum of the transferred particle (proton) is equal and opposite to that of neutron spectator, due to the quasi-free assumption [108]. The center-of-mass angular ranges in this experiment were about $\theta_{c.m.}$ = 86°-136° and $\theta_{c.m.}$ = 82°-130° for the PSD1-PSD2 and PSD3-PSD4 coincidence detectors respectively.

The general expression for the angular distribution of the fragments for the resonance reaction has been obtained by Blatt [135]. In the case of an isolated resonance with only one value of l_i, l_f , S_i, and S_f , it takes the form:

$$\begin{aligned}\frac{d\sigma}{d\Omega} =& K(-1)^{S_f - S_i} \\ & \times \sum_L (\vec{l_i})(\vec{l_f})(\vec{J_F})^2(-1)^L \begin{pmatrix} l_i & J_F & S_i \\ J_F & l_i & L \end{pmatrix} \\ & \times \langle l_i m_{li} l_i m_{li} | L M_L \rangle \begin{pmatrix} l_i & J_F & S_i \\ J_F & l_i & L \end{pmatrix} \\ & \times \langle l_f m_{lf} l_f m_{lf} | L M_L \rangle P_L(cos\theta_{c.m.})\end{aligned}$$

where:

- $\begin{pmatrix} l_i & J_F & S_i \\ J_F & l_i & L \end{pmatrix}$ and $\begin{pmatrix} l_i & J_F & S_i \\ J_F & l_i & L \end{pmatrix}$ are Wigner 6j-symbols;
- $\langle l_i m_{li} l_i m_{li} | L M_L \rangle$ and $\langle l_f m_{lf} l_f m_{lf} | L M_L \rangle$ Glebsch-Gordan coefficients;
- K a normalization constant, function of the $E_{c.m.}$.

The angular distributions test was performed for five different $\alpha - ^{16} O$ relative energy intervals between $E_{c.m.}$ = 0-900 keV, where the resonances reported in table 5.1 occur.

The result obtained is displayed in figure 5.16, were the different center of mass energies being marked for each picture. The angular distributions extracted are shown as red points, the direct data as black points and the theoretical ones as a line.

The error bars include both statistical and normalization errors (being determined by adjusting the indirect data to the trend of the direct ones).

In this case, the angular distributions of the final fragments coming from the $^{19}F(p,\alpha)^{16}O$ subreaction are extracted not to evaluate spin and parity of the low-laying resonances, but only to validate the THM approach.

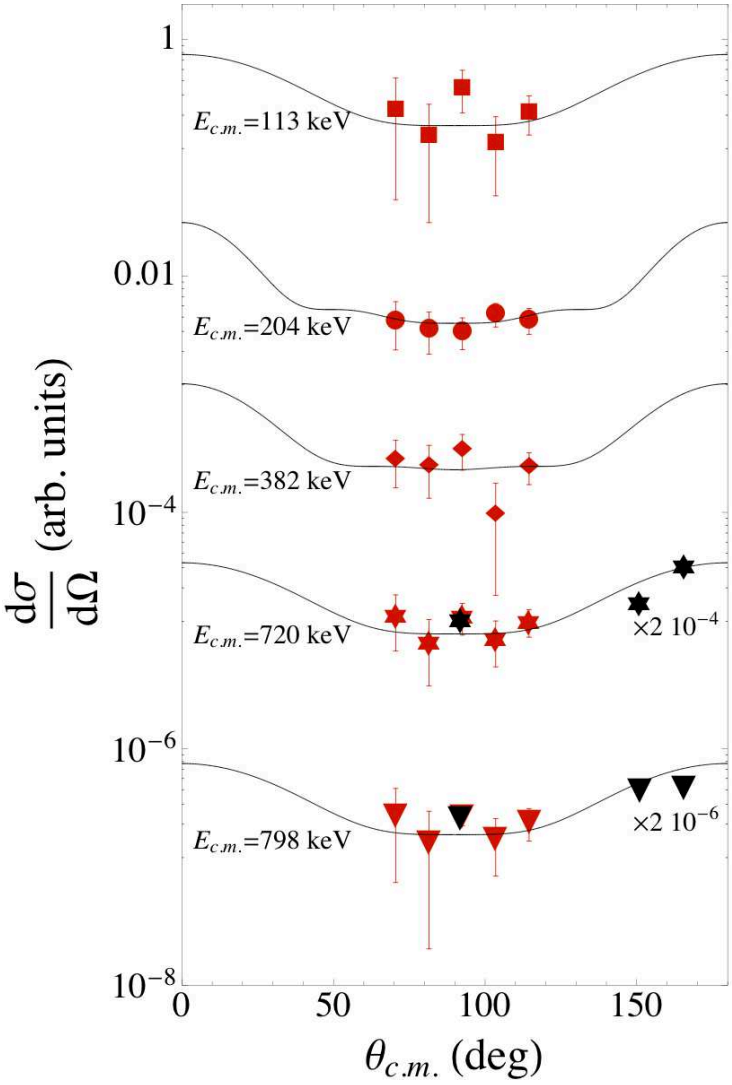

FIGURE 5.16: Example of angular distribution extracted at different $E_{c.m.}$ via the THM (red point) compared to the direct data(black point) [22] [23] and the theoretical ones (solid lines) calculated according to the equation 5.3.1.

The quite fair agreement between the two trends makes us confident on the validity of the IA.

5.3.2 Excitation function

The normalized coincidence yield for each coincidence is given in figures 5.17. It was obtained by dividing the selected coincidence yield by the product of the phase-space factor and of the p-n momentum distribution (see [136] and references therein).

$\mathbf{E}_{^{20}Ne}$ **(MeV)**	$\mathbf{E}_{c.m.}$ **(MeV)**	$\mathbf{J}^{\pi}$
12.957	0.113	2^+
13.048	0.2	4^+
13.222	0.374	0^+
13.224	0.376	1^-
13.226	0.378	3^-
13.529	0.681	2^+
13.586	0.738	2^+
13.642	0.794	0^+, 2^+

TABLE 5.1: ^{20}Ne excited states populated in the ^{19}F(p, α_0)^{16}O reaction [24]. The third column indicates the J_π values reported in literature.

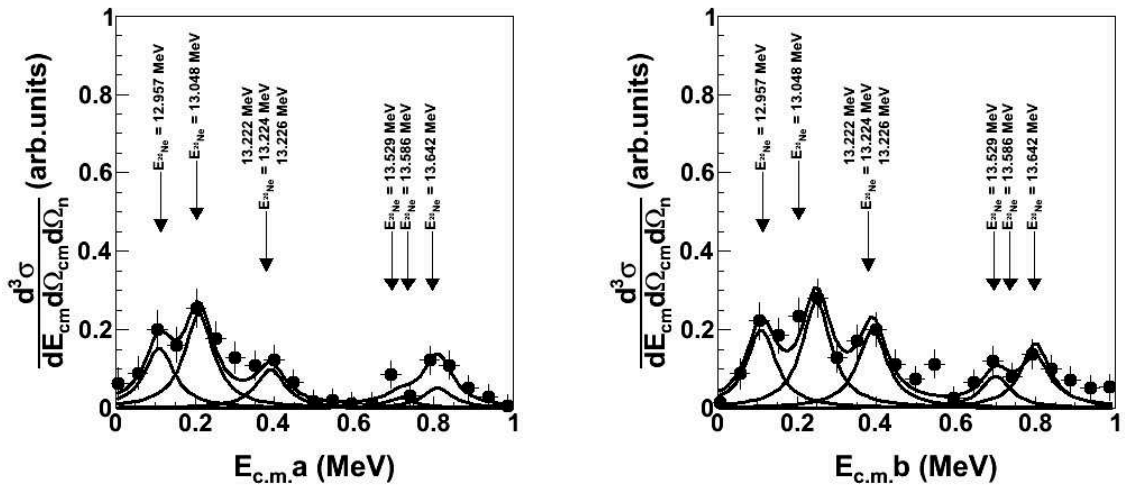

FIGURE 5.17: Normalized coincidence yield of the ^{19}F(p, α_0)^{16}O reaction for the two coincidences. The black circles are the experimental data, with the horizontal error bars defining the p - ^{19}F-relative-energy binning used in data reduction and the vertical ones the statistical uncertainties. The black line are the contribution of the resonances and multi-Gaussian fitting of the experimental data.

The experimental data clearly show the presence of five resonance groups corresponding to ^{20}Ne states at 12.957; 13.048 MeV; 13.222, 13.224, and 13.226 MeV; and 13.529, 13.586 MeV and 13.642 MeV (see table 5.1) which correspond to the 0.113 MeV; 0.2 MeV; 0.374, 0.376, 0.378 MeV; 0.681, 0.738 MeV and 0.794 MeV excited levels in the E_{cm} (see figure 5.18), as schematized in the table 5.1.

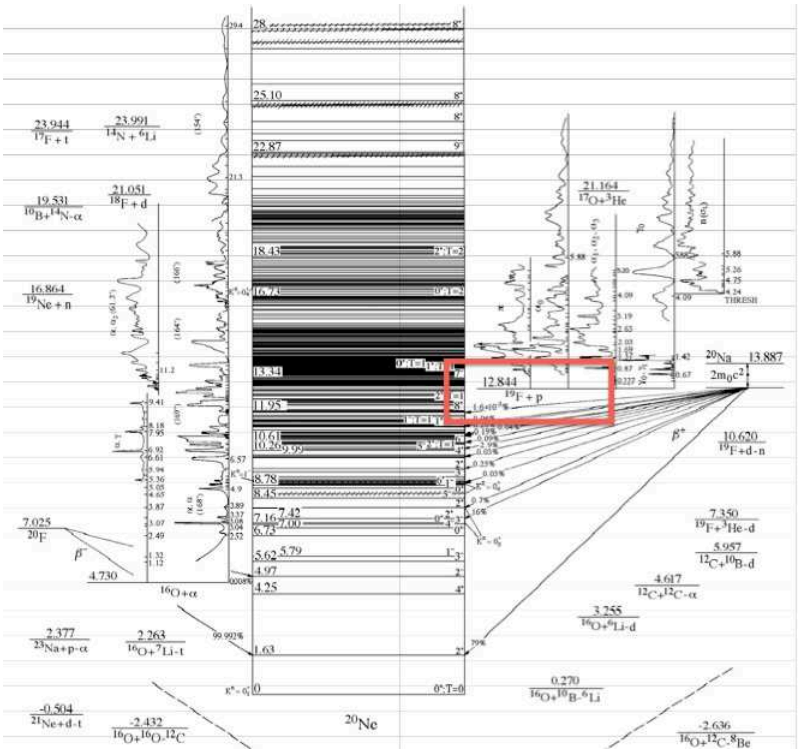

FIGURE 5.18: Typical scheme of the possible excited states of ^{20}Ne [24]. The red box underlines the energetic region reached with the present experiment.

The normalized yield was fitted simultaneously with five Gaussian curves to separate the resonance contributions. The same fitting procedure has been repeated for each coincidence.

A single Gaussian was used in the cases of the 13.222, 13.224, and 13.226 MeV levels could not be resolved in the experimental E_{cm} spectrum and in the 13.529 and 13.586 MeV levels because have the same spin parity (see table 5.2).

In the fit, the resonance energies were kept fixed at their known values, while the FWHM of each resonance was left as a free parameters.

$\mathbf{E}_{^{20}Ne}$ **(MeV)**	$\mathbf{S}_i$ **(MeV)**	$\mathbf{L}_i$	$\mathbf{J}^\pi$
12.957	0^+	2	2^+
	1^+	2	2^+
13.048	0	4	4^+
	1^+	4	4^+
13.222	0^+	0	0^+
13.224	0^+	1	1^-
	1^+	1	1^-
13.226	0	3	3^-
	1	3	3^-
13.529	0^+	2	2^+
	1^+	2	2^+
13.586	0^+	2	2^+
	1^+	2	2^+
13.642	0^+	2	2^+
	1^+	2	2^+
	(0^+	0	0^+)

TABLE 5.2: ^{20}Ne excited states populated in the ^{19}F(p, α_0)^{16}O reaction [24]. The column indicates the possible S_i, L_i and J_π values.

5.4 The two-body cross-section

Assuming non-interfering resonances, the TH cross section is obtained in the plane-wave (PW) approximation by equation 3.36. In the integration, the $J^\pi = 3^-$ E_R = 13.226 MeV state in ^{20}Ne was assumed to dominate over the two neighbor resonances, because of the $2J^\pi$ +1 enhancement factor in the formula.
The resulting reaction cross section for each coincidence are shown in figures 5.19.

The total TH cross section $\frac{d2\sigma}{dE_{c.m.}d\Omega n}$ is displayed in Figure 5.20 as full dots. Statistical uncertainties and those due to angular-distribution integration are given, as the other source of uncertainty, namely background subtraction, contributes by less than 20% to the total error budget. The horizontal error bars give the width of the p -^{19}F relative-energy bins used in the data analysis.

Figure 5.20 clearly shows the presence of the same levels of the first run (see section 3.8) not present in literature, but with better resolution.

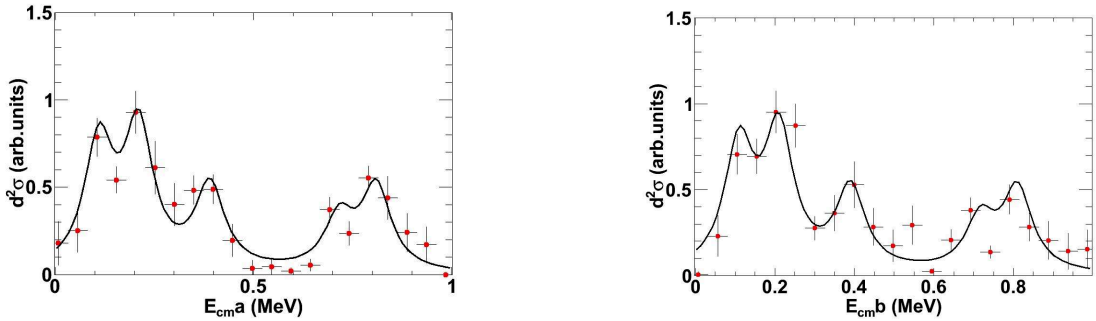

FIGURE 5.19: QF cross section reaction in arbitrary units for the two coincidences. The black circles are the experimental data.

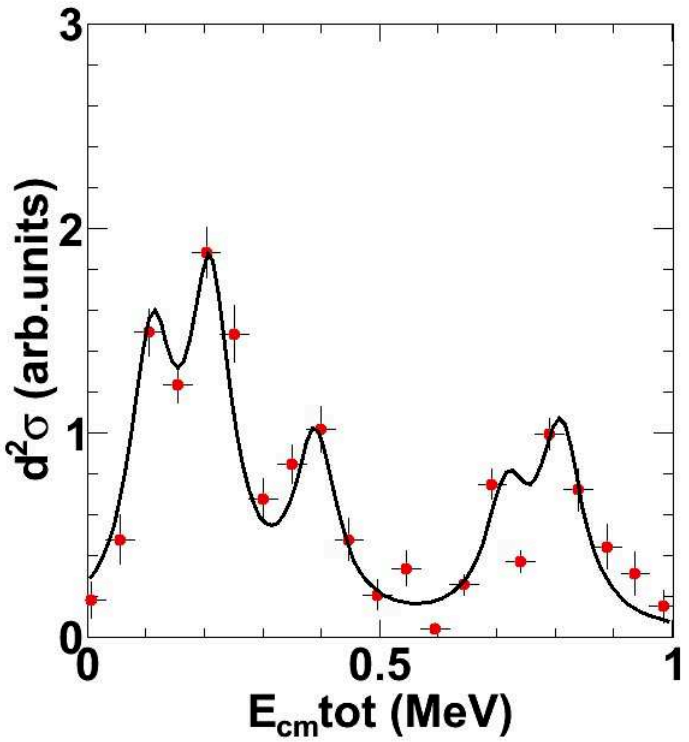

FIGURE 5.20: QF cross section of the ^{19}F(p, α_0)^{16}O reaction in arbitrary units. The black circles are the experimental data. The middle line represents the best fit to the data.

The two body cross section obtained is in arbitrary units; as said in section 3.5, absolute cross sections can be obtained only after normalization to the directly-measured excitation function.

5.5 Comparison with direct data

As said before, no absolute values of TH cross-section could be defined and normalization to direct data is necessary.

As a first step, a R-matrix fit of the direct astrophysical factor data available in the literature was performed (see section 2.64, [88]). In the calculation, has been used the non-resonant background from the NACRE compilation [15] and was chosen to normalize the THM data to the astrophysical factor of Lombardo et al. 2.10 assuming a $J^{\pi} = 0^{+}$ state in ^{20}Ne at an excitation energy of 13.642 MeV in contrast with [25] that attributed a spin-parity $J^{\pi} = 2^{+}$, as said in section 2.7.

In Fig.5.21, the direct astrophysical factor in is shown (symbols), together with the R-matrix fit.

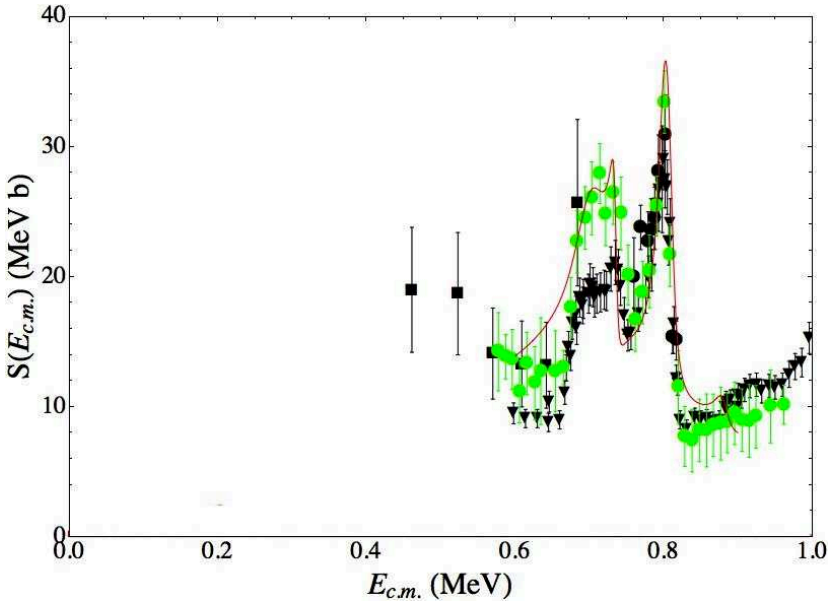

FIGURE 5.21: R-matrix fit of direct data (black squares from [22], black triangle from [25], black circles from [26] and green simbols from [16]).

Interference effects were fully taken into account, which justify the sharp drop of the astrophysical factor in the energy region below about 0.66 MeV and above about 0.82 MeV.

R-matrix fit is needed to extract the reduced γ-widths of the measured 13.529, 13.586, and 13.642 MeV states in ^{20}Ne, to be inserted into the modified R-matrix fitting. These are fitted values and were not fixed in the calculation. Energy and spin parity of these resonances were instead fixed to the values given in literature. The resulting p- and α-reduced widths (γ_p and γ_α) are given in Table 5.3.

$\mathbf{E}_{^{20}Ne}$ **(MeV)**	γ_p	γ_α	$\mathbf{J}^\pi$
13.529	0.085	0.078	2^+
13.586	0.015	0.041	2^+
13.642	0.019	0.047	0^+

TABLE 5.3: Resonance energies, spin parities, and α partial widths in R-matrix fit.

Therefore, the reduced widths of the lower energy resonances obtained with the modified R-matrix fit are normalized to the ones of the 13.529, 13.586, and 13.642 MeV ^{20}Ne states. The $\frac{d2\sigma}{dE_{c.m.}d\Omega n}$ best-fit cross section obtained is shown in figure 5.22.

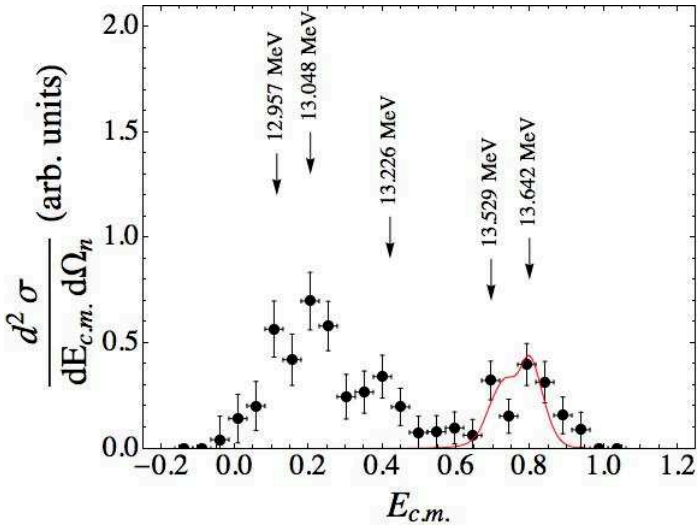

FIGURE 5.22: The cross section calculated in the modified R-matrix approach, normalized to the peak at 690-790 keV and convoluted with the experimental resolution. The red line represents the best fit to the data.

Values of γ_p and γ_{α_0} from the fitting below 600 keV were then used to evaluate the resonance contribution to the on-energy-shell ^{19}F(p, α_0)^{16}O astrophysical factor, according to standard R-matrix formulae, shown in Figure 5.23.

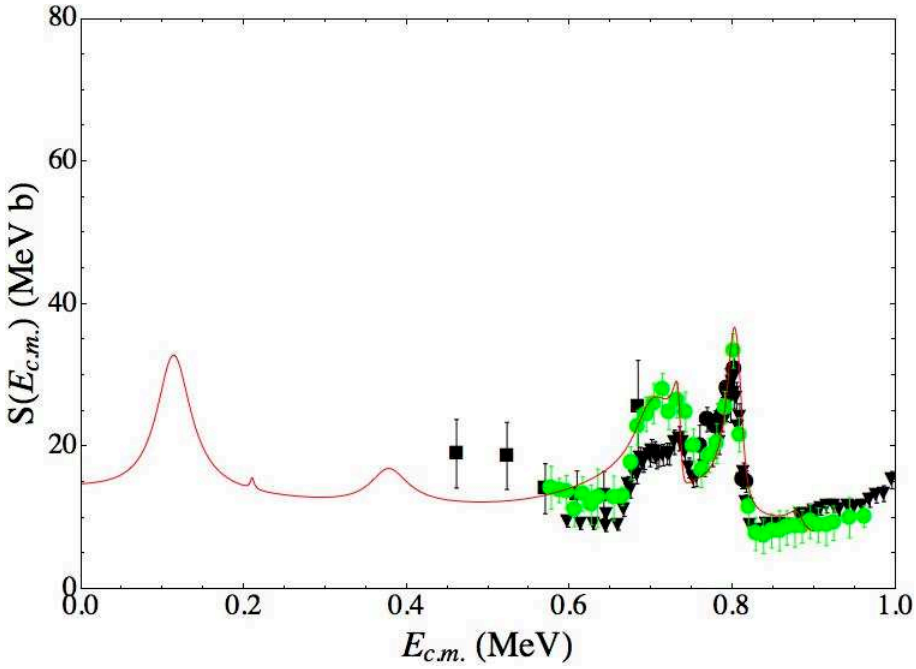

FIGURE 5.23: The red line show the combination of the S(E) factor from the fitting of Lombardo et al. data [16] (above 600 keV) and of the one calculated using standard R-matrix formulae, where the resonance parameters where taken from the generalized R-matrix fitting of THM data in fig. 5.22 (below 600 keV).

Since the TH cross section provided the resonance contribution only, the non-resonant part of the cross section was taken from Angulo et al. [15]. The SE-factor shows the presence of resonant structures not present in literature which is in disagreement with the NACRE S(E)-factor shows a non-resonant behavior from 0.6 MeV downward, but confirmed the TH data of the first run. Moreover, the main result of the present work is the estimate of the contribution of the 12.957 MeV ^{20}Ne level, single out from the other levels, as it is responsible of a resonance at 113 keV, well inside the energy range of astrophysical interest.

Chapter 6

Conclusion

In this thesis the Trojan Horse Method was used to extract the ^{19}F(p,α_0)^{16}O reaction cross section in the energy range of astrophysical interest ($E_{c.m.} \approx$ 0-1 MeV) in order to reduce the uncertainties in the nuclear reaction rates involved in the synthesis of F in the AGB stars and hence in the stellar model.
Indeed, fluorine abundance might represent a strong constraint of stellar internal structure, being very sensitive to the physical conditions and mixing phenomena taking place in their inner layers. When the abundances predicted by the current models are compared with the observed ones, an unacceptable discrepancy shows up even when model parameters are varied in a reasonable range. A possible justification could be given by a reassessment of the nuclear reaction rates involved in fluorine production and destruction.
In this contest, the ^{19}F(p,α)^{16}O channel represent the main fluorine depleting reaction in hydrogen rich environments, such as the outer layers of AGB stars, where fluorine can experience temperatures large enough to determine its destruction, owing to extra-mixing processes. The energy where this reaction takes place (the so called Gamow window) in a proton rich enviroment extend from 300 to 800 keV. However, direct measurements of the cross section stop at about 500 keV, while this reaction rate is still unknown at low energies; the astrophysical factor was extrapolated to low energies assuming a a non resonant trend. Thus only model calculations of the reaction rate are actually available in the temperature region most relevant for ^{19}F nucleosynthesis in AGB stars. Infact this measurement have to be performed inside the Energy windows relevant for astrophysics (that as said before extend from 0.8 down to 0.3 MeV). Anyway these energies are much lower

than the coulomb barrier of the ^{19}F+p channel that is about 2.5 MeV. This makes the cross section measurement of the nuclear processes under investigation very difficult, thus extrapolation is required to estimate the relevant low-energy cross section. For this reason a new experimental study through the THM is important because the method is particulary suited for the study of low-energy resonances.

In this work the THM was thus used to access this energy region, by extracting the quasi-free contribution to the ^{2}H(^{19}F, $\alpha_0{}^{16}$O)n reaction. The experiment was performed in Legnaro at the Laboratori Nazionali di Legnaro where the Tandem accelerator provided a 55 MeV ^{19}F beam impinged onto CD_2 target. In this case the reaction occurring through deuterium break-up, where the proton is the participant and neutron is the spectator of the two-body reaction.
The experimental setup consisted of a telescope devoted to oxygen detection, made up of an ionization chamber and a silicon position sensitive detector on one side with respect to the beam direction and one additional silicon PSD on the opposite side of the beam axis optimized for coincident detection of the alfa particles.
After detector calibration, the first step of the data analysis is the three-body reaction channel selection with the separation of the oxygen locus in the dE-E two-dimensional plot by means of a graphical cut.
Following the selection of the ^{16}O-α-n exit channel, the following step in data analysis is to establish whether in the selected experimental kinematic regions the contribution of the QF process to the overall ^{16}O-α coincidence yield is evident and well separated from others.
The presence of the QF-mechanism was checked by reconstruction of the experimental momentum distribution and the behavior of the coincidence yield with the neutron momentum values: only if these two experimental evidences confirm the role of the undetected neutron as spectator of the virtual two-body reaction, it is possible to select the QF-contribution to the three-body reaction. The performed study makes us confident that the QF mechanism gives the main contribution to the ^{19}F+d reaction at an energy of 55 MeV in the experimental kinematical regions in the -40$<$ p_s $<$ 20 MeV/c neutron momentum range. Moreover, it proves that the QF mechanism can be selected without significant contribution from contaminant SD processes and the analysis in PWIA is sufficient to describe the process.

The TH measurement of the α_0 channel reveal the presence of resonant structures not observed before;

- a resonance at about Ecm ∼113 keV, due to the population of the 12.957 MeV excited level of ^{20}Ne ($J^{\pi}=2^{+}$)
- a resonance at about Ecm ∼ 200 keV, due to the population of the 13.048 MeV excited level of ^{20}Ne ($J^{\pi}=4^{+}$).
- a group of resonance, the dominant is the one at about Ecm ∼ 380 keV, due to the population of the 13.226 MeV excited level of ^{20}Ne ($J^{\pi}=3^{-}$).
- three resonance at about Ecm ∼ 696, 739 and 798 keV, due to the population of the 13.529, 13.586 and 13.642 MeV excited level of ^{20}Ne ($J^{\pi}=2^{+}$, 2^{+} and 0^{+} respectively). These resonances have already been measured and are therefore used for the normalization.

In particular the resonance at lower energies is very important because lies in the Gamow peak region with important consequences on the fluorine destruction.
The experimental THM data are in contradiction with the NACRE extrapolation that support a non resonant trend of the low-energy S(E) factor. Indeed the data show the existence of three resonance in the energy regions below Ecm ≈ 450 keV which cause an increase of the reaction rate at astrophysical temperatures and can help to solve the discrepancies observed in fluorine abundance.

Bibliography

[1] C.E. Rolfs and W.S. Rodney. *Cauldrons in the Cosmos*. 1988.

[2] F. LeBlanc. *An Introduction to Stellar Astrophysics*. 2010. URL http://adsabs.harvard.edu/abs/2010isa..book.....L.

[3] A. I. Karakas. Nucleosynthesis of Low and Intermediate-mass Stars. In A. Goswami and B. E. Reddy, editors, *Principles and Perspectives in Cosmochemistry*, page 107, 2010. URL http://adsabs.harvard.edu/abs/2010ppc..conf..107K.

[4] J. C. Lattanzio. Evolution and Mixing in Low and Intermediate Mass Stars. In M. Busso, C. M. Raiteri, and R. Gallino, editors, *Nuclei in the Cosmos III*, volume 327 of *American Institute of Physics Conference Series*, page 353, 1995. URL http://adsabs.harvard.edu/abs/1995AIPC..327..353L.

[5] J. C. Lattanzio and A. I. Boothroyd. Nucleosynthesis of elements in low to intermediate mass stars through the AGB phase. In E. K. Zinner and T. J. Bernatowicz, editors, *American Institute of Physics Conference Series*, volume 402 of *American Institute of Physics Conference Series*, pages 85–114, March 1997. URL http://adsabs.harvard.edu/abs/1997AIPC..402...85L.

[6] O. Straniero, A. Chieffi, M. Limongi, M. Busso, R. Gallino, and C. Arlandini. Evolution and Nucleosynthesis in Low-Mass Asymptotic Giant Branch Stars. I. Formation of Population I Carbon Stars. *Astrophysical Journal*, 478: 332–339, March 1997. URL http://adsabs.harvard.edu/abs/1997ApJ...478..332S.

[7] C. A. Frost and J. C. Lattanzio. AGB Stars: What Should Be Done ? In *Liege International Astrophysical Colloquia*, volume 32 of *Liege International*

Astrophysical Colloquia, page 307, 1995. URL http://adsabs.harvard.edu/abs/1995LIACo..32..307F.

[8] A. Jorissen, V. V. Smith, and D. L. Lambert. Fluorine in red giant stars - Evidence for nucleosynthesis. *Astronomy and Astrophysics*, 261:164–187, 1992. URL http://adsabs.harvard.edu/abs/1992A%26A...261..164J.

[9] M. Lugaro, C. Ugalde, A. I. Karakas, J. Görres, M. Wiescher, J. C. Lattanzio, and R. C. Cannon. Reaction Rate Uncertainties and the Production of ^{19}F in Asymptotic Giant Branch Stars. *Astrophysical Journal Letters*, 615:934–946, November 2004. URL http://adsabs.harvard.edu/abs/2004ApJ...615..934L.

[10] K.M. Nollet, M. Busso, and G.J. Wasserburg. Cool bottom processes on the thermally-pulsing AGB and the isotopic composition of circumstellar dust grains. *Astrophysical Journal*, 582:1036–1058, November 2002. URL http://arXiv:astro-ph/0211271.

[11] S. Lucatello, T. Masseron, J. A. Johnson, M. Pignatari, and F. Herwig. Fluorine and Sodium in C-rich Low-metallicity Stars. *Astrophysical Journal*, 729:40, March 2011. URL http://adsabs.harvard.edu/abs/2011ApJ...729...40L.

[12] L. R. Nittler. Presolar stardust in meteorites: recent advances and scientific frontiers. *Earth and Planetary Science Letters*, 209:259–273, April 2003. URL http://adsabs.harvard.edu/abs/2003E%26PSL.209..259N.

[13] A. Jorissen and S. Goriely. The Nuclear Network Generator: A tool for nuclear astrophysics. *Nuclear Physics A*, 688:508–510, May 2001. URL http://adsabs.harvard.edu/abs/2001NuPhA.688..508J.

[14] K. Spyrou, C. Chronidou, S. Harissopulos, S. Kossionides, T. Paradellis, C. Rolfs, W. H. Schulte, and L. Borucki. Cross section and resonance strength measurements of ^{19}F(p, $\alpha\gamma$)^{16}O at E$_p$= 200 800 keV. *European Physical Journal A*, 7:79–85, January 2000. URL http://adsabs.harvard.edu/abs/2000EPJA....7...79S.

[15] C. Angulo, M. Arnould, M. Rayet, P. Descouvemont, D. Baye, C. Leclercq-Willain, A. Coc, S. Barhoumi, P. Aguer, C. Rolfs, R. Kunz, J. W. Hammer, A. Mayer, T. Paradellis, S. Kossionides, C. Chronidou, K. Spyrou, S. degl'Innocenti, G. Fiorentini, B. Ricci, S. Zavatarelli, C. Providencia, H. Wolters, J. Soares, C. Grama, J. Rahighi, A. Shotter, and M. Lamehi Rachti. A compilation of charged-particle induced thermonuclear reaction rates. *Nuclear Physics A*, 656:3–183, August 1999. URL http://adsabs.harvard.edu/abs/1999NuPhA.656....3A.

[16] I. Lombardo, D. Dell'Aquila, L. Campajola, E. Rosato, G. Spadaccini, and M. Vigilante. Analysis of the ^{19}F(p, α_0)^{16}O reaction at low energies and the spectroscopy of ^{20}Ne. *Journal of Physics G Nuclear Physics*, 40(12):125102, December 2013. URL http://adsabs.harvard.edu/abs/2013JPhG...40l5102L.

[17] M.L. Cognata, C. Spitaleri, A. Tumino, S. Typel, S. Cherubini, L. Lamia, A. Musumarra, R.G. Pizzone, A. Rinollo, C. Rolfs, S. Romano, D. Schurmann, and F. Strieder. Bare-nucleus astrophysical factor of the He3(d,p)He4 reaction via the "Trojan horse'" method. *Physical Review C*, 72(6):065802, December 2005.

[18] M. Lattuada, R.G. Pizzone, S. Typel, P. Figuera, D. Miljanic, A. Musumarra, M.G. Pellegriti, C. Rolfs, C. Spitaleri, and H.H. Wolter. The Bare Astrophysical S(E) Factor of the ^{7}Li(p, α)α Reaction. *Astrophysical Journal*, 562:1076–1080, December 2001. URL http://adsabs.harvard.edu/abs/2001ApJ...562.1076L.

[19] R. G. Pizzone, C. Spitaleri, M. Lattuada, A. Musumarra, M. G. Pellegriti, S. Romano, A. Tumino, S. Cherubini, P. Figuera, D. Miljanić, C. Rolfs, S. Typel, H. H. Wolter, V. Castellani, S. degl'Innocenti, and A. Imperio. Bare astrophysical S(E)-factor for the ^{6}Li(d, α)^{4}He and ^{7}Li(p, α)^{4}He reactions at astrophysical energies. *Nuclear Physics A*, 718:496–498, May 2003. URL http://adsabs.harvard.edu/abs/2003NuPhA.718..496P.

[20] E. Costanzo, M. Lattuada, S. Romano, D. Vinciguerra, and M. Zadro. A procedure for the analysis of the data of a three body nuclear reaction. *Nuclear Instruments and Methods in Physics Research A*, 295:373–376, November 1990. URL http://adsabs.harvard.edu/abs/1990NIMPA.295..373C.

[21] R. G. Pizzone, C. Spitaleri, A. M. Mukhamedzhanov, L. D. Blokhintsev, C. A. Bertulani, B. F. Irgaziev, M. L. Cognata, L. Lamia, and S. Romano. Effects of distortion of the intercluster motion in H2, He3, H3, Li6, and Be9 on Trojan horse applications. *Physical Review C*, 80(2), August 2009. URL http://adsabs.harvard.edu/abs/2009PhRvC..80b5807P.

[22] G. Breuer. Messung und analyse von winkelverteilung und wirkungsquerschnitt der reaktion f19(p,Îś0)o16 im energiebereich 0,4 bis 0,72 mev. *Zeitschrift fÃijr Physik*, 154(3):339–351, 1959. URL http://dx.doi.org/10.1007/BF01330257.

[23] D. Dieumegard, B. Maurel, and G. Amsel. Microanalysis of Flourine by nuclear reactions. I. ^{19}F(p, α $_0$) ^{16}O and^{19}F(p α γ) ^{16}O reactions. *Nuclear Instruments and Methods*, 168:93–103, January 1980. URL http://adsabs.harvard.edu/abs/1980NucIM.168...93D.

[24] F. Ajzenberg-Selove. Energy levels of light nuclei A = 18-20. *Nuclear Physics A*, 475:1–198, December 1987. URL http://adsabs.harvard.edu/abs/1987NuPhA.475....1A.

[25] A. Isoya. Analysis of the yield curves and the angular distributions of the reactions F ^{19} (p, α $_0$) O ^{16} and F ^{19} (p, α) O $^{16?}$. *Nuclear Physics*, 7:126–145, August 1958. URL http://adsabs.harvard.edu/abs/1958NucPh...7..126I.

[26] R. Caracciolo. The 13.645 MeV state in ^{20}Ne. *Lett. Nuovo Cimento*, 11, 1974. URL http://link.springer.com/article/10.1007%2FBF02752724.

[27] S.. Sengupta. *Worlds Beyond Our Own*. 2014.

[28] G. Baur, C. A. Bertulani, and H. Rebel. Coulomb dissociation as a source of information on radiative capture processes of astrophysical interest. *Nuclear Physics A*, 458:188–204, September 1986. URL http://adsabs.harvard.edu/abs/1986NuPhA.458..188B.

[29] A. M. Mukhamedzhanov and R. E. Tribble. Connection between asymptotic normalization coefficients, subthreshold bound states, and resonances. *Physical Review C*, 59:3418–3424, June 1999. URL http://adsabs.harvard.edu/abs/1999PhRvC..59.3418M.

[30] C. Spitaleri, M. Aliotta, S. Cherubini, M. Lattuada, D. Miljanić , S. Romano, N. Soic, M. Zadro, and R. A. Zappalà. Indirect ^{7}Li(p,α)^{4}He reaction at astrophysical energies. *Physical Review C*, 60(5):055802, November 1999. URL http://adsabs.harvard.edu/abs/1999PhRvC..60e5802S.

[31] E. M. Burbidge, G. R. Burbidge, W. A. Fowler, and F. Hoyle. Synthesis of the elements in stars. *Reviews of Modern Physics*, 29:547–650, 1957. URL http://adsabs.harvard.edu/abs/1957RvMP...29..547B.

[32] D. Clayton. *Handbook of Isotopes in the Cosmos*. September 2003. URL http://adsabs.harvard.edu/abs/2003hic..book.....C.

[33] H. Reeves. Galactic Cosmic Ray Origin of Li, Be and B in Stars. *Nature*, 226: 727–729, May 1970. URL http://adsabs.harvard.edu/abs/1970Natur.226..727R.

[34] A. G. W. Cameron. Nuclear Reactions in Stars and Nucleogenesis. *Pub. Astron. Soc. Pac.*, 69:201, 1957. URL http://adsabs.harvard.edu/abs/1957PASP...69..201C.

[35] I. Iben, Jr. and A. Renzini. Asymptotic giant branch evolution and beyond. *Annual Review of Astronomy and Astrophysics*, 21:271–342, 1983. URL http://adsabs.harvard.edu/abs/1983ARA%26A..21..271I.

[36] F. Herwig. Evolution of Asymptotic Giant Branch Stars. *Annual Review of Astronomy and Astrophysics*, 43:435–479, September 2005. URL http://adsabs.harvard.edu/abs/2005ARA%26A..43..435H.

[37] S. G. Ryan and A. J. Norton. *Stellar Evolution and Nucleosynthesis*. January 2010. URL http://adsabs.harvard.edu/abs/2010sen..book.....R.

[38] R. Kippenhahn and A. Weigert. *Stellar Structure and Evolution*. 1990. URL http://adsabs.harvard.edu/abs/1990sse..book.....K.

[39] C. Iliadis. *Nuclear Physics of Stars*. Wiley-VCH Verlag, 2007. URL http://adsabs.harvard.edu/abs/2007nps..book.....I.

[40] H. A. Bethe. Energy Production in Stars. *Physical Review*, 55:434–456, March 1939. URL http://adsabs.harvard.edu/abs/1939PhRv...55..434B.

[41] M. Lugaro. *Stardust from meteorites. An introduction to presolar grains*. September 2005. URL http://adsabs.harvard.edu/abs/2005sdfm.book.....L.

[42] A. McWilliam and M. Rauch. *Origin and Evolution of the Elements: Volume 4, Carnegie Observatories Astrophysics Series*. Carnegie Observatories astrophysics series. Cambridge University Press, 2004. URL http://books.google.it/books?id=MxrezhbXx-MC.

[43] M. Salaris and S. Cassisi. *Evolution of Stars and Stellar Populations*. 2006. URL http://adsabs.harvard.edu/abs/2006essp.book.....S.

[44] F. Hoyle. On Nuclear Reactions Occuring in Very Hot STARS.I. the Synthesis of Elements from Carbon to Nickel. *Astrophysical Journal Supplement*, 1: 121, September 1954. URL http://adsabs.harvard.edu/abs/1954ApJS...1..121H.

[45] O. Straniero, R. Gallino, and S. Cristallo. s process in low-mass asymptotic giant branch stars. *Nuclear Physics A*, 777:311–339, October 2006. URL http://adsabs.harvard.edu/abs/2006NuPhA.777..311S.

[46] I. Iben, Jr. Asymptotic Giant Branch Stars: Thermal Pulses, Carbon Production, and Dredge Up; Neutron Sources and S-Process Nucleosynthesis. In G. Michaud and A. V. Tutukov, editors, *Evolution of Stars: the Photospheric Abundance Connection*, volume 145 of *IAU Symposium*, page 257, 1991. URL http://adsabs.harvard.edu/abs/1991IAUS..145..257I.

[47] M. Pignatari. PhD thesis, University of Torino, 2006.

[48] R. J. De Boer. PhD thesis, University of Notre Dame, 2011.

[49] A. G. W. Cameron. Origin of Anomalous Abundances of the Elements in Giant Stars. *The Astrophysical Journal*, 121:144, January 1955. URL http://adsabs.harvard.edu/abs/1955ApJ...121..144C.

[50] A. G. W. Cameron. New Neutron Sources of Possible Astrophysical Importance. *Astronomical Journal*, 65:485, 1960. URL http://adsabs.harvard.edu/abs/1960AJ.....65Q.485C.

[51] D. D. Clayton, W. A. Fowler, T. E. Hull, and B. A. Zimmerman. Neutron capture chains in heavy element synthesis. *Annals of Physics*, 12: 331–408, March 1961. URL http://adsabs.harvard.edu/abs/1961AnPhy..12..331C.

[52] D. D. Clayton and M. E. Rassbach. Termination of the s-PROCESS. *The Astrophysical Journal*, 148:69, April 1967. URL http://adsabs.harvard.edu/abs/1967ApJ...148...69C.

[53] R. Gallino, C. Arlandini, M. Busso, M. Lugaro, C. Travaglio, O. Straniero, A. Chieffi, and M. Limongi. Evolution and Nucleosynthesis in Low-Mass Asymptotic Giant Branch Stars. II. Neutron Capture and the S-Process. *The Astrophysical Journal*, 497:388–403, April 1998. URL http://adsabs.harvard.edu/abs/1998ApJ...497..388G.

[54] M. Busso, R. Gallino, and G. J. Wasserburg. Nucleosynthesis in Asymptotic Giant Branch Stars: Relevance for Galactic Enrichment and Solar System Formation. *Annual Review of Astronomy and Astrophysics*, 37:239–309, 1999. URL http://adsabs.harvard.edu/abs/1999ARA%26A..37..239B.

[55] S. Cristallo. Evolution and nucleosynthesis in low-mass asymptotic giant branch stars. *Nuovo Cimento B Serie*, 122:697–706, June 2007. URL http://adsabs.harvard.edu/abs/2007NCimB.122..697C.

[56] F. Kappeler, C. Arlandini, M. Heil, R. Reifarth, F. Voss, and K. Wisshak. Neutron Capture at keV Energies - Probing the Stellar Interior. *Journal of Nuclear Science and Technology*, 39:518–523, August 2014. URL http://dx.doi.org/10.1080/00223131.2002.10875154.

[57] J. C. Lattanzio and M. A. Lugaro. What we do and do not know about the s-process in AGB stars. *Nuclear Physics A*, 758:477–484, July 2005. URL http://adsabs.harvard.edu/abs/2005NuPhA.758..477L.

[58] F. Herwig and T. Blocker. Overshoot in giant stars. In A. Noels, P. Magain, D. Caro, E. Jehin, G. Parmentier, and A. A. Thoul, editors, *Liege International Astrophysical Colloquia*, volume 35 of *Liege International Astrophysical Colloquia*, page 59, 2000. URL http://adsabs.harvard.edu/abs/2000LIACo..35...59H.

[59] S. Goriely, A. Jorissen, and M. Arnould. On the mechanisms of ^{19}F production. In W. Hillebrandt and E. Müller, editors, *Nuclear Astrophysics*, page 60, April 1989. URL http://adsabs.harvard.edu/abs/1989nuas.conf...60G.

[60] S. E. Woosley and W. C. Haxton. Supernova Neutrinos, Neutral Currents and the Origin of Fluorine. *Nature*, 334:45–47, 1988. URL http://adsabs.harvard.edu/abs/1988Natur.334...45W.

[61] G. Meynet and M. Arnould. Synthesis of ^{19}F in Wolf-Rayet stars. 355:176–180, 2000. URL http://adsabs.harvard.edu/abs/2000A%26A...355..176M.

[62] S. Uttenthaler, B. Aringer, T. Lebzelter, H. U. Käufl, R. Siebenmorgen, and A. Smette. The Fluorine Abundance in a Galactic Bulge AGB Star Measured from CRIRES Spectra. *Astrophysical Journal*, 682:509–514, July 2008. URL http://adsabs.harvard.edu/abs/2008ApJ...682..509U.

[63] E. Maiorca, H. Uitenbroek, S. Uttenthaler, S. Randich, M. Busso, and L. Magrini. A New Solar Fluorine Abundance and a Fluorine Determination in the Two Open Clusters M67 and NGC 6404. *Astrophysical Journal Letters*, 788:149, June 2014. URL http://adsabs.harvard.edu/abs/2014ApJ...788..149M.

[64] S. E. Woosley, D. H. Hartmann, R. D. Hoffman, and W. C. Haxton. The nu-process. *The Astrophysical Journal*, 356:272–301, June 1990. URL http://adsabs.harvard.edu/abs/1990ApJ...356..272W.

[65] A. Heger, E. Kolbe, W. C. Haxton, K. Langanke, G. Martínez-Pinedo, and S. E. Woosley. Neutrino nucleosynthesis. *Phys. Lett. B*, 606:258–264, 2005. URL http://adsabs.harvard.edu/abs/2005PhLB..606..258H.

[66] A. Palacios. ˆ26Al and ˆ19F nucleosynthesis in Wolf-Rayet and AGB stars. In T. Montmerle and C. Kahane, editors, *EAS Publications Series*, volume 19, pages 67–84, 2006. URL http://adsabs.harvard.edu/abs/2006EAS....19...67P.

[67] P. A. Crowther. Physical Properties of Wolf-Rayet Stars. *Review of Astronomy and Astrophysics*, 45:177–219, September 2007. URL http://adsabs.harvard.edu/abs/2007ARA%26A..45..177C.

[68] Y. Zhang and X.-W. Liu. Fluorine Abundances in Planetary Nebulae. *The Astrophysical Journal*, 631:L61–L64, September 2005. URL http://adsabs.harvard.edu/abs/2005ApJ...631L..61Z.

[69] M. Forestini, S. Goriely, A. Jorissen, and M. Arnould. Fluorine production in thermal pulses on the asymptotic giant branch. *Astronomy and Astrophysics*, 261:157–163, July 1992. URL http://adsabs.harvard.edu/abs/1992A%26A...261..157F.

[70] N. Mowlavi. On the third dredge-up phenomenon in asymptotic giant branch stars. *Astronomy and Astrophysics*, 344:617–631, April 1999. URL http://adsabs.harvard.edu/abs/1999A%26A...344..617M.

[71] C. Abia, A. Recio-Blanco, P. de Laverny, S. Cristallo, I. DomÃŋnguez, and O. Straniero. Fluorine in asymptotic giant branch carbon stars revisited. *The Astrophysical Journal*, 694(2), 2009. URL http://stacks.iop.org/0004-637X/694/i=2/a=971.

[72] S. Randich and L. Pasquini. *Chemical Abundances and Mixing in Stars in the Milky Way and its Satellites*. 2006. URL http://adsabs.harvard.edu/abs/2006cams.book.....R.

[73] C. Abia, K. Cunha, S. Cristallo, P. de Laverny, I. DomÃŋnguez, K. Eriksson, L. Gialanella, K. Hinkle, G. Imbriani, A. Recio-Blanco, V. V. Smith, O. Straniero, and R. Wahlin. Fluorine abundances in galactic asymptotic giant branch stars. *The Astrophysical Journal Letters*, 715(2), 2010. URL http://stacks.iop.org/2041-8205/715/i=2/a=L94.

[74] W. Aoki, S. Honda, T. C. Beers, M. Takada-Hidai, N. Iwamoto, N. Tominaga, H. Umeda, K. Nomoto, J. E. Norris, and S. G. Ryan. Spectroscopic Studies of Extremely Metal-poor Stars with the Subaru High-Dispersion Spectrograph. IV. The α-Element-Enhanced Metal-poor Star BS 16934-002. *Astrophysical Journal*, 660:747–761, May 2007. URL http://adsabs.harvard.edu/abs/2007ApJ...660..747A.

[75] M. Lugaro, S. E. de Mink, R. G. Izzard, S. W. Campbell, A. I. Karakas, S. Cristallo, O. R. Pols, J. C. Lattanzio, O. Straniero, R. Gallino, and T. C. Beers. Fluorine in carbon-enhanced metal-poor stars: a binary

scenario. *Astronomy and Astrophysics*, 484:L27–L30, June 2008. URL http://adsabs.harvard.edu/abs/2008A%26A...484L..27L.

[76] M. Griffiths. *Planetary Nebulae and How to Observe Them*. 2012. URL http://adsabs.harvard.edu/abs/2012pnho.book.....G.

[77] E. Zinner. Stellar Nucleosynthesis and the Isotopic Composition of Presolar Grains from Primitive Meteorites. *Annual Review of Earth and Planetary Sciences*, 26:147–188, 1998. URL http://adsabs.harvard.edu/abs/1998AREPS..26..147Z.

[78] T. Bernatowicz, G. Fraundorf, T. Ming, E. Anders, B. Wopenka, E. Zinner, and P. Fraundorf. Evidence for interstellar SiC in the Murray carbonaceous meteorite. *nature*, 330:728–730, December 1987. URL http://adsabs.harvard.edu/abs/1987Natur.330..728B.

[79] R. Gallino, M. Busso, and M. Lugaro. Neutron capture nucleosynthesis in AGB stars. In T. J. Bernatowicz and E. Zinner, editors, *American Institute of Physics Conference Series*, volume 402 of *American Institute of Physics Conference Series*, pages 115–153, March 1997. URL http://adsabs.harvard.edu/abs/1997AIPC..402..115G.

[80] E. K. Zinner. Presolar Grains. *Treatise on Geochemistry*, 1:17–39, December 2003. URL http://adsabs.harvard.edu/abs/2003TrGeo...1...17Z.

[81] B. Srinivasan and E. Anders. Noble gases in the Murchison meteorite - Possible relics of s-process nucleosynthesis. *Science*, 201:51–56, July 1978. URL http://adsabs.harvard.edu/abs/1978Sci...201...51S.

[82] E. Zinner, L. R. Nittler, R. Gallino, A. I. Karakas, M. Lugaro, O. Straniero, and J. C. Lattanzio. Silicon and Carbon Isotopic Ratios in AGB Stars: SiC Grain Data, Models, and the Galactic Evolution of the Si Isotopes. *Astrophysical Journal*, 650:350–373, October 2006. URL http://adsabs.harvard.edu/abs/2006ApJ...650..350Z.

[83] G. J. Wasserburg, A. I. Boothroyd, and I.-J. Sackmann. Deep Circulation in Red Giant Stars: A Solution to the Carbon and Oxygen Isotope Puzzles? *Astrophysical Journal Letters*, 447:L37, July 1995. URL http://adsabs.harvard.edu/abs/1995ApJ...447L..37W.

[84] D. D. Clayton. *Principles of stellar evolution and nucleosynthesis*. 1983. URL http://adsabs.harvard.edu/abs/1983psen.book.....C.

[85] G. Gamow. Zur Quantentheorie des Atomkernes. *Zeitschrift fur Physik*, 51: 204–212, March 1928. URL http://adsabs.harvard.edu/abs/1928ZPhy...51..204G.

[86] G. R. Satchler and N. Austern. Introduction to Nuclear Reactions. *Physics Today*, 34:81, 1981. URL http://adsabs.harvard.edu/abs/1981PhT....34e..81S.

[87] P. Descouvemont. Theoretical Models for Nuclear Astrophysics. In M. Terasawa, S. Kubano, T. Kishida, T. Kajino, T. Motobayashi, and K. Nomato, editors, *Origin of Matter and Evolution of Galaxies*, pages 241–253, December 2005. URL http://adsabs.harvard.edu/abs/2005omeg.conf..241D.

[88] A. M. Lane and R. G. Thomas. R-Matrix Theory of Nuclear Reactions. *Reviews of Modern Physics*, 30:257–353, April 1958. URL http://adsabs.harvard.edu/abs/1958RvMP...30..257L.

[89] K. Langanke, T. D. Shoppa, C. A. Barnes, and C. Rolfs. Energy loss, electron screening and the astrophysical ^{3}He(d, p)^{4}He cross section. *Physics Letters B*, 369:211–214, February 1996. URL http://adsabs.harvard.edu/abs/1996PhLB..369..211L.

[90] P. Cuzzocrea. Quartet states in ^{20}Ne. *Lett. Nuovo Cimento*, 28, 1980. URL http://link.springer.com/article/10.1007%2FBF02776224.

[91] C. A. Bertulani. The astrophysical reactions ^{12}C(α,γ)^{16}O and ^{7}Be(p,γ)^{8}B and Coulomb dissociation experiments. *Physical Review C*, 49:2688–2694, May 1994. URL http://adsabs.harvard.edu/abs/1994PhRvC..49.2688B.

[92] T. Motobayashi, N. Iwasa, Y. Ando, M. Kurokawa, H. Murakami, J. Ruan (Gen), S. Shimoura, S. Shirato, N. Inabe, M. Ishihara, T. Kubo, Y. Watanabe, M. Gai, R. H. France, K. I. Hahn, Z. Zhao, T. Nakamura, T. Teranishi, Y. Futami, K. Furutaka, and T. Delbar. Coulomb dissociation of ^{8}B and the ^{7}Be(p,γ)^{8}B reaction at low energies. *Physical Review Letters*, 73:2680–2683, November 1994. URL http://adsabs.harvard.edu/abs/1994PhRvL..73.2680M.

[93] A. M. Mukhamedzhanov and N. K. Timofeyuk. Astrophysical S-factor for the reaction ^{7}Be+p$\rightarrow^{8}$B+γ. *Soviet Journal of Experimental and Theoretical Physics Letters*, 51:282–284, March 1990. URL http://adsabs.harvard.edu/abs/1990JETPL..51..282M.

[94] L. Trache, A. Azhari, H. L. Clark, C. A. Gagliardi, Y.-W. Lui, A. M. Mukhamedzhanov, R. E. Tribble, and F. Carstoiu. Asymptotic normalization coefficients for ^{13}C+p$\rightarrow^{14}$N. *Physical Review C*, 58:2715–2719, November 1998. URL http://adsabs.harvard.edu/abs/1998PhRvC..58.2715T.

[95] A. Azhari, V. Burjan, F. Carstoiu, C. A. Gagliardi, V. Kroha, A. M. Mukhamedzhanov, F. M. Nunes, X. Tang, L. Trache, and R. E. Tribble. Asymptotic normalization coefficients and the ^{7}Be(p,γ)^{8}B astrophysical S factor. *Physical Review C*, 63(5):055803, May 2001. URL http://adsabs.harvard.edu/abs/2001PhRvC..63e5803A.

[96] A. M. Mukhamedzhanov, H. L. Clark, C. A. Gagliardi, Y.-W. Lui, L. Trache, R. E. Tribble, H. M. Xu, X. G. Zhou, V. Burjan, J. Cejpek, V. Kroha, and F. Carstoiu. Asymptotic normalization coefficients for ^{10}B$\rightarrow^{9}$Be+p. *Physical Review C*, 56:1302–1312, September 1997. URL http://adsabs.harvard.edu/abs/1997PhRvC..56.1302M.

[97] E. D. Johnson, G. V. Rogachev, A. M. Mukhamedzhanov, L. T. Baby, S. Brown, W. T. Cluff, A. M. Crisp, E. Diffenderfer, V. Z. Goldberg, B. W. Green, T. Hinners, C. R. Hoffman, K. W. Kemper, O. Momotyuk, P. Peplowski, A. Pipidis, R. Reynolds, and B. T. Roeder. Astrophysical Reaction Rate for the Neutron-Generator Reaction C13(α,n)O16 in Asymptotic Giant Branch Stars. *Physical Review Letters*, 97(19):192701, November 2006. URL http://adsabs.harvard.edu/abs/2006PhRvL..97s2701J.

[98] E. G. Adelberger, S. M. Austin, J. N. Bahcall, A. B. Balantekin, G. Bogaert, L. S. Brown, L. Buchmann, F. E. Cecil, A. E. Champagne, L. de Braeckeleer, C. A. Duba, S. R. Elliott, S. J. Freedman, M. Gai, G. Goldring, C. R. Gould, A. Gruzinov, W. C. Haxton, K. M. Heeger, E. Henley, C. W. Johnson, M. Kamionkowski, R. W. Kavanagh, S. E. Koonin, K. Kubodera, K. Langanke, T. Motobayashi, V. Pandharipande, P. Parker, R. G. Robertson, C. Rolfs, R. F. Sawyer, N. Shaviv, T. D. Shoppa, K. A. Snover, E. Swanson, R. E. Tribble, S. Turck-Chièze, and J. F. Wilkerson. Solar fusion cross

sections. *Reviews of Modern Physics*, 70:1265–1291, October 1998. URL http://adsabs.harvard.edu/abs/1998RvMP...70.1265A.

[99] N. Iwasa, F. Boué, G. Surówka, K. Sümmerer, T. Baumann, B. Blank, S. Czajkowski, A. Förster, M. Gai, H. Geissel, E. Grosse, M. Hellström, P. Koczon, B. Kohlmeyer, R. Kulessa, F. Laue, C. Marchand, T. Motobayashi, H. Oeschler, A. Ozawa, M. S. Pravikoff, E. Schwab, W. Schwab, P. Senger, J. Speer, C. Sturm, A. Surowiec, T. Teranishi, F. Uhlig, A. Wagner, W. Walus, and C. A. Bertulani. Measurement of the Coulomb Dissociation of ^{8}B at 254 MeV /nucleon and the ^{8}B Solar Neutrino Flux. *Physical Review Letters*, 83:2910–2913, October 1999. URL http://adsabs.harvard.edu/abs/1999PhRvL..83.2910I.

[100] M. Hass. A new measurement of the ˆ7Be(p, gamma)ˆ8B cross-secion with an implanted ˆ7Be target. *Physics Letters B*, 462:237–242, October 1999. URL http://adsabs.harvard.edu/abs/1999PhLB..462..237H.

[101] G. Baur. Breakup reactions as an indirect method to investigate low-energy charged-particle reactions relevant for nuclear astrophysics. *Physics Letters B*, 178:135–138, October 1986. URL http://adsabs.harvard.edu/abs/1986PhLB..178..135B.

[102] C. Spitaleri, L. Lamia, A. Tumino, R. G. Pizzone, S. Cherubini, A. del Zoppo, P. Figuera, M. La Cognata, A. Musumarra, M. G. Pellegriti, A. Rinollo, C. Rolfs, S. Romano, and S. Tudisco. The ^{11}B (p, α_0) ^{8}Be reaction at sub-Coulomb energies via the Trojan-horse method. *Physical Review C*, 69(5):055806, May 2004. URL http://adsabs.harvard.edu/abs/2004PhRvC..69e5806S.

[103] S. Cherubini, V. N. Kondratyev, M. Lattuada, C. Spitaleri, D. Miljanic, M. Zadro, and G. Baur. Indirect Investigation of the d + ^{6}Li Reaction at Low Energies Relevant for Nuclear Astrophysics. *Astrophysical Journal Letters*, 457:855, February 1996. URL http://adsabs.harvard.edu/abs/1996ApJ...457..855C.

[104] A. Tumino, C. Spitaleri, A. di Pietro, P. Figuera, M. Lattuada, A. Musumarra, M. G. Pellegriti, R. G. Pizzone, S. Romano, C. Rolfs, S. Tudisco, and S. Typel. Validity test of the "Trojan horse" method applied to

the ^{6}Li(p,α)^{3}He reaction. *Physical Review C*, 67(6):065803, June 2003. URL http://adsabs.harvard.edu/abs/2003PhRvC..67f5803T.

[105] N. S. Chant and P. G. Roos. Distorted-wave impulse-approximation calculations for quasifree cluster knockout reactions. *Physical Review C*, 15:57–68, January 1977. URL http://adsabs.harvard.edu/abs/1977PhRvC..15...57C.

[106] P. G. Roos, N. S. Chant, A. A. Cowley, D. A. Goldberg, H. D. Holmgren, and R. Woody, III. Absolute spectroscopic factors from the (p, pα) reaction at 100 MeV on 1p-shell nuclei. *Physical Review C*, 15:69–83, January 1977. URL http://adsabs.harvard.edu/abs/1977PhRvC..15...69R.

[107] S. Typel and H. H. Wolter. Extraction of Astrophysical Cross Sectionsin the Trojan-Horse Method. *Few-Body Systems*, 29:75–93, 2000. URL http://adsabs.harvard.edu/abs/2000FBS....29...75T.

[108] M. Jain, P. G. Roos, H. G. Pugh, and H. D. Holmgren. The (p, pα) and (α, 2α) reactions on ^{6}Li and ^{7}Li at 60 MeV. *Nuclear Physics A*, 153:49–81, September 1970. URL http://adsabs.harvard.edu/abs/1970NuPhA.153...49J.

[109] I. Šlaus, R. G. Allas, L. A. Beach, R. O. Bondelid, E. L. Petersen, J. M. Lambert, P. A. Treado, and R. A. Moyle. Quasifree processes in the ^{2}H + ^{3}He interaction. *Nuclear Physics A*, 286:67–88, August 1977. URL http://adsabs.harvard.edu/abs/1977NuPhA.286...67S.

[110] P.G. Roos, D.A. Goldberg, N.S. Chant, R. Woody, and W. Reichart. The α-d and τ-t cluster structure of ^{6}Li. *Nuclear Physics A*, 257:317–332, February 1976. URL http://adsabs.harvard.edu/abs/1976NuPhA.257..317R.

[111] S. Typel and G. Baur. Theory of the Trojan-Horse method. *Annals of Physics*, 305:228–265, June 2003. URL http://adsabs.harvard.edu/abs/2003AnPhy.305..228T.

[112] C. Spitaleri, S. Typel, R. G. Pizzone, M. Aliotta, S. Blagus, M. Bogovac, S. Cherubini, P. Figuera, M. Lattuada, M. Milin, D. Miljanić, A. Musumarra, M. G. Pellegriti, D. Rendić, C. Rolfs, S. Romano, N. Soić, A. Tumino, H. H. Wolter, and M. Zadro. "Trojan horse" method applied to ^{2}H(^{6}Li,α)^{4}He at

astrophysical energies. *Physical Review C*, 63(5):055801, May 2001. URL http://adsabs.harvard.edu/abs/2001PhRvC..63e5801S.

[113] S. Engstler, G. Raimann, C. Angulo, U. Greife, C. Rolfs, U. Schröder, E. Somorjai, B. Kirch, and K. Langanke. Isotopic dependence of electron screening in fusion reactions. *Zeitschrift fur Physik A Hadrons and Nuclei*, 342:471–482, December 1992. URL http://adsabs.harvard.edu/abs/1992ZPhyA.342..471E.

[114] R.G. Pizzone, C. Spitaleri, L. Lamia, C. Bertulani, A. Mukhamedzhanov, L. Blokhintsev, V. Burjan, S. Cherubini, Z. Hons, G.G. Kiss, V. Kroha, M. La Cognata, C. Li, J. Mrazek, Š. Piskoř, S.M.R. Puglia, G.G. Rapisarda, S. Romano, M.L. Sergi, and A. Tumino. Trojan horse particle invariance studied with the Li6(d,α)He4 and Li7(p,α)He4 reactions. *Physical Review C*, 83(4):045801, April 2011. URL http://adsabs.harvard.edu/abs/2011PhRvC..83d5801P.

[115] A. Tumino, C. Spitaleri, A. Mukhamedzhanov, G.G. Rapisarda, S. Cherubini, V. Crucillá, Z. Elekes, Z. Fülöp, M. Gulino, G. Gyürky, G. Kiss, M. La Cognata, L. Lamia, F. Mudó, R.G. Pizzone, S. Romano, M.L. Sergi, and E. Somorjai. Suppression of the Coulomb Interaction in the Off-Energy-Shell p-p Scattering from the p+d→p+p+n Reaction. *Physical Review Letters*, 98(25):252502, June 2007. URL http://adsabs.harvard.edu/abs/2007PhRvL..98y2502T.

[116] A. Rinollo, S. Romano, C. Spitaleri, C. Bonomo, S. Cherubini, A. Del Zoppo, P. Figuera, M. La Cognata, L. Lamia, A. Musumarra, and et al. Measurement of cross section and astrophysical factor of the d(d,p)t reaction using the Trojan Horse Method. *Nuclear Physics A*, 758:146–149, July 2005. URL http://adsabs.harvard.edu/abs/2005NuPhA.758..146R.

[117] A. Tumino, C. Spitaleri, A. M. Mukhamedzhanov, S. Typel, M. Aliotta, V. Burjan, M. Gimenez del Santo, G. G. Kiss, V. Kroha, Z. Hons, M. La Cognata, L. Lamia, J. Mrazek, R. G. Pizzone, S. Piskor, G. G. Rapisarda, S. Romano, M. L. Sergi, and R. Spartà. Low-energy d+d fusion via the Trojan Horse Method. *Journal of Physics Conference Series*, 436(1):012073, April 2013. URL http://adsabs.harvard.edu/abs/2013JPhCS.436a2073T.

[118] R. G. Pizzone, A. Tumino, S. degl'Innocenti, C. Spitaleri, S. Cherubini, A. Musumarra, and S. Romano. Trojan Horse estimate of bare nucleus astrophysical S(E)-factor for the ^{6}Li(p,α)^{3}He reaction and its astrophysical implications. *Astronomy and Astrophysics*, 438:779–784, August 2005. URL http://adsabs.harvard.edu/abs/2005A%26A...438..779P.

[119] A. Tumino, C. Spitaleri, M. L. Sergi, V. Kroha, V. Burjan, S. Cherubini, Z. Fülöp, M. La Cognata, L. Lamia, J. Novác, R. G. Pizzone, S. Romano, E. Somorjai, S. Tudisco, and J. Vincour. Validity test of the Trojan Horse Method applied to the ^{7}Li + p $\rightarrow$ α + α reaction via the ^{3}He break-up. *European Physical Journal A*, 27:243–248, March 2006. URL http://adsabs.harvard.edu/abs/2006EPJA...27S.243T.

[120] S. Romano, L. Lamia, C. Spitaleri, C. Li, S. Cherubini, M. Gulino, M. La Cognata, R. G. Pizzone, and A. Tumino. Study of the ^{9}Be(p,α)^{6}Li reaction via the Trojan Horse Method. *European Physical Journal A*, 27: 221–225, March 2006. URL http://adsabs.harvard.edu/abs/2006EPJA...27S.221R.

[121] L. Lamia, S. Romano, N. Carlin, S. Cherubini, V. Crucillà, M. M. de Moura, M. G. Del Santo, M. G. Munhoz, M. Gulino, R. Liguori Neto, M. La Cognata, F. Mudò, R. G. Pizzone, S. M. R. Puglia, M. L. Sergi, F. A. Souza, C. Spitaleri, A. A. P. Suaide, E. Szanto, A. Szanto de Toledo, S. Tudisco, and A. Tumino. Boron depletion: indirect measurement of the ^{10}B(p,α)^{7}Be S(E)-factor. *Nuclear Physics A*, 787:309–314, May 2007. URL http://adsabs.harvard.edu/abs/2007NuPhA.787..309L.

[122] S. Romano, C. Spitaleri, L. Lamia, A. Tumino, R. G. Pizzone, S. Cherubini, A. Del Zoppo, P. Figuera, M. Gulino, M. La Cognata, A. Musumarra, M. G. Pellegriti, A. Rinollo, and S. Tudisco. The astrophysical factor for the ^{11}B(p, α_0) ^{8}Be reaction extracted via the Trojan Horse method. *Nuclear Physics A*, 738:406–410, June 2004. URL http://adsabs.harvard.edu/abs/2004NuPhA.738..406R.

[123] M. La Cognata, S. Romano, C. Spitaleri, R. Tribble, L. Trache, S. Cherubini, C. Fu, L. Lamia, A. Mukhamedzhanov, R. G. Pizzone, C. Rolfs, G. Tabacaru, and A. Tumino. Indirect measurement of the ^{15}N(p,α)^{12}C reaction cross section through the Trojan-Horse Method. *European Physical Journal A*, 27:

249–254, March 2006. URL http://adsabs.harvard.edu/abs/2006EPJA...27S.249L.

[124] M. La Cognata, C. Spitaleri, A. M. Mukhamedzhanov, B. Irgaziev, R. E. Tribble, A. Banu, S. Cherubini, A. Coc, V. Crucillà, V. Z. Goldberg, M. Gulino, G. G. Kiss, L. Lamia, J. Mrazek, R. G. Pizzone, S. M. R. Puglia, G. G. Rapisarda, S. Romano, M. L. Sergi, G. Tabacaru, L. Trache, W. Trzaska, and A. Tumino. Measurement of the 20 and 90keV Resonances in the O18(p,α)N15 Reaction via the Trojan Horse Method. *Physical Review Letters*, 101(15):152501, October 2008. URL http://adsabs.harvard.edu/abs/2008PhRvL.101o2501L.

[125] M. L. Sergi, C. Spitaleri, A. Coc, A. Mukhamedzhanov, S. V. Burjan, M. Gulino, F. Hammache, Z. Hons, B. Irgaziev, G. G. Kiss, V. Kroha, M. La Cognata, L. Lamia, R. G. Pizzone, N. de Séréville, and E. Somorjai. The 65 keV resonance in the ^{17}O(p,α)^{14}N thermonuclear reaction. *Nuclear Physics A*, 834:676–678, March 2010. URL http://adsabs.harvard.edu/abs/2010NuPhA.834..676S.

[126] M. La Cognata, C. Spitaleri, O. Trippella, G. G. Kiss, G. V. Rogachev, A. M. Mukhamedzhanov, M. Avila, G. L. Guardo, E. Koshchiy, A. Kuchera, L. Lamia, S. M. R. Puglia, S. Romano, D. Santiago, and R. Spartà. Measurement of the -3keV Resonance in the Reaction C13(α,n)O16 of Importance in the s-Process. *Physical Review Letters*, 109(23):232701, December 2012. URL http://adsabs.harvard.edu/abs/2012PhRvL.109w2701L.

[127] M. La Cognata, A. M. Mukhamedzhanov, C. Spitaleri, I. Indelicato, M. Aliotta, V. Burjan, S. Cherubini, A. Coc, M. Gulino, Z. Hons, G. G. Kiss, V. Kroha, L. Lamia, J. Mrázek, S. Palmerini, Š. Piskoř, R. G. Pizzone, S. M. R. Puglia, G. G. Rapisarda, S. Romano, M. L. Sergi, and A. Tumino. The Fluorine Destruction in Stars: First Experimental Study of the ^{19}F(p, α_0)^{16}O Reaction at Astrophysical Energies. *Astrophysical Journal Letters*, 739:L54, October 2011. URL http://adsabs.harvard.edu/abs/2011ApJ...739L..54L.

[128] A. Tumino, C. Spitaleri, C. Bonomo, S. Cherubini, P. Figuera, M. Gulino, M. La Cognata, L. Lamia, A. Musumarra, M. G. Pellegriti, R. G. Pizzone, A. Rinollo, and S. Romano. Quasi-free ^{6}Li(n,α)^{3}H reaction at low energy

from ^{2}H break-up. *European Physical Journal A Supplement*, 25:649–650, September 2005. URL http://adsabs.harvard.edu/abs/2005EPJAS..25..649T.

[129] C. Spitaleri, A. M. Mukhamedzhanov, L. D. Blokhintsev, M. L. Cognata, R. G. Pizzone, and A. Tumino. The Trojan Horse Method in nuclear astrophysics. *Physics of Atomic Nuclei*, 74:1725–1739, December 2011. URL http://adsabs.harvard.edu/abs/2011PAN....74.1725S.

[130] M. Zadro, D. Miljanić, C. Spitaleri, G. Calvi, M. Lattuada, and F. Riggi. Excitation function of the quasifree contribution in the ^{2}H(^{7}Li,$\alpha\alpha$)n reaction at E_0=28-48 MeV. *Physical Review C*, 40:181–185, July 1989. URL http://adsabs.harvard.edu/abs/1989PhRvC..40..181Z.

[131] M. Gulino, C. Spitaleri, X. D. Tang, G. L. Guardo, L. Lamia, S. Cherubini, B. Bucher, V. Burjan, M. Couder, P. Davies, R. deBoer, X. Fang, V. Z. Goldberg, Z. Hons, V. Kroha, L. Lamm, M. La Cognata, C. Li, C. Ma, J. Mrazek, A. M. Mukhamedzhanov, M. Notani, S. O'Brien, R. G. Pizzone, G. G. Rapisarda, D. Roberson, M. L. Sergi, W. Tan, I. J. Thompson, and M. Wiescher. Suppression of the centrifugal barrier effects in the off-energy-shell neutron $+^{17}$O interaction. *Physical Review C*, 87(1):012801, January 2013. URL http://adsabs.harvard.edu/abs/2013PhRvC..87a2801G.

[132] O. B. Tarasov and D. Bazin. LISE++: Radioactive beam production with in-flight separators. *Nuclear Instruments and Methods in Physics Research B*, 266:4657–4664, October 2008. URL http://adsabs.harvard.edu/abs/2008NIMPB.266.4657T.

[133] G. F. Knoll. *Radiation detection and measurement*. 2000. URL http://adsabs.harvard.edu/abs/2000rdm..book.....K.

[134] F. Ajzenberg-Selove. Energy levels of light nuclei A = 16-17. *Nuclear Physics A*, 460:1–110, November 1986. URL http://adsabs.harvard.edu/abs/1986NuPhA.460....1A.

[135] J. M. Blatt and L. C. Biedenharn. The Angular Distribution of Scattering and Reaction Cross Sections. *Reviews of Modern Physics*, 24:258–272, October 1952. URL http://adsabs.harvard.edu/abs/1952RvMP...24..258B.

[136] M. La Cognata, C. Spitaleri, and A. M. Mukhamedzhanov. Effect of high-energy resonances on the 18o(p, Îś)15n reaction rate at agb and post-agb relevant temperatures. *The Astrophysical Journal*, 723(2):1512, 2010. URL http://stacks.iop.org/0004-637X/723/i=2/a=1512.